

Meniscus dynamics and

evaporation in inkjet printing



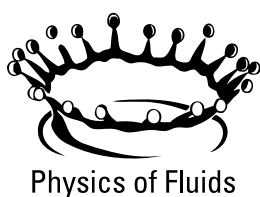
Maaïke Rump

# Meniscus dynamics and selective evaporation in inkjet printing

Maaïke Rump

**Graduation committee:**

Prof. dr. J.L. Herek (chair)	University of Twente
Prof. dr. rer. nat. D. Lohse (supervisor)	University of Twente
Prof. dr. M. Versluis (supervisor)	University of Twente
Dr. T.J. Segers (co-supervisor)	University of Twente
Dr. E.S. Kooij	University of Twente
Prof. dr. ir. L.I. Segerink	University of Twente
Prof. dr. H.M.A. Wijshoff	Eindhoven University of Technology
Prof. dr. N.F. Shahidzadeh	University of Amsterdam

**Canon****UNIVERSITY  
OF TWENTE.**

The work in this thesis was carried out at the Physics of Fluids group of the Faculty of Science and Technology of the University of Twente. This thesis was part of an Industrial Partnership Programme of the Netherlands Organisation for Scientific Research (NWO), cofinanced by Canon Production Printing Netherlands B.V., University of Twente, and Eindhoven University of Technology.

Dutch title:

*Oppervlaktedynamica en selectieve verdamping in inkjet printen*

Publisher:

Maaïke Rump, Physics of Fluids, University of Twente,  
P.O. Box 217, 7500 AE Enschede, The Netherlands

Copyright © 2022. All rights reserved.

No part of this work may be reproduced or transmitted for commercial purposes, in any form or by any means, electronic or mechanical, including photocopying and recording, or by any information storage or retrieval system, except as expressly permitted by the publisher.

ISBN: 978-90-365-5372-8

DOI: 10.3990/1.9789036553728

# MENISCUS DYNAMICS AND SELECTIVE EVAPORATION IN INKJET PRINTING

DISSERTATION

to obtain  
the degree of doctor at the University of Twente,  
on the authority of the rector magnificus,  
Prof. dr. ir. A. Veldkamp,  
on account of the decision of the Doctorate Board,  
to be publicly defended  
on Friday the 3rd of June 2022 at 12:45

by

Maaïke Rump  
Born on the 31st of July 1994  
in Utrecht, Netherlands



This dissertation has been approved by the supervisors:

Prof. dr. rer. nat. D. Lohse

Prof. dr. M. Versluis

and the co-supervisor:

Dr. T.J. Segers

# Contents

<b>Introduction</b>	<b>1</b>
<b>1 Meniscus oscillations driven by flow focusing lead to bubble pinch-off and entrainment in a piezoacoustic inkjet nozzle</b>	<b>9</b>
1.1 Introduction . . . . .	10
1.2 Experimental and numerical methods . . . . .	14
1.2.1 Printhead and ink . . . . .	14
1.2.2 Imaging setup . . . . .	15
1.2.3 Measurement procedure . . . . .	16
1.2.4 Image analysis . . . . .	16
1.2.5 Piezo eigenfrequency characterization through ring-down measurements . . . . .	18
1.2.6 Boundary integral simulations . . . . .	18
1.3 Results & discussion . . . . .	19
1.3.1 Meniscus and bubble dynamics . . . . .	19
1.3.2 Piezo actuator characterization . . . . .	21
1.3.3 Meniscus shape deformation process . . . . .	23
1.3.4 Jet formation mechanism . . . . .	24
1.3.5 The bubble pinch-off window . . . . .	27
1.4 Conclusions . . . . .	29
<b>2 Vorticity-induced flow-focusing leads to bubble entrainment in an inkjet printhead: synchrotron X-ray and volume-of-fluid visualizations</b>	<b>31</b>
2.1 Introduction . . . . .	32
2.2 Ultrafast X-ray phase contrast imaging . . . . .	34
2.2.1 Set-up and procedure . . . . .	34

2.2.2	Image processing	36
2.3	Numerical method	38
2.3.1	Governing equations	38
2.3.2	Numerical setup	39
2.4	Results & discussion	41
2.4.1	Phenomenology and numerical validation	41
2.4.2	Bubble pinch-off classes	42
2.4.3	Physical mechanism of pinch-off	44
2.5	Conclusion	48
<b>3</b>	<b>Predicting the meniscus shape modes of an inkjet nozzle in-</b>	
	<b>terface</b>	<b>49</b>
3.1	Introduction	50
3.2	Experimental and numerical methods	51
3.2.1	Capillary dispersion relation	51
3.2.2	Set-up	51
3.2.3	Procedure	52
3.2.4	Data analysis	53
3.2.5	Boundary Integral simulations	57
3.3	Results & discussion	58
3.4	Conclusion	64
3.5	Appendix	64
<b>4</b>	<b>Selective evaporation at the nozzle exit in piezoacoustic inkjet</b>	
	<b>printing</b>	<b>67</b>
4.1	Introduction	68
4.2	Printhead, model ink, and experimental procedure	70
4.3	Analytical model of the printhead acoustics	73
4.4	Numerical model	79
4.4.1	Evaporation phase	80
4.4.2	Probe pulse and jetting pulse	83
4.5	Results & discussion	85
4.5.1	Influence of drying on drop formation	85
4.5.2	Acoustically probing the drying phenomenon	86
4.5.3	Recovering the liquid composition	92
4.6	Conclusion & outlook	94

<b>5 Role of surfactants on droplet formation in DoD piezoacoustic</b>	
<b>inkjet printing</b>	<b>95</b>
5.1 Introduction . . . . .	96
5.2 Experimental methods . . . . .	99
5.2.1 Printhead and ink . . . . .	99
5.2.2 Imaging setups . . . . .	100
5.2.3 Image analysis . . . . .	101
5.2.4 Viscosity measurement . . . . .	104
5.3 Numerical model . . . . .	104
5.3.1 Evaporation phase . . . . .	105
5.3.2 Droplet formation . . . . .	105
5.4 Results & discussion . . . . .	106
5.4.1 Droplet velocity . . . . .	106
5.4.2 Droplet formation . . . . .	109
5.4.3 Evaporation . . . . .	110
5.5 Conclusion . . . . .	115
5.6 Appendix . . . . .	116
<b>Conclusions &amp; Outlook</b>	<b>121</b>
<b>References</b>	<b>127</b>
<b>Summary</b>	<b>145</b>
<b>Samenvatting</b>	<b>149</b>
<b>Scientific output</b>	<b>153</b>
<b>Acknowledgments</b>	<b>155</b>

# Introduction

If you want to get a digital image or document on paper, most of us will use the printer at home or the office. It is a comfortable method as the desired pattern is easily and quickly deposited on the paper. There is no need to own a stamp with the correct pattern, let alone to cover the stamp in ink, push it on the paper, and peel it off. Furthermore, a single printer can deposit a wide variety of designs onto paper. When ink droplets are the material that generates the pattern on the paper, the process is called inkjet printing. The ink droplets in inkjet printing are highly reproducible in size and speed, and can therefore be deposited with high accuracy [1-4].

An example of the accuracy and reproducibility of inkjet printing is demonstrated in Fig. 1 where it seems we are observing the formation of a single

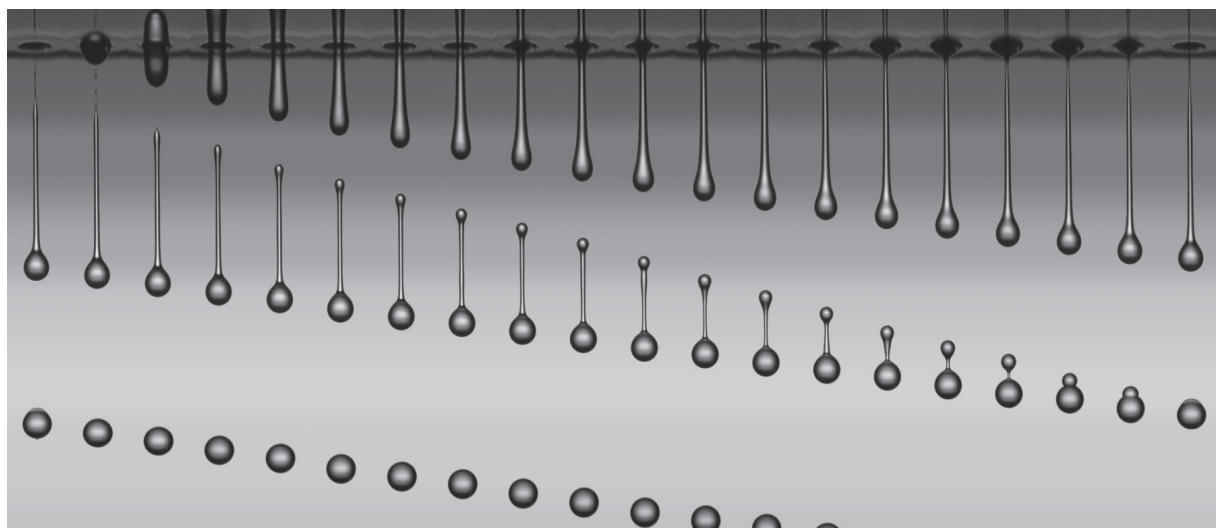


Figure 1: Time-sequence of the piezoacoustic drop-on-demand inkjet printing process, with picoliter droplets (diameter  $\approx 15\text{ }\mu\text{m}$ ). Image taken from [5].

droplet over time. Instead, between each snapshot in this time-sequence, a thousand droplets are produced.

The high control over the ink droplets has led to the use of inkjet printing in applications beyond the printing of graphics. Using light-emitting polymers, and their self-assembling properties during the drying process, the high control in depositing the droplets using inkjet printing has been used to develop organic electroluminescent displays [6,7]. The use of solutions containing conductive polymers as ink has also led to the printing of electronic circuits [8], which was developed further into using inks containing graphene [9,10]. Similarly, printing polymer solutions has been used to produce tissue-like materials [11] and artificial muscles [12]. Inkjet printing is also used for the production of pharmaceutical products, such as oral tablets, where the high accuracy of the droplet size is used to control the concentrations of different materials [13]. Another application where the accurate control over liquid quantity is desired is in the lubrication of moving parts that are subject to friction and wear, such as ball bearings, to optimize the lubrication layer thickness [14].

There are two main techniques to generate the droplets: continuous inkjet printing and - the focus of this thesis - drop-on-demand (DOD) inkjet printing, both illustrated in Fig. 2. In continuous inkjet printing, the droplets are created by ejecting a constant stream of liquid out of the printhead that

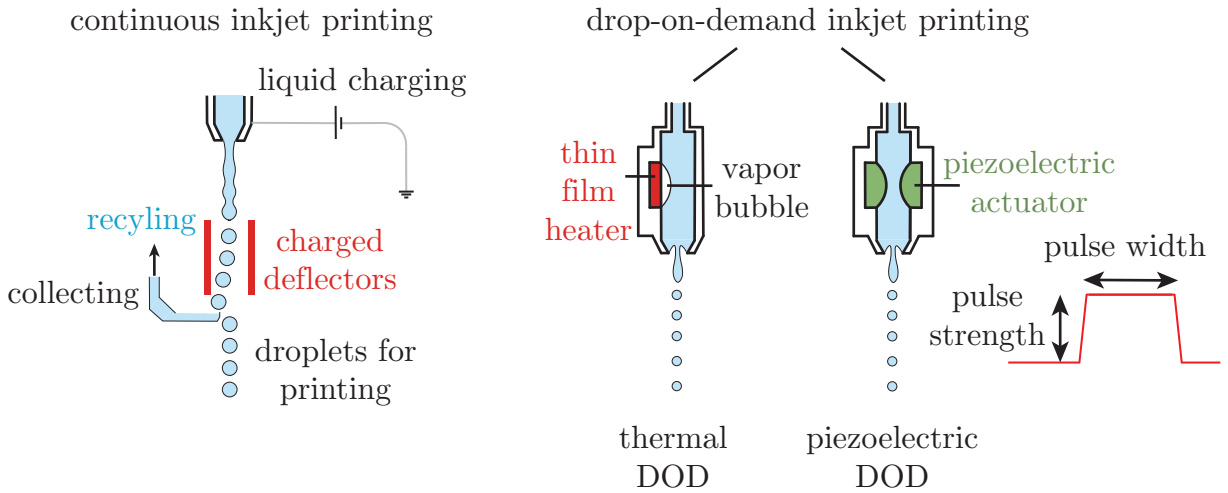


Figure 2: Schematic representation of a continuous inkjet printer (left) and a thermal and piezoelectric drop-on-demand (DOD) inkjet printer on the right. Included is a trapezoidal piezo driving pulse that is typically used in this thesis. Inspired by [15].

breaks up due to the Rayleigh-Plateau instability, similar to how droplets are formed from a dripping faucet. The droplets are either deposited on the substrate, or are deflected and recycled. The DOD technique produces a droplet on demand and jetted toward the substrate, as also illustrated in Fig. 1. The droplet formation is triggered by a pressure build-up in the ink channel, which can be achieved by thermal nucleation of a small vapor bubble with a thin film heater (thermal DOD), or by the motion of a piezoelectric actuator (piezoelectric DOD). While thermal DOD is mostly used in home and office printers, piezoelectric DOD is used in high-end and industrial printing technologies, because of the increased flexibility and control over the droplet volume and velocity. In Fig. 3 is an example of such an industrial printer from our collaborators at Canon Production Printing B.V. The origin of this flexibility lies in the easily adjusted actuation of the system, namely by changing the strength and width of the pulse to actuate the piezo, which also allows for droplet production with a wide variation in liquid properties.

Whether an ink will result in reliable and stable droplet formation, depends on the actuation of the piezo and on the liquid properties of the ink. The ideal conditions can be described as a function of the actuation of the system and the properties of the ink. Figure 4 presents these features. The Reynolds number,  $Re = UR\rho/\mu$ , is the ratio of inertial and viscous forces. In inkjet printing, this means the ratio between the force pushing the liquid out of the nozzle ( $U$  is the ink velocity,  $R$  is the droplet radius, and  $\rho$  is the ink density), which is related to the pressure build-up in the ink channel, and the ink viscosity  $\mu$ , which restricts the liquid from moving. The liquid properties are described by the Ohnesorge number,  $Oh = \mu/\sqrt{\rho\gamma R}$ , as the ratio between



Figure 3: A Canon printer from the varioPRINT iX-series, including the outline of a person to indicate the size of the printer.

the viscous and capillary timescales ( $\gamma$  is the surface tension of the ink). The  $Oh$  number in inkjet printing relates to the amount of droplets that is formed.

## Driving pulses leading to bubbles and smaller droplets

On the horizontal axis of Fig. 4 which represents the desired jetting regime, is the Reynolds number  $Re$ . At very low  $Re$ , e.g.  $Re \approx 1$ , the actuation does not result in a high enough ink speed to achieve pinching-off from the liquid inside the nozzle, and hence no droplet is produced. Increasing  $Re$  too much results in splashing of the droplet onto the substrate, which is undesirable as the splashed droplets reduce the quality of the print. However, the upper limit of  $Re$  is often desired in order to achieve higher printing speeds, which is achieved by printing more droplets in the same amount of time, for which the droplets have to travel faster. A higher droplet velocity requires a higher amplitude in piezo actuation to produce a high pressure in the ink channel. With this increase in pressure comes the increased probability of an undesired byproduct inside the printhead itself: a bubble. It has been shown that with increasing piezo amplitude there is an increased probability of bubble entrainment in the ink channel [17]. A bubble in the ink channel disturbs the acoustics [18–24],

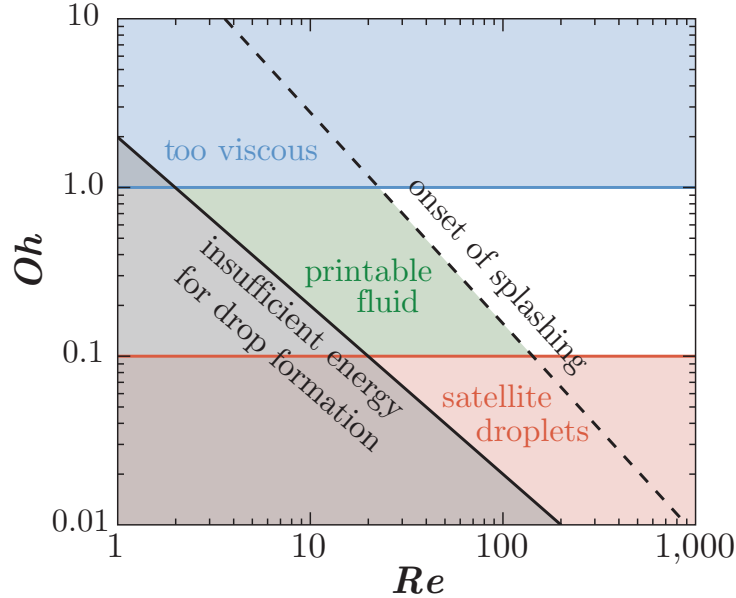


Figure 4: A schematic diagram showing the operating regime for stable operation of drop-on-demand inkjet printing as function of the Reynolds number  $Re$  and the Ohnesorge number  $Oh$ . Adapted from [3, 16].



resulting in a disruption in, and eventually stops, the droplet formation [17, 25, 26]. The disruption in the channel acoustics allows for detection of the bubble by measuring the channel acoustics using the deformable piezo element, and thus without requiring the imaging of the droplet formation [17, 19]. Once a bubble is entrained, it can be removed by flushing the channel with ink or through diffusive dissolution, i.e., by switching off the piezo actuation for a period of the order of seconds to minutes [23]. Neither of these solutions is desired as it interrupts the printing process. Therefore, the best method is to prevent the entrainment of these bubbles, which can be achieved by understanding the mechanisms of entrainment.

The shape of the piezo driving pulse also influences the size of the droplet that is produced [27]. One way to control the droplet size is to control the shape of the liquid-air interface, or meniscus. The shape of the oscillating meniscus is similar to a vibrating drum sheet, which can have different oscillation modes. Forcing the meniscus to oscillate at a higher mode will result in a smaller droplet [28]. Therefore, it allows for a change in droplet size without changing the geometry of the printhead, increasing the flexibility of the DOD inkjet printer even further.

## Liquid properties of a drying ink

On the vertical axis of the figure showing the stable jetting regime (Fig. 4), is the Ohnesorge number  $Oh$ . This ratio in inkjet printing describes primarily whether the viscosity dominates (high  $Oh$ ) or surface tension  $\gamma$  dominates (low  $Oh$ ). At high viscosity, the liquid resistance to movement is too high, and therefore, no droplet is produced. At high surface tension, which is the energy needed to create new surface area, the liquid jet that is produced breaks up into multiple droplets to reduce the surface area as quickly as possible. When the viscosity and surface tension are balanced, the jetted ink becomes a single droplet, which is desired for high control. In inkjet printing, the inks are multi-component, and commercial inks can contain around 25 different ingredients. These ingredients include water in water-based systems, co-solvents like glycerol to tune the viscosity, pigment particles to provide the color, and surfactants to stabilize the mixture and promote droplet spreading on the substrate, to name a few. As the different components have different properties, like how fast they evaporate (volatility) or adsorption onto the surface, the ink can change in  $Oh$  during the time in-between droplet formations. The change in  $Oh$  can be significant during longer times, like in between printing proce-

dures, as evaporation starts playing a role. The change in ink composition can be probed by measuring the droplet formation and running accurately corresponding numerical simulations [29,30]. However, the understanding of and the interaction between the different components is not advanced enough to be able to simulate many component combinations. Therefore, a further investigation into the drying phenomenon is highly desirable.

## A guide through the thesis

This thesis attempts to provide solutions to the challenges presented in the previous sections to improve the speed, accuracy and quality of piezoacoustic inkjet printing. Chapter [1] describes a mechanism of bubble entrainment in an inkjet nozzle that results from the large meniscus deformations at high driving voltages. We describe the experimental observations and provide a proof of concept for the proposed mechanism using (inviscid and irrotational) numerical simulations. In chapter [2] we aim to validate the proposed mechanism of chapter [1] by utilizing synchrotron experiments and combining these results with (viscous and rotational) numerical simulations. The investigation on meniscus deformations is continued in chapter [3] for lower driving voltages, where we investigate the different oscillating modes of the meniscus and attempt to predict the required driving frequency to trigger the different observed modes.

In the second part of the thesis, we focus on the multi-component properties of the ink inside the printhead. In chapter [4], we describe a method to measure changes in the concentration inside the nozzle during the evaporation of a mixture where one liquid has a higher evaporation rate than the other. We quantify the concentration changes by using the piezo element to measure the corresponding change of the acoustics inside the printhead. Using an in-house developed analytical model, which is further validated by numerical simulations, these measurements provide information on the liquid composition in the nozzle. Finally, in chapter [5] the liquid mixture is a water-surfactant solution, where we investigate how the presence of surfactant influences droplet formation and the resulting droplet velocity and volume during the different timescales involved in inkjet printing.

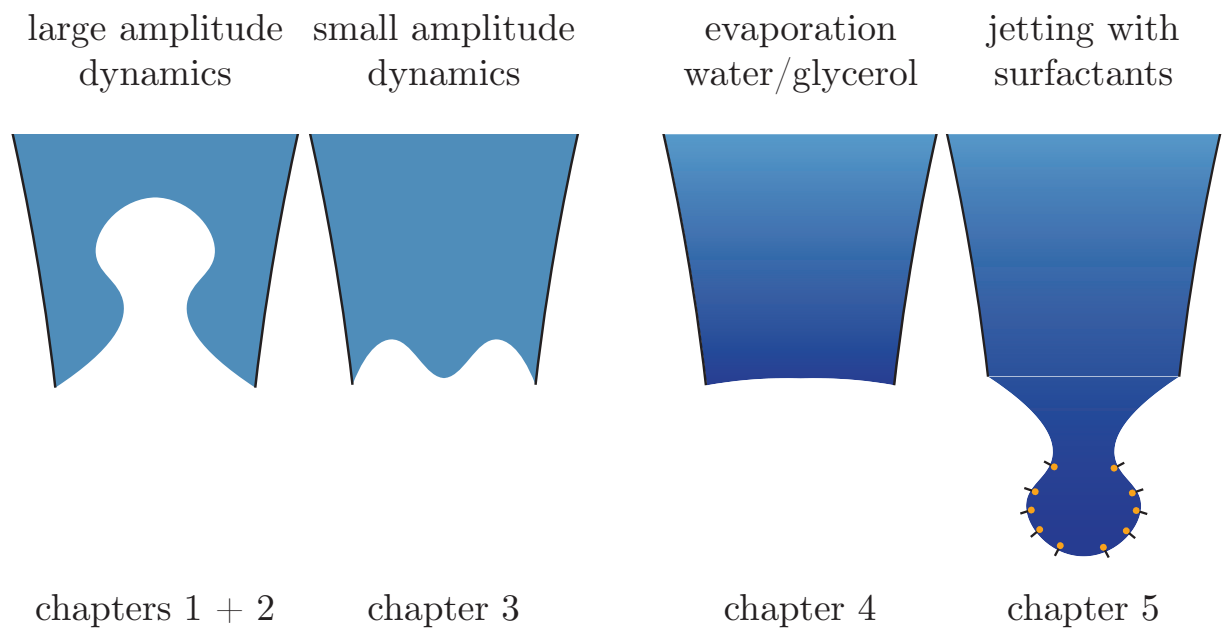
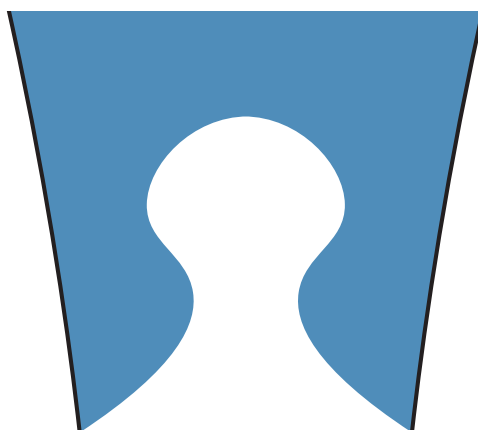


Figure 5: Schematic representation of the content discussed in each chapter of this thesis.

# Meniscus oscillations driven by flow focusing lead to bubble pinch-off and entrainment in a piezoacoustic inkjet nozzle



□

---

Published as: Arjan Fraters, **Maaïke Rump**, Roger Jeurissen, Marc van den Berg, Youri de Loore, Hans Reinten, Herman Wijshoff, Devaraj van der Meer, Detlef Lohse, Michel Versluis, and Tim Segers, *Meniscus oscillations driven by flow-focusing leading to bubble pinch-off and entrainment in a piezo acoustic inkjet nozzle*, Phys. Rev. Applied **16**, 044052 (2021), where Maaïke continued the experiments after Arjan identified the pinch-off phenomenon, and contributed in the finalizing of the manuscript.

## Abstract

The stability of high-end piezoacoustic drop-on-demand (DOD) inkjet printing is sometimes compromised by the entrainment of an air bubble inside the ink channel. Here, bubble pinch-off from an oscillating meniscus is studied in an optically transparent DOD printhead as a function of the driving waveform. We show that bubble pinch-off follows from low-amplitude high-frequency meniscus oscillations on top of the global high-amplitude low-frequency meniscus motion that drives droplet formation. In a certain window of control parameters, phase inversion between the low and high frequency components leads to the enclosure of an air cavity and bubble pinch-off. Although phenomenologically similar, bubble pinch-off is not a result of capillary wave interaction such as observed in drop impact on a liquid pool. Instead, we reveal geometrical flow focusing as the mechanism through which at first, an outward jet is formed on the retracted concave meniscus. The subsequent high-frequency velocity oscillation acts on the now toroidal-shaped meniscus, and it accelerates the toroidal ring outward resulting in the formation of an air cavity that can pinch-off. Through incompressible boundary integral simulations we reveal that bubble pinch-off requires an unbalance between the capillary and inertial time scales and that it does not require acoustics. The critical control parameters for pinch-off are the pulse timing and amplitude. To cure the bubble entrainment problem, the threshold for bubble pinch-off can be increased by suppressing the high frequency driving through appropriate waveform design. The present work therefore aids the improvement of the stability of inkjet printers through a physical understanding of meniscus instabilities.

## 1.1 Introduction

Piezo-inkjet printing is an accurate and contactless method to deposit ink droplets on a substrate [1,3,31]. Droplets are formed on demand from a nozzle by actuating a piezoelectric element. The piezo deforms the channel wall upon electrical stimulation, resulting in acoustic pressure waves that jet the ink out of the nozzle [32]. Piezo-inkjet printing is used in high-end industrial printers for on-demand personalized printing of documents, graphic art, and packaging, the main reason being its high reliability, high print quality, and its compatibility with a wide range of inks. The aforementioned properties also make piezo-inkjet printing also an excellent technique for several emerging ad-

ditive manufacturing applications, such as printing electronics [6,9,10,33–38], pharmaceuticals [13], biomaterials [11,12,39,40], and even the lubrication of ball bearings [14].

Although piezo-inkjet printing is a highly reliable droplet deposition technique, the droplet-formation process is sometimes compromised by the entrainment of an air bubble [17–26]. The entrained air bubble disturbs or even stops the jetting process and thereby dramatically reduces the printing quality and reliability. Previously, several mechanisms have been identified by which bubbles can be entrained in the ink channel. First, on the nozzle plate at the nozzle exit, dirt particles or an ink layer can trigger bubble entrainment by disturbing the jetting process at the nozzle exit [25]. Second, a dirt particle in the ink can trigger bubble nucleation upon its interaction with the oscillating meniscus interface and, third, a bubble can nucleate on the particle through cavitation inception in the rarefaction pressure wave [17]. However, bubbles can also be entrained in the absence of dirt particles or an ink layer, i.e., by yet another physical mechanism. Figure 1.1 shows back-illuminated [41,42] images of such a bubble pinch-off and entrainment event that is observed in a squeeze-type piezo-inkjet printhead with a 70- $\mu\text{m}$ -diameter optically transparent nozzle exit (Microdrop Technologies GmbH, Autodrop Pipette AD-K-501), driven by a rectangular push-pull pulse (amplitude 150 V, width 30  $\mu\text{s}$ ). First, a droplet is ejected and, subsequently, the meniscus retracts back into the nozzle and a bubble pinches off when the meniscus motion reverses from its inward motion to an outward motion, away from the ink channel. Note that the ink appears transparent inside the glass nozzle and dark outside—oppositely to air—due to the similar refractive indices of ink and glass, and their mismatch with that of air. The bubble pinch-off event is shown in more detail in Fig. 1.1(b). The figure shows that the central region of the meniscus moves inward while the outer region of the meniscus moves outward. As a result, an air cavity forms that eventually closes, thereby pinching off an air bubble.

Bubble pinch-off as shown in Fig. 1.1 is found to occur only within certain windows of the piezo driving conditions. This is illustrated in Fig. 1.2, where two examples of a bubble pinch-off window are given for a rectangular pull-push pulse with amplitude  $A$  and width  $\Delta t$  (Fig. 1.2(a)). In the first example in Fig. 1.2(b), the pulse amplitude  $A$  is varied with all other parameters fixed ( $\Delta t = 30 \mu\text{s}$ ). Note from the retracted meniscus amplitude that the injected momentum increases linearly with pulse amplitude, as expected [44]. A win-

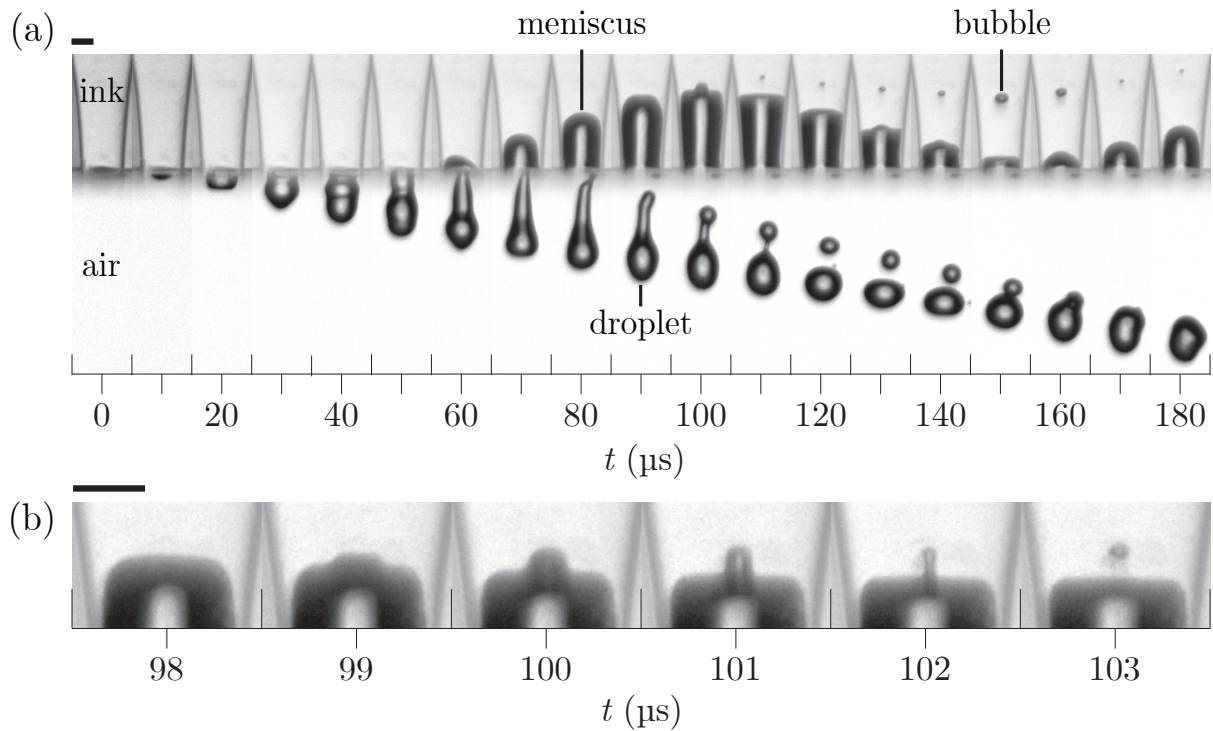


Figure 1.1: (a) Bubble pinch-off and entrainment in a 70- $\mu\text{m}$ -diameter nozzle of a piezo drop-on-demand inkjet printhead. The piezo actuation pulse is a rectangular push-pull pulse with a 150-V amplitude and a 30- $\mu\text{s}$  width. The images are recorded using 8-ns single-flash stroboscopic imaging with illumination by laser-induced fluorescence (iLIF) [43]. (b) Details of the bubble pinch-off process: the center of the meniscus moves inward while the outer region of the meniscus moves outward, leading to the formation of an air cavity that eventually pinches off as an entrained air bubble. The scale bars represent 50  $\mu\text{m}$ .

dow of bubble pinch-off is observed between pulse amplitudes of 140 V and 150 V. Given the nature of meniscus instabilities, meaning that the growth time shortens and the oscillation amplitude increases with increasing acceleration [45–47], it is expected that bubble pinch-off will always occur above a certain threshold amplitude. Surprisingly, no bubble pinch-off is observed at amplitudes larger than 160 V. In the second example [see Fig. 1.2(c)], the pulse width is varied. Bubble pinch-off is observed between pulse widths of 70  $\mu\text{s}$  and 75  $\mu\text{s}$ . The bubble size initially increases and then decreases, with a maximum radius between 72  $\mu\text{s}$  and 73  $\mu\text{s}$ .



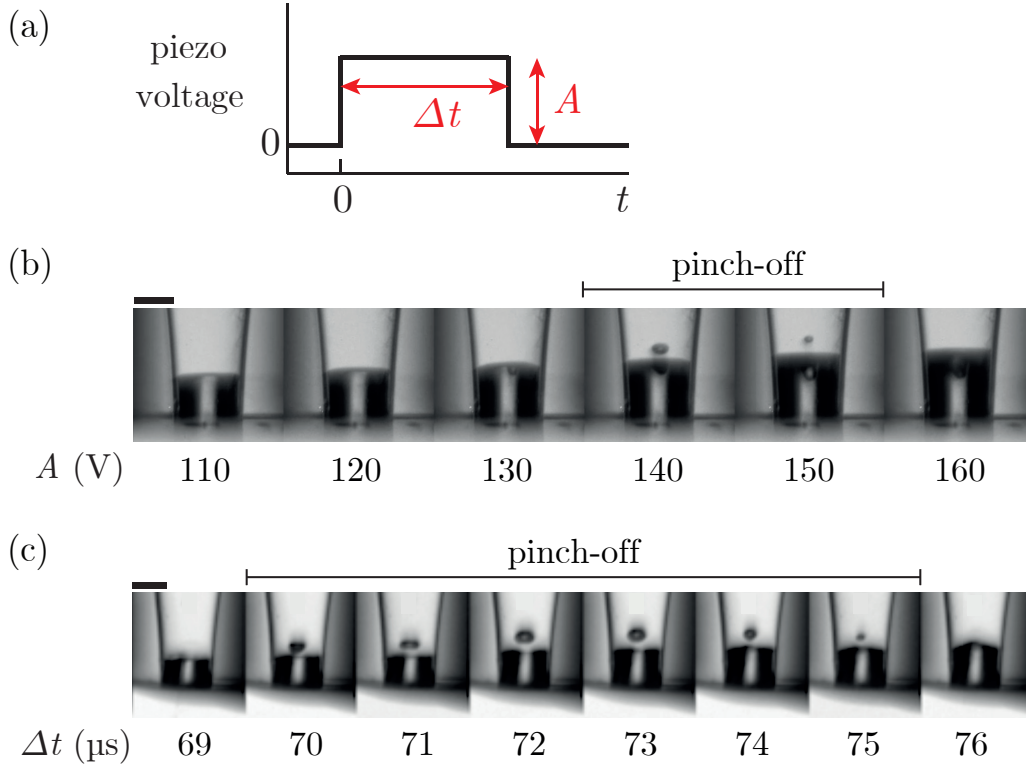


Figure 1.2: (a) A rectangular piezo actuation pulse, with its amplitude  $A$  and length  $\Delta t$  as the control parameters. (b),(c) The window of bubble pinch-off for (b) a pull-push pulse with a pulse width of  $30 \mu\text{s}$  and a varying amplitude and (c) a pull-push pulse with an amplitude of  $94 \text{ V}$  and a varying pulse width. The scale bars represent  $50 \mu\text{m}$ .

An oscillating meniscus can be destabilized by several mechanisms, including the classical Rayleigh-Taylor instability [45, 46, 48] and the parametrically driven meniscus instability [47, 49]. A Rayleigh-Taylor instability grows on a flat interface between two fluids with different density, i.e., in this particular case, the ink and air. The two fluids are accelerated at a rate high enough for the inertial forces to overcome the restoring surface tension. The parametrically driven meniscus instability grows on an initially flat meniscus at the subharmonic of the frequency at which the meniscus is driven (period doubling). The meniscus can also be destabilized at an intermediate Ohnesorge number by an inhomogeneous velocity field at the meniscus, due to the finite transport time of viscous-drag-induced vorticity from the wall to the center of the nozzle [50]. Furthermore, the meniscus can be deformed by geometrical-flow focusing when a pressure wave hits a concave meniscus [51–53]. Finally, meniscus destabilization and resulting bubble pinch-off can originate from the



interaction of capillary waves at the gas-liquid interface. In fact, there is a remarkable similarity between the bubble-entrainment phenomenon in Figs. 1.1 and 1.2 and, in particular, the window of bubble entrainment, with bubble pinch-off during crater collapse in drop impact and that during bubble bursting at the surface of a liquid pool [54–59]. In these cases, bubble entrainment is a result of capillary waves traveling down the cavity that then interact at the base of the cavity, leading to the pinch-off of a bubble. Bubble pinch-off has been shown to require perfect timing of capillary-wave interaction and it thereby depends on both the amplitude and the overall shape of the cavity [54, 57, 59].

The aim of the present study is to find the underlying physical mechanisms that drive bubble pinch-off and entrainment as observed in Figs. 1.1 and 1.2 and to gain fundamental physical insight into the stability of the meniscus in an inkjet nozzle. To that end, after describing the methods for both the experiments and numerics in Section II, the meniscus and bubble dynamics shown in Fig. 1.1 are analyzed in more detail by tracking the meniscus position over time (Section III). The driving of the meniscus by the piezo actuator is further characterized by measuring the ring-down piezosignal. Then the meniscus dynamics of two additional experiments is analyzed to identify the process during which the inner and outer region of the meniscus develop their destabilizing out-of-phase motion. Finally, the mechanisms that drive the development of this out-of-phase motion are identified using numerical simulations with the boundary integral (BI) method [52]. The work ends with conclusions (section IV).

## 1.2 Experimental and numerical methods

### 1.2.1 Printhead and ink

A 70- $\mu\text{m}$ -nozzle-diameter Autodrop Pipette from Microdrop Technologies GmbH (AD-K-501 and AD-H-501) is used [see Fig. 1.3(a)]. Figure 1.3(b) shows the approximate inner dimensions of the functional acoustic part of the printhead. More details about this type of printhead can be found in Refs. [60, 61].

A 4:1 (v/v) mixture of water with glycerol (Sigma-Aldrich, G9012, 1,2,3-Propanetriol,  $\geq 99.5\%$ ) is used as a model ink. All experiments are performed at room temperature. The density, viscosity, and surface tension  $\sigma$

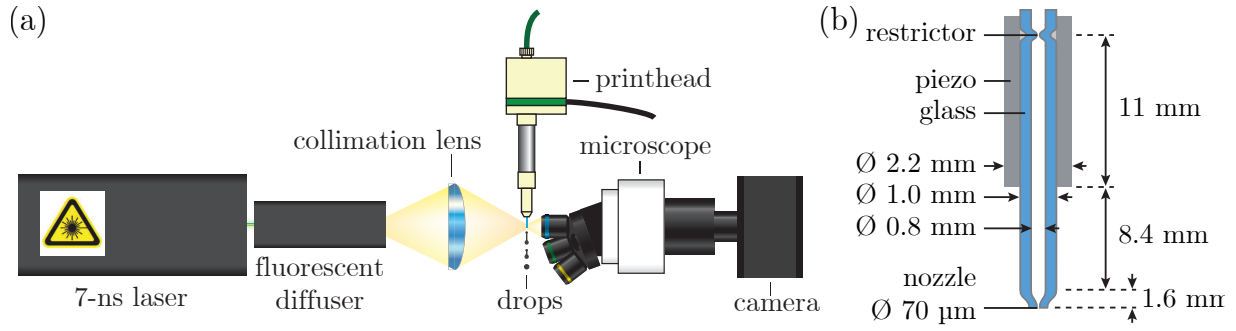


Figure 1.3: (a) The experimental setup employed to image meniscus motion and bubble pinch-off in the drop-on-demand piezoacoustic inkjet nozzle using illumination by iLIF [43]. (b) A schematic layout of the functional acoustic part of the inkjet printhead. It consists of a glass capillary tube (blue) that is tapered towards the 70- $\mu\text{m}$ -nozzle exit. A cylindrical piezo (gray) can be actuated to drive the ink-channel acoustics and the resulting droplet formation.

are taken from literature to be  $1050 \text{ kg/m}^3$ ,  $2.1 \text{ mPa}\cdot\text{s}$ , and  $71 \text{ mN/m}$ , respectively [62, 63]. The model ink is supplied from a plastic syringe to the top of the Autodrop Pipette holder via flexible plastic polyether ether ketone tubing (Upchurch Scientific) and the meniscus is positioned at the nozzle exit by manually adjusting the piston of the syringe.

## 1.2.2 Imaging setup

Bubble pinch-off is recorded using a stroboscopic imaging setup [see Fig. 1.3(a)]. The microscope (Olympus) has a  $5\times$  objective (LMPLFLN5x, numerical aperture of 0.13), a tube lens (U-TLU), and a high-resolution CCD camera (Lumenera, Lw135m,  $1392 \times 1040$  pixels,  $4.65 \mu\text{m}/\text{pixel}$  size). The resulting optical resolution is  $0.93 \mu\text{m}/\text{pixel}$ . The images captured by the camera are saved by custom-made software on a Personal Computer (PC) programmed in the graphical programming language LABVIEW (National Instruments).

The tip of the Autodrop Pipette is illuminated by incoherent 8-ns illumination pulses with a wavelength of  $577 \text{ nm}$  from a laser-induced fluorescence (iLIF) system [43]. The iLIF system consists of a pulsed laser (Quantel EverGreen, dual cavity Nd:YAG,  $\lambda = 532 \text{ nm}$ ,  $7 \text{ ns}$ ), a fluorescent plate embedded in a highly efficient diffuser (Lavision, part nos. 1108417 and 1003144), and a lens to condense the light pulses onto the imaging plane of the microscope.

### 1.2.3 Measurement procedure

A programmable pulse-delay generator (Berkeley Nucleonics Corp., BNC 575) triggers the laser, the camera, and the printhead actuation system with nanosecond precision. The jetting process is kept reproducible by jetting the entrained bubble out after each bubble pinch-off event. To do so, the piezo is actuated by rectangular pulses from two arbitrary waveform generators: one waveform generator (Agilent 33220A, 20 MHz, 14 bit, 50 MS/s) produced one high-amplitude pulse to entrain an air bubble, and the other waveform generator (Wavetek 195, 16 MHz, 12 bit, 40 MS/s) successively produces 49 low amplitude pulses to jet the entrained air bubbles out of the nozzle. The DOD rate is in all cases only 100 droplets/s such that the ink-channel acoustics are completely damped out and the meniscus position restored to its equilibrium position before the start of a new actuation pulse. For every actuation cycle, a custom-made LABVIEW program captured one image during the high-amplitude piezo actuation pulse. The timing of image exposure is controlled by varying the delay of the laser flash with respect to the start of the piezo driving pulse. The delay is varied over a range from 0  $\mu\text{s}$  to 200  $\mu\text{s}$  with steps of 1  $\mu\text{s}$ , to capture the complete drop formation and bubble pinch-off process. Thus, in total, 200 droplets are imaged out of 10 000 piezo actuations, which demonstrates the extremely high degree of reproducibility of inkjet printing.

A laboratory amplifier (Falco System WMA-300, 5 MHz, 2000 V/ $\mu\text{s}$ ) amplifies the pulses from the waveform generators by a factor of 50. Given the 5-MHz amplifier bandwidth, the rise-and-fall time of the rectangular pulses is 0.2  $\mu\text{s}$ . Note, however—from, e.g., Fig. 1.1—that the actual response time of the ink in the nozzle is a little less than 10  $\mu\text{s}$  after applying the driving pulse to the electrical piezo connections at  $t = 0 \mu\text{s}$ . The rectangular piezo driving pulses have an amplitude between 0 V and 160 V and the printhead can be driven in either the push-pull mode or pull-push mode by switching the polarity of the electrical connections at the printhead. With the complete system, droplets are produced with diameters in the range of 70–100  $\mu\text{m}$ , corresponding to volumes of 180–520 pL, and droplet velocities in the range of 1–3  $\text{m s}^{-1}$ .

### 1.2.4 Image analysis

The motion of the meniscus and that of the bubble are tracked as a function of time. First, the contrast in each image is enhanced using ImageJ [64] by subtracting the original image from the image taken at  $t = 0 \mu\text{s}$  and by adding

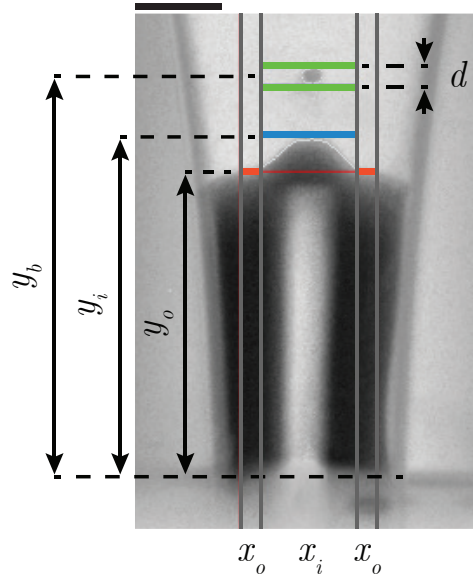


Figure 1.4: An example of an image-analysis result, showing the meniscus positions  $y_o$  of the outer region  $x_o$  and  $y_i$  of inner region  $x_i$ , the bubble position  $y_b$ , and the bubble diameter  $d$ . The scale bar represents  $50\text{ }\mu\text{m}$ .

the inverted result to the original image. Second, the edges of the meniscus and bubble are detected using a script programmed in PYTHON [65]. The script applies a Scikit-Image Canny edge detector to each image, extracts the edges of interest, and calculates their positions. The meniscus is separated in an inner and outer region to quantify the meniscus shape deformation (see Fig. 1.4). The inner region is chosen such that it always confines the bubble, and has a width of 0.6 times the nozzle diameter. The outer region is set to a width of 0.9 times the nozzle diameter. The position of the outer region of the meniscus  $y_o$  is the average position of the detected edge in that region. The position of the inner region of the meniscus  $y_i$  is the maximum or minimum position of the detected edge in that region depending on whether it has a concave or convex shape, respectively. When a bubble is present, its center position  $y_b$  and diameter  $d$  are determined. The bubble diameter is always measured in the axial direction to minimize a potential error in the bubble diameter due to the refraction of light at the cylindrical walls of the glass nozzle that can deform the image. However, optical distortion due to refraction is low for three reasons: (i) due to the similar refractive index of the ink and glass, (ii) because the outer diameter of the glass nozzle (0.4 mm; see Fig. 1.3) is large compared to the nozzle diameter, and (iii) due to the relatively low numerical aperture of the microscope objective. Consequently, light rays from within

the ink in the nozzle region are mostly normal to the glass-air interface upon exiting the glass nozzle toward the microscope objective and, therefore, we do not correct  $y_o$ ,  $y_i$ , and  $y_b$  for refraction. The time-dependent positions  $y_o$ ,  $y_i$ , and  $y_b$  are filtered to extract the amplitudes and dynamics of the low- and high-frequency components of the meniscus motion.

### 1.2.5 Piezo eigenfrequency characterization through ring-down measurements

To characterize the resonance behavior of the piezo, the ring-down of the piezo is measured using a piezo sensing technique described in Refs. [1, 25]. The piezo is driven using an electrical pulse. Subsequently, when the driving voltage dropped below 1 V, the piezo contacts are connected automatically to an oscilloscope that records the ring-down voltage oscillations of the piezo, giving its characteristic resonance frequency.

### 1.2.6 Boundary integral simulations

To study the bubble pinch-off process and the underlying physical mechanisms in greater detail, BI simulations are performed [52]. The utilized BI code is axisymmetric and assumes irrotational, incompressible, and inviscid flow [66–69]. In essence, the unsteady Bernoulli equation,

$$\frac{\partial \phi}{\partial t} = -\frac{1}{2} |\nabla \phi|^2 - \frac{\Delta p + \kappa \sigma}{\rho}, \quad (1.1)$$

is time integrated as described in Ref. [52]. In Eq. 1.1,  $\phi$  is the flow potential,  $\Delta p$  is the pressure variation,  $\kappa$  is the curvature, and  $\sigma$  and  $\rho$  are the liquid surface tension and density, respectively. Owing to the micron-sized meniscus, we neglect gravity. The inviscid assumption is appropriate here, as in the experiments it is observed that the meniscus shape deformation is the largest at low viscosity and decreases as the ink viscosity increases. The numerical setup consists of a nozzle wall (solid boundary) and a meniscus (free boundary). The flow in the nozzle is driven by applying a stream-velocity boundary condition to the nodes at the entrance of the nozzle.

Two methods are used sequentially to describe the contact-line dynamics of the meniscus; a fixed contact line and a moving contact line based on contact-angle hysteresis, with a receding contact angle  $\theta_r$  and an advancing contact angle  $\theta_a$ . The combination of these two methods provides a good balance between

approximating the experimentally observed meniscus motion and preventing numerical instabilities. These occur when the distance between the free boundary and solid boundary becomes too small. At the start of each simulation, the contact line is kept pinned. If, during this first time period, one of the nodes of the meniscus comes within a distance from the wall that will cause numerical instability, the meniscus between that node and the contact line is cut off and a new contact line is created near this node. This intervention does not have a significant effect on the bubble pinch-off phenomena in the simulations. Once the contact angle becomes larger than  $\theta_a$ , the moving-contact-line method is initiated. This method keeps the contact line pinned for  $\theta_r < \theta < \theta_a$ ; moves the contact line to  $\theta = \theta_r$  if  $\theta < \theta_r$ , and moves the contact line to  $\theta = \theta_a$  when  $\theta > \theta_a$ .  $\theta_r$  and  $\theta_a$  are set to the maximum angle away from  $90^\circ$  for which the meniscus motion near the wall remains stable during the simulations, i.e.  $\theta_r = 72^\circ$  and  $\theta_a = 108^\circ$ . At larger angles away from  $90^\circ$ , numerical instabilities will develop on the meniscus because of the too small distance between the free boundary and the solid boundary, as before.

## 1.3 Results & discussion

### 1.3.1 Meniscus and bubble dynamics

The data shown in Fig. 1.1 are now analyzed in more detail. Figure 1.5(a) shows the positions of the outer and inner regions of the meniscus ( $y_o$ ,  $y_i$ ) and that of the bubble ( $y_b$ ) as a function of time. Note that just before pinch-off, a phase difference  $\Delta\varphi$  develops between the inner and outer regions of the meniscus, eventually leading to phase inversion. This is the crucial opposing motion between the central cavity and the outer region of the meniscus that leads to bubble pinch-off, as is observed in Fig. 1.1(b). The process that is responsible for this phase difference is analyzed in Section 1.3.3. Also note in Fig. 1.5(a) that both the meniscus-position curve and the bubble-position curve have a high-amplitude low-frequency motion of the order of 10 kHz (100- $\mu$ s period) with, superimposed, a low-amplitude high-frequency motion of the order of 100 kHz (10- $\mu$ s period). The low-frequency motion of the meniscus and bubble are indicated by the dashed curve and by the dash-dotted curve, respectively.

The high-frequency component in the meniscus motion  $\Delta y_o$  and that of the bubble motion  $\Delta y_b$  are plotted in Fig. 1.5(b). In addition, in Fig. 1.5(b) the

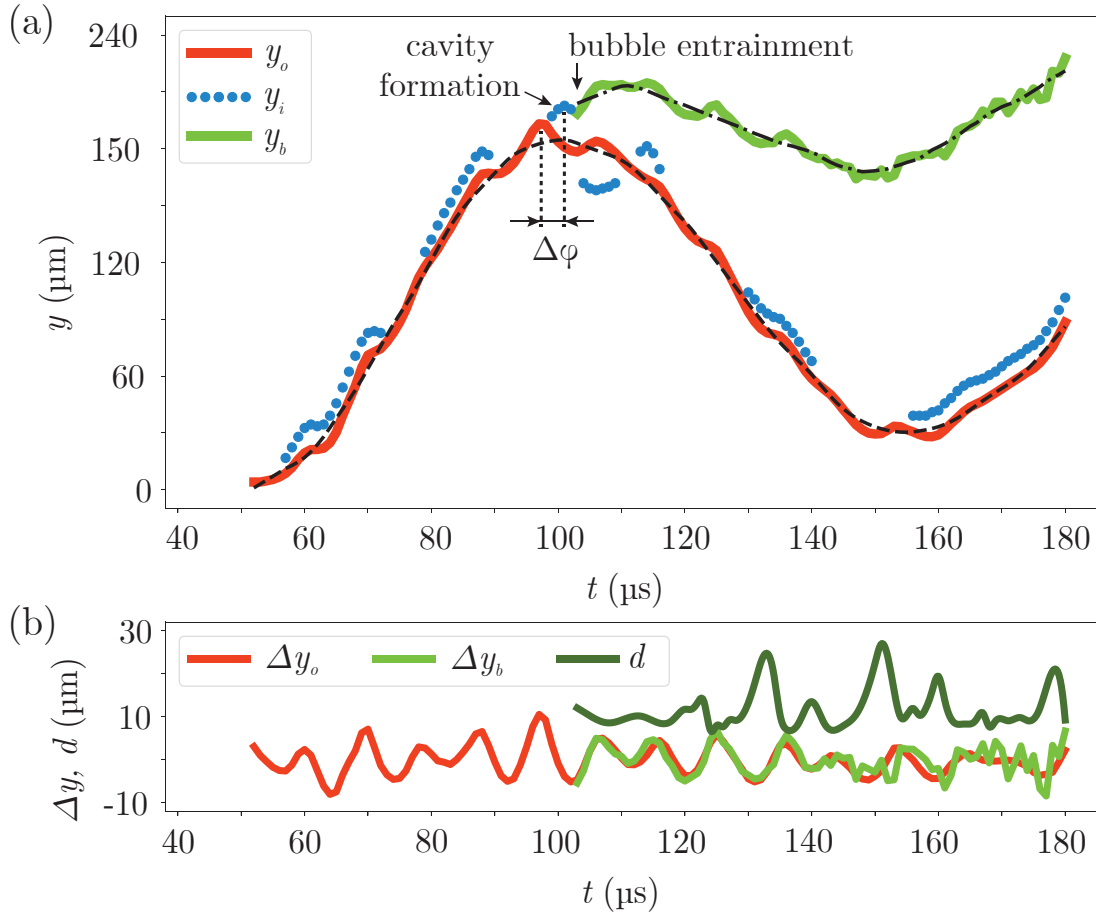


Figure 1.5: (a) The meniscus outer,  $y_o$ , and inner,  $y_i$ , positions and bubble position,  $y_b$ , as functions of time after the start of piezo actuation. The black dashed line and the black dash-dotted line show the low-frequency (low-pass-filtered red curve) motion of the meniscus outer region and that of the bubble (low-pass-filtered green curve), respectively. (b) The high-frequency [high-pass filtered red curve in (a)] movement of the meniscus outer-region position,  $\Delta y_o$ , and that of the bubble position,  $\Delta y_b$ . The dark green curve shows the bubble diameter,  $d$ , as function of time.

bubble diameter  $d$  is plotted as a function of time. The bubble equilibrium radius is  $5 \pm 1 \mu\text{m}$ , which corresponds to a Minnaert eigenfrequency [70] of approximately 600 kHz. As this is much higher than the observed bubble oscillation frequency of 100 kHz, the radial dynamics of the bubble is considered to oscillate in phase with that of the pressure waves inside the ink channel [71]. Therefore, the bubble radius directly represents the local pressure, i.e. the maximum in bubble radius corresponds to a minimum pressure, and vice versa. Note in Fig 1.5(b) that the bubble diameter, the bubble po-



sition, and the meniscus position all oscillate at a frequency of  $105 \pm 5$  kHz. Also note that the meniscus and bubble are moving inward around the time that the bubble diameter is maximum (pressure minimum), while the meniscus and bubble start moving outward when the bubble diameter is minimum (pressure maximum). Thus, the meniscus and the bubble are driven by the same high-frequency pressure waves, and not by their individual eigenmodes.

It may be noted that next to bubble entrainment, Fig. 1.1 shows another typical inkjet phenomenon named 'tail-hooking': When the meniscus retracts into the nozzle the tail sweeps toward a nozzle side to reduce its surface energy [48,72]. Tail-hooking typically induces an off-axis jet angle and in Fig. 1.1 it also results in the deposition of a tiny sessile droplet on the nozzle plate (indicated by the arrow). However, since stroboscopic imaging is used here, i.e., every image shows a different droplet, it can be concluded that the jetting process is highly robust and reproducible. This can also be observed from the absence of any discontinuities in the position and size of the sessile droplet, the bubble, and the jetted droplet.

### 1.3.2 Piezo actuator characterization

To determine whether the piezo actuator is the origin of the high-frequency pressure oscillations, the eigenmodes of the piezo are characterized by measuring the ring-down signal of the piezo for an empty ink channel. The piezo is first actuated using a pull-push pulse with an amplitude  $A$  of 10 V, a full-width-at-half-maximum (FWHM) pulse width  $\Delta t$  of 72  $\mu$ s, and a rise-and-fall time  $\Delta e$  of 1  $\mu$ s [see Fig. 1.6(a)]. The ring-down signal and its Fourier spectrum are plotted in Fig. 1.6(b) and 1.6(c). Indeed, in the ring-down signal the same 105-kHz high-frequency component is present as in the meniscus motion, the bubble motion, and the radial dynamics in Fig. 1.5(b). The piezo eigenmode frequencies are calculated from its dimensions (Fig. 1.3) and the speed of sound in piezoceramic (approximately 4000 m/s) to be  $111 \pm 12$  kHz in longitudinal direction and  $3.4 \pm 0.1$  MHz in radial direction [73,74]. Thus, the 105-kHz high-frequency component in the piezo ring-down signal originates from the longitudinal resonance mode of the piezo and the pressure waves produced by this resonance mode drive the high-frequency motion of the meniscus in the nozzle. Indeed, when the high-frequency component is suppressed by using a  $\Delta e$  of 9  $\mu$ s [see Fig. 1.6(b) and 1.6(c)] also the high-frequency motion of the meniscus is suppressed [see Fig. 1.6(d)].



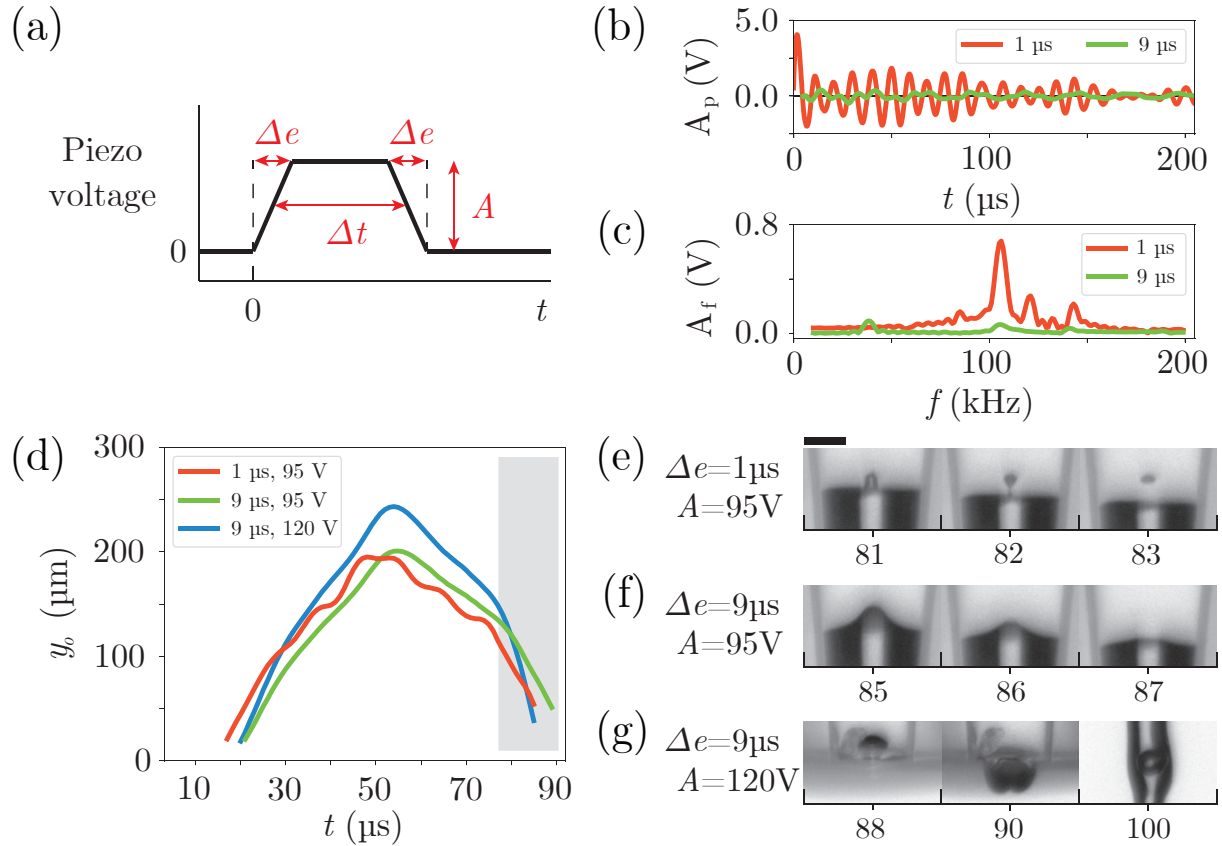


Figure 1.6: (a) A piezo actuation pulse with amplitude  $A$ , FWHM pulse width  $\Delta t$ , and rise-and-fall time  $\Delta e$ . (b),(c) Piezo (b) ring-down measurements with (c) the corresponding Fourier spectra, for a pull-push pulse with  $A = 10$  V,  $\Delta t = 72 \mu$ s, and values of  $\Delta e$  as indicated in the legend. (d) The meniscus motion for three pulses with  $\Delta t = 72 \mu$ s and with  $\Delta e$  and  $A$  as given in the legend. Bubble entrainment takes place in the gray-shaded time window. (e-g) Images of the nozzle taken during the time window indicated by the gray-shaded time window in (d), showing whether or not bubble pinch-off takes place. The numbers under the images correspond to the time in  $\mu$ s in (d). The scale bar represents  $50 \mu$ m.

Notably, the absence of the 105-kHz high-frequency pressure waves also prevents bubble pinch-off [see Fig. 1.6(f) in comparison to Fig. 1.6(e)]. In the experiment shown in Fig. 1.6(f), an air cavity is still formed but it does not pinch off a bubble. This cavity can be forced to pinch off in the same way as before, but at a different meniscus position and time, by increasing the amplitude of the piezo driving to 120 V [see Fig. 1.6(g)]. Thus, suppressing the high-frequency pressure waves effectively increases the threshold for

bubble pinch-off from 95 V to 120 V. In other words, the high-frequency pressure waves from the longitudinal resonance mode of the piezo promote bubble pinch-off and, through suppression of the 105 kHz waves, the driving amplitude can be increased, allowing for stable inkjet printing at a higher droplet velocity.

### 1.3.3 Meniscus shape deformation process

Now that the driving mechanisms of the meniscus are identified, next, the process responsible for the development of the phase difference between the inner and outer regions of meniscus, eventually leading to phase inversion and bubble pinch-off, can be identified. The phase difference  $\Delta\varphi$  [Fig. 1.5(a)] develops through the meniscus shape deformation process that can be observed in Fig. 1.7: it develops by jet formation at a concave meniscus. The universality of the meniscus shape deformation process prior to bubble pinch-off is demonstrated in Fig. 1.7 by its presence in two bubble pinch-off experiments with entirely different driving conditions, namely, with piezo driving pulses with opposite polarity. In the first experiment, the piezo is actuated using a rectangular push-pull pulse ( $A = 160$  V,  $\Delta t = 30$   $\mu$ s). A bubble is entrained after droplet formation, and it remains inside the nozzle [see Fig. 1.7(a)]. In the second experiment, the piezo is actuated using a rectangular pull-push pulse ( $A = 150$  V,  $\Delta t = 30$   $\mu$ s). In contrast to the first experiment, a bubble is entrained before droplet formation and it is ejected with the droplet shortly after entrainment [see Fig. 1.7(b)]. Despite the large differences between the two experiments, the image sequences and graphs in Figs. 1.7(c)-1.7(f) show that the meniscus shape deformation process is qualitatively the same for the two experiments. Initially, upon retraction, the meniscus has a concave shape. Then, during the advancing of the meniscus, a small liquid jet is formed in outward direction. Later, this jet recoils back inward, while the outer region of the meniscus is forced to move outward again, in the opposite direction of the movement of the jet. Similar to the experiment in Fig. 1.1, the opposing motion of the outer and inner regions of the meniscus leads to the formation and closure of a cavity and thereby to the pinch-off of a bubble. Thus, phase inversion between the inner and outer region of the meniscus is a consequence of jet formation at the central part of the concave meniscus. The qualitative differences between the meniscus shapes in Figs. 1.7(c) and 1.7(d), e.g., the flatter meniscus in (d) as compared to (c), underpin the complex nonlinear behavior of the inkjet nozzle.

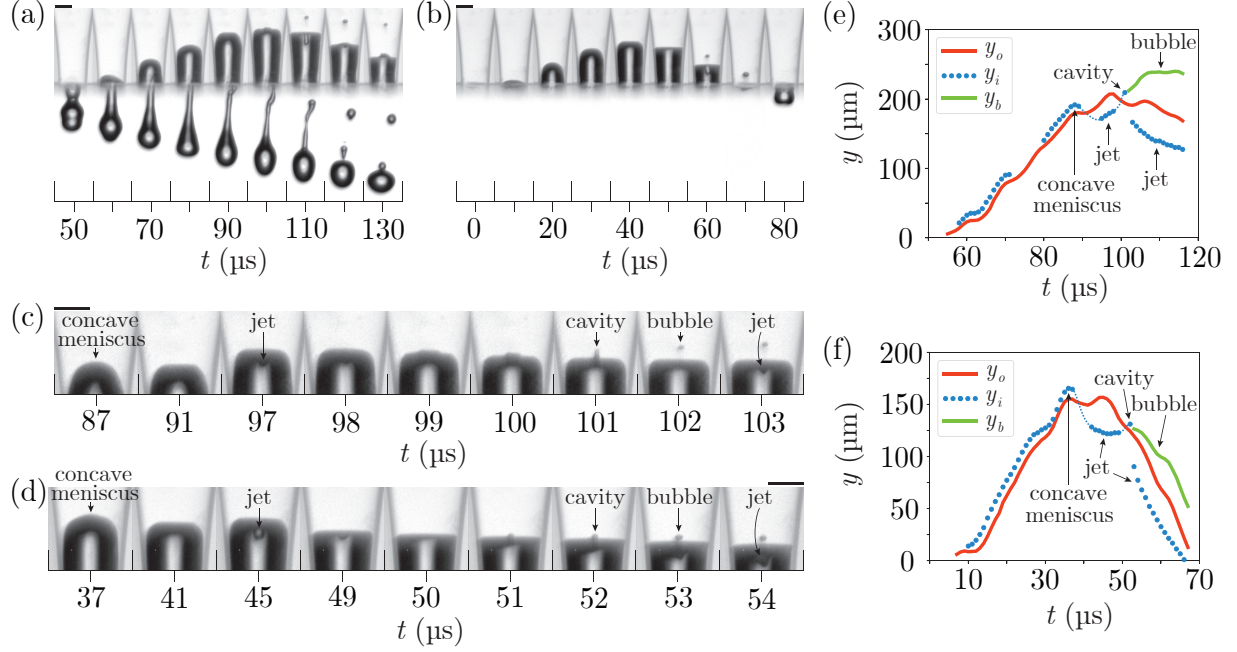


Figure 1.7: Bubble pinch-off for (a) a rectangular push-pull pulse with an amplitude of 160 V and a width of 30  $\mu\text{s}$  and (b) a rectangular pull-push pulse with an amplitude of 150 V and a width of 30  $\mu\text{s}$ . (c, d) Details of the meniscus shape deformation process prior to, during, and after bubble pinch-off for the push-pull and the pull-push pulse, respectively. (e, f) The meniscus outer-region position  $y_o$ , inner region position  $y_i$ , and bubble position  $y_b$  as function of time for the push-pull and pull-push pulse, respectively. The thin blue dashed line is added to guide the eye in the parts of the jet-formation and jet-recoil process where the position of the inner region of the meniscus cannot be tracked. The scale bars represent 50  $\mu\text{m}$ .

### 1.3.4 Jet formation mechanism

From literature it is known that when a pressure wave propels a concave-shaped meniscus forward, a jet forms due to geometrical focusing of the flow at the meniscus due to an inhomogeneous pressure gradient field along the meniscus [52][53]. The pressure gradient and the resulting velocity are larger at the center of a concave meniscus than at its edge (see also Ref. [51]). Thus, in the inkjet nozzle, first, the inward motion of ink results in a concave shaped meniscus, then a first outward acceleration creates a phase difference between the inner and outer regions of the meniscus by the formation of a central outward-moving liquid jet, and, finally, a well-timed second outward acceleration enhances this phase difference by the formation of a toroidal outward-

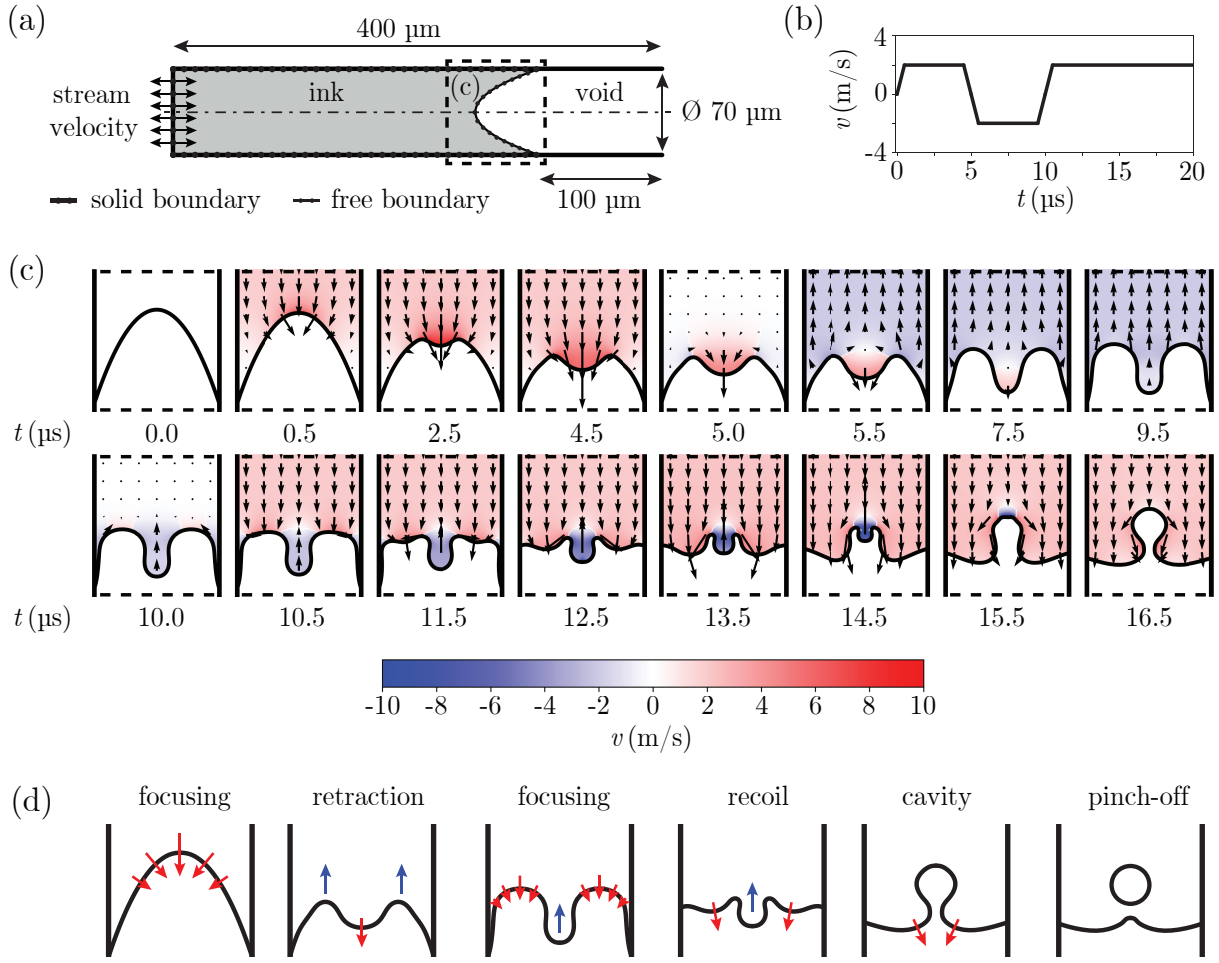


Figure 1.8: (a) The numerical setup for the (BI) simulation, where the left boundary is subject to a stream-velocity boundary condition. The initial meniscus shape is a parabola with a depth of 0.75 times the nozzle diameter. (b) The stream-velocity boundary condition  $v$  for the numerical setup as function of time with a 100-kHz velocity oscillation followed by an outward-directed flow. (c) The meniscus shape deformation process prior to bubble pinch-off, simulated using the BI method. (d) A schematic summary of the main steps in (c).

moving liquid jet. The central liquid jet recoils inward and forms an air cavity that is enclosed by the toroidal outward-moving liquid jet, and as a consequence, a bubble pinches off.

To further demonstrate the details of the proposed pinch-off mechanism, numerical simulations are performed using the BI method. The results are shown in Fig. 1.8. The geometry of the numerical setup in Fig. 1.8(a), and the stream-

velocity boundary condition  $v(t)$  in Fig. 1.8(b), are chosen such that they follow the experimental conditions, i.e., the nozzle diameter and the 100-kHz oscillations that are identified to drive bubble pinch-off. The initial meniscus shape [Fig. 1.8(c)] and the imposed amplitude of the 100-kHz velocity boundary condition [Fig. 1.8(b)] are varied and, as in the experiments, only for highly specific combinations of the two, the meniscus shape deformation process develops toward bubble pinch-off. In the simulation, we thus start with a retracted concave meniscus with a parabolic and undisturbed profile, as observed in the experiments up to a time of approximately  $80 \mu\text{s}$  in Fig. 1.1 and  $87 \mu\text{s}$  in Fig. 1.7. A simulation result is shown in Fig. 1.8(c). The figure reveals the amplitude and the direction of the ink velocity, and demonstrates how the velocity field inhomogeneity and the focusing of the flow at the concave part of the meniscus drive the jet formation. Moreover, Fig. 1.8(c) highlights the opposing motion between the central jet and the toroidal jet and shows in detail how this opposing motion leads to the formation of a cavity that closes and pinches off a bubble. The main steps in this process, which are discussed in detail earlier, are now schematically summarized in Fig. 1.8(d): a central jet forms at the concave meniscus during the first outward acceleration; then, a toroidal jet forms at the concave meniscus around the central jet during the second outward acceleration; and, finally, the recoiling central jet forms a cavity and the progressing toroidal jet encloses this cavity, with bubble pinch-off as a result.

Note that even though the BI simulations are incompressible, we observe the same meniscus deformation process as in the experiments, suggesting that the meniscus shape deformation process responsible for bubble pinch-off does not require acoustics but that a certain unbalance between the capillary and inertial time scales is sufficient. Indeed, the capillary time scale ( $\tau_c = \sqrt{\rho R^3/\sigma}$ , with  $R$  the nozzle radius) for the present inkjet nozzle is approximately  $24 \mu\text{s}$ , whereas the inertial timescale is of the order of  $1 \mu\text{s}$ , i.e., set by the rise and fall time of  $v(t)$  in Fig. 1.8(b). Furthermore, from the input velocity boundary condition  $v(t)$  and Eq. 1.1 the dynamic driving pressure in the BI simulations can be calculated, as follows:  $\Delta p = \Delta p_a + \Delta p_i = -\rho \frac{\partial \phi}{\partial t} - \frac{1}{2} \rho U^2$ , with  $\Delta p_a$  and  $\Delta p_i$  the pressure contributions from acceleration and inertia, respectively. The magnitude of  $\Delta p_i$  is directly estimated from  $v(t)$  as 8 kPa. The magnitude of  $\Delta p_a$  can be estimated as  $\rho U L / \Delta t \approx 1.4\text{--}12 \text{ bar}$ , where  $U$  the velocity variation (4 m/s) over time  $\Delta t$  [ $1 \mu\text{s}$ ; see Fig. 1.8(b)] and  $L$  a length scale between the nozzle radius ( $35 \mu\text{m}$ ) and the fluid-filled domain

[300  $\mu\text{m}$ ; see Fig. 1.8a]. Note that since the BI simulations are incompressible, these dynamic pressure fluctuations are to be compared with acoustic pressure fluctuations in the experiment. The order of magnitude of the dynamic driving pressure amplitude is in line with values reported for the acoustic driving pressure in inkjet printing [1, 17], which once more shows that acoustic wave propagation is not required for the observed bubble pinch-off phenomenon and that it is a flow-dominated process.

### 1.3.5 The bubble pinch-off window

Using the knowledge acquired on the underlying physics of the bubble pinch-off phenomenon studied in this work, we now qualitatively explain the observed parameter windows of bubble pinch-off in Fig. 1.2. In Fig. 1.2(b), the pulse width  $\Delta t$  is fixed and the amplitude  $A$  is varied. At an amplitude of 130 V and lower, the velocity difference between the recoiling central jet and the progressing toroidal jet is not high enough to form a sufficiently deep cavity at the right moment in time and to enclose this cavity. At an amplitude of 160 V, the central jet has such a length and inertia that it is too slow to recoil before the toroidal jet reaches the central axis. As a result, the toroidal jet encloses the base of the central jet, which in multiple experiments and simulations has been observed to result in the formation of a toroidal bubble such as shown experimentally in Fig. 1.9(a) and from a BI simulation in Fig. 1.9(b).

In Fig. 1.2(c), the amplitude  $A$  is fixed and the pulse width  $\Delta t$  is varied. In other words, the control parameter in these experiments is the timing of the outward acceleration of the meniscus by the falling edge of the piezo driving pulse. In the experiments shown in Fig. 1.2(c), the central jet has already been formed before the falling edge of the pulse. At the different times of meniscus acceleration, the meniscus shape is different and thus the toroidal jet-formation process is different. At  $\Delta t = 69 \mu\text{s}$ , the acceleration is too early, i.e. the central jet is not able to develop sufficient opposing motion with respect to the toroidal jet because of its early formation. At  $\Delta t = 76 \mu\text{s}$ , the acceleration is too late, i.e. the meniscus is propelled outward while the cavity is already present; thus, the central cavity is propelled outward faster than the outer region of the meniscus.

Despite the acquired knowledge on the underlying physics of the bubble pinch-off mechanism, it remains difficult to predict where exactly in the piezo driving parameter space bubble pinch-off will occur, as is also the case for bubble



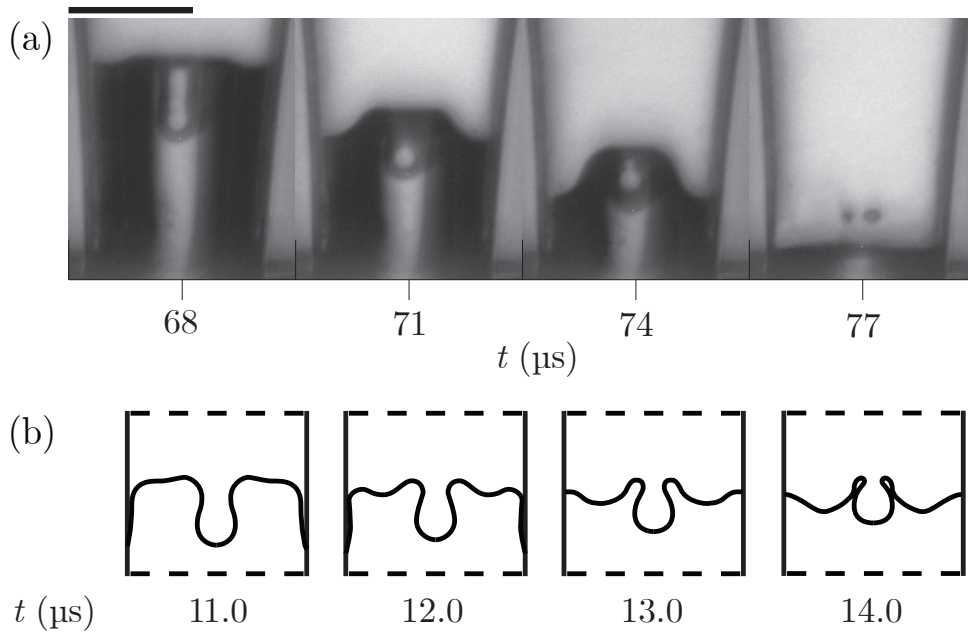


Figure 1.9: (a) Toroidal bubble pinch-off as experimentally recorded for a rectangular pull-push pulse with an amplitude of 92 V and a width of 53  $\mu\text{s}$ . The scale bar represents 50  $\mu\text{m}$ . (b) A simulation using the BI method of the meniscus shape deformation process eventually leading to toroidal bubble pinch-off.

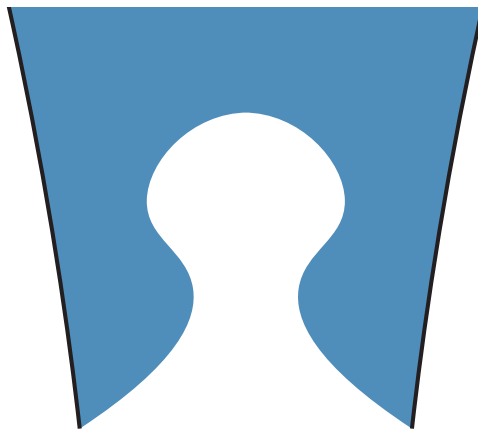
pinch-off after drop impact on a liquid pool [54, 57]. The two main reasons are the sensitivity of the mechanism to the operating conditions and the unavailability of information about the exact printhead configuration and its detailed acoustic properties. However, also in printheads with different dimensions and thus different driving acoustics, the authors have observed highly similar meniscus deformation and pinch-off processes. As a practical guideline, bubble pinch-off can be suppressed with relative ease by suppressing the high-frequency component in the acoustics through the edge duration of the piezo driving pulse. Another simple method, which is not studied here, is to damp out the meniscus shape deformations by increasing the ink viscosity. However, this requires higher driving amplitudes to produce droplets at equal velocity and reduces the universal applicability of the technique. The role of ink viscosity on meniscus deformations due to flow focusing in an inkjet nozzle will be part of future work, as well as remaining questions as to the physics that dictates the size of the entrained bubble.

## 1.4 Conclusions

An oscillating meniscus in a piezo-inkjet nozzle can pinch off a bubble in a specific window of driving conditions, thereby excluding the Rayleigh-Taylor instability as the primary driving mechanism. Pinch-off is the result of the closure of a central air cavity in the meniscus that forms due to opposing motion between a central region and an outer region of the meniscus. The opposing motion between the central region and outer region of the meniscus is the result of jet formation at the concave meniscus. We reveal that jet formation is driven by flow focusing, i.e., due to the inhomogeneous pressure gradient field along the meniscus, as is confirmed by the BI simulations. The process that is responsible for the bubble pinch-off can be summarized as follows. The meniscus gains a concave shape due to inward motion. Subsequently, a first outward acceleration produces a central jet at the concave meniscus. A well-timed second outward acceleration produces a toroidal jet at the concave meniscus around the central jet. The recoiling central jet forms a central air cavity while the progressing toroidal jet encloses this air cavity. Eventually, this leads to pinch-off of an air bubble. These results contribute to a fundamental understanding of the stability of the oscillating meniscus in an inkjet printhead and thereby provide ways to increase the stability of inkjet printing, such as the suppression of higher harmonics of the fundamental resonance mode of the ink channel by changing the piezo driving pulse rather than the nozzle or piezo design. The results from the incompressible BI simulations suggest that bubble pinch-off requires a certain unbalance between the capillary and inertial time scales and that it is therefore a flow-driven phenomenon that does not require acoustics. Future work will focus on further elucidating the role of liquid viscosity and meniscus velocity on bubble pinch-off and entrainment.



Vorticity-induced flow-focusing leads to bubble  
entrainment in an inkjet printhead: synchrotron  
X-ray and volume-of-fluid visualizations



□

---

To be submitted as: **Maaïke Rump\***, Youssef Saade\*, Uddalok Sen, Kamel Fezzaa, Michel Versluis, Detlef Lohse, and Tim Segers, *Vorticity-induced flow-focusing leads to bubble entrainment in an inkjet printhead: synchrotron X-ray and volume-of-fluid visualizations*.

\*Both authors contributed equally.

## Abstract

The oscillatory flows present in an inkjet printhead can lead to strong deformations of the air-liquid interface at the nozzle exit. Such deformations may lead to an inward directed air jet with bubble pinch-off and the subsequent entrainment of an air bubble, which is highly detrimental to the stability of inkjet printing. Understanding the mechanisms of bubble entrainment is therefore crucial in improving print stability. In the present work, we use ultrafast X-ray phase-contrast imaging and direct numerical simulations to study the mechanisms underlying bubble entrainment in a piezo-acoustic printhead. We first demonstrate good agreement between experiments and numerics. We then show the different classes of bubble pinch-off obtained in experiments, and that were also captured numerically. The numerical results are then used to show that the baroclinic torque that is generated at the gas-liquid interface due to the misalignment of density and pressure gradients, results in a flow-focusing effect that drives the formation of the air jet from which a bubble can pinch-off.

## 2.1 Introduction

Drop-on-demand inkjet printing is an accurate, non-contact, and highly reproducibly droplet deposition method that can be used to print liquids with a wide range of physical properties [1-4]. Today's applications of inkjet printing reach far beyond printing graphics on paper as inkjet technology is now used for the fabrication of electroluminescent displays [6,7], electronic circuits [8-10], and biomaterials [11-13].

Even though inkjet printing is a highly reproducible droplet deposition technique, the stability of the jetting process is at times hampered by the entrainment of a bubble [18-24]. The entrained bubble compromises the channel's incompressibility and it thereby disturbs the acoustics in the printhead and can even stop the entire jetting process [17,25,26]. As applications of inkjet printing rely on the stability and reproducibility of the droplet formation process, it is crucial to understand the physical mechanisms of the bubble entrainment process.

Several bubble entrainment mechanisms have been identified. First, an ink layer or particles on the nozzle plate can result in bubble entrainment upon

their interaction with the ink jet during its ejection from the nozzle [25,75]. Second, bubbles can nucleate on microparticles present in the ink due to cavitation during the rarefactional pressure wave or upon their direct interaction with the oscillating meniscus [17]. Third, bubbles can be entrained through direct bubble pinch-off from the oscillating meniscus, e.g. as a result of asymmetric meniscus oscillations [48,76]. Bubble entrainment mechanisms are typically stochastic, where the probability of bubble entrainment increases exponentially with the driving amplitude [17]. At high driving amplitudes, however, bubble entrainment due to meniscus instabilities can become deterministic, as we have shown before using an optically transparent printhead [76]. Here, the high-frequency flow oscillations in the printhead can result in the formation of an air jet on the retracted concave meniscus [76]. The tip of the air jet can pinch-off, resulting in bubble entrainment. We used inviscid irrotational boundary integral (BI) simulations to identify flow-focusing as the physical mechanism that drives this meniscus instability leading to deterministic bubble pinch-off. Geometrical flow-focusing is the process where, when a pressure wave arrives at a concave part of the meniscus, the inhomogeneous pressure gradient field along the meniscus leads to the formation of a jet [51,53,77–79]. However, as we used inviscid and irrotational BI simulations, a direct comparison between experiment and numerics was not feasible. Therefore, open questions remain as to the role of viscosity and vorticity on the bubble pinch-off mechanism driven by flow focusing. A direct comparison between experiment and numerics was further complicated by the refractive index mismatch between ink and air, which masks certain regions of the curved meniscus. As such, only part of the meniscus oscillations could be visualized in high-speed microscopy.

X-rays do not suffer as much from refraction at a curved interface (see Fig. 2.1d) as visible light rays, due to the short wavelength of the photons. High-energy X-rays are typically produced in a synchrotron. Ultrafast X-ray phase-contrast imaging has been previously used to study droplet coalescence [80], drop impact on liquid pools [81,82] and substrates [83,84], and droplet formation in drop-on-demand inkjet printing [85]. The frame rate in the synchrotron is limited to 270 kHz by the roundtrip of electrons in the storage ring [86]. However, stroboscopic high-speed imaging can be performed using multiple interleaved high-speed recordings to reach an equivalent frame rate of 2 million frames per second. A prerequisite for stroboscopic imaging is a fully deterministic and reproducible process, which turned out from earlier experimentation in

the case for the bubble pinch-off phenomenon studied here [76].

In the present study, we investigate the physics governing the geometric flow-focusing mechanism of bubble entrainment in a piezoacoustic printhead. The detailed meniscus oscillations are visualized using ultrafast phase contrast X-ray imaging, which allowed us to not only capture the complete interface dynamics, but also to extract the displaced volume, and thereby the flow rate. The experimentally obtained flow rate provides the input for our direct numerical simulations (DNS) performed using the volume of fluid (VoF) method, which was previously successfully used in studies involving drops and bubbles [87–91]. We use the simulations to unravel the intricate local flows during the bubble entrainment process, which reveal the origin of the geometric flow-focusing mechanism in our printhead. We furthermore use the numerics to study the influence of viscosity and vorticity on the bubble pinch-off process.

The work is organized as follows. In [section 2.2] and [section 2.3], the experimental and numerical methods are described, respectively. Then, in [subsection 2.4.1], the comparison between the experiments and numerics is discussed. The different observed bubble pinch-off classes are presented in [subsection 2.4.2]. In [subsection 2.4.3], we describe our findings on the mechanism of bubble entrainment via geometrical flow-focusing. The work ends with the conclusions in [section 2.5].

## 2.2 Ultrafast X-ray phase contrast imaging

### 2.2.1 Set-up and procedure

A schematic of the experimental imaging setup is shown in Fig. [2.1a]. The experiments were performed at the 32-ID undulator beamline at the Advanced Photon Source of the Argonne National Laboratory with the storage ring in hybrid mode. In this hybrid mode, 84% of all electrons stored in the synchrotron storage ring are collected in a bunch. The electrons produce X-rays as they are forced through an undulating trajectory by magnetic structures. These X-rays can be released unto the set-up by opening a shutter. The resulting X-ray illumination pulse has a duration of 472 ns and a peak irradiance of  $10^{14}$  ph/s/mm<sup>2</sup>/0.1%bw [80]. The shutter releasing the X-rays, the printhead, and the high-speed camera (Photron Fastcam SA-Z) were synchronized to the passing of the electron bunch in the storage ring using delay genera-

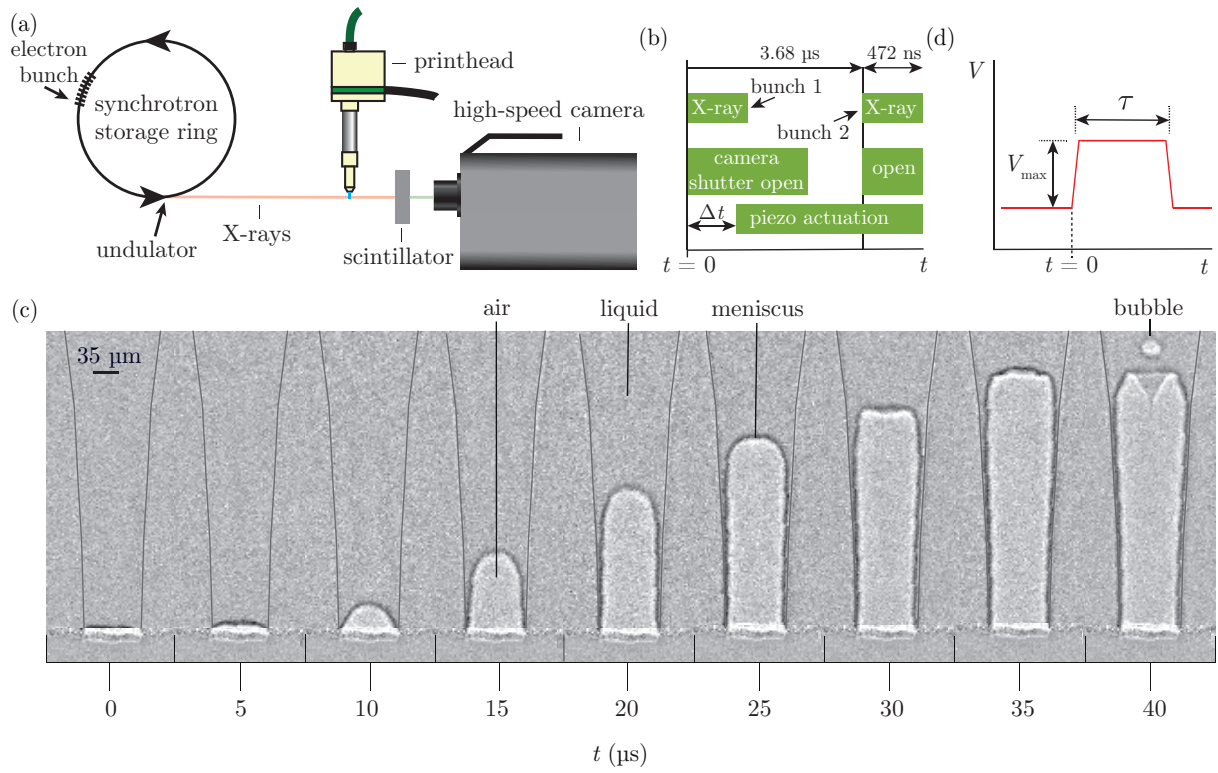


Figure 2.1: Schematic of the experimental setup. (b)  $t = 0$  is when the first 472 ns X-ray pulse illuminates the printhead and the camera is triggered. The piezo in the printhead is triggered after a set delay  $\Delta t$ , starting at 0  $\mu\text{s}$ . After 3.68  $\mu\text{s}$  the next X-ray pulse illuminates the set-up for the second frame in the recording. This process continues for 200 frames. The next recording has a delay  $\Delta t$  of 0.5  $\mu\text{s}$  for the piezo actuation. This continues in steps of 0.5  $\mu\text{s}$  until a maximum  $\Delta t$  of 3.5  $\mu\text{s}$ . (d) The trapezoidal piezo driving pulse. (c) Typical bubble entrainment phenomenon for a driving pulse with  $V_{\text{max}} = 140 \text{ V}$  and  $\tau = 32 \mu\text{s}$ . The edge of the nozzle is marked by the gray lines.

tors (Stanford DG535) that were triggered using the radio-frequency signal generated by the passing of the electron bunch. The time between two subsequent X-ray illumination pulses is set by the round-trip time of the electron bunch of 3.68  $\mu\text{s}$  in the storage ring. The interframe time of the high-speed camera was therefore also set to 3.68  $\mu\text{s}$  (271.553 frames/s) such that every camera frame was exposed by a single X-ray illumination pulse, see Fig. 2.1b. The X-rays were converted into visible wavelength photons using a scintillator plate (LuAG:Ce, decay time 50 ns), which were captured by the high-speed camera and a 10 $\times$  imaging objective (Mitutoyo Plan Apo Infinity Corrected Long WD, Edmund Optics) at a spatial resolution of 2  $\mu\text{m}/\text{pixel}$ . Figure 2.1c

shows the meniscus retracting into the nozzle. Around  $t = 30 \mu\text{s}$ , the concave meniscus deforms and an instability develops, which pinches off a bubble. Each experiment was repeated 9 times, where for every repeat the delay time ( $\Delta t$ ) was increased by  $0.5 \mu\text{s}$  for the start of the piezo driving pulse, as illustrated in Fig. 2.1b. The nine high-speed recordings were then interleaved to obtain a single high-speed recording at an effective frame rate of 2 million frames/s (500 ns interframe time).

The employed single-nozzle printhead (Autodrop Pipette, Ad-K-501 and AD-H-501, Microdrop Technologies GmbH) has a nozzle diameter of  $70 \mu\text{m}$  [60,61]. The printhead was driven by a rectangular pulse (Fig. 2.1c) with rise and fall times of  $0.2 \mu\text{s}$ . The piezo driving pulse was generated by an arbitrary waveform generator (Agilent 33220A) and amplified by a broadband amplifier (Falco System WMA-300). The pulse width  $\tau$  was varied between  $30 \mu\text{s}$  and  $36 \mu\text{s}$  and the driving amplitude  $V_{max}$  was varied between 70 V and 150 V. In all experiments, Milli-Q water was used as the model ink. An underpressure was applied by manually adjusting the piston of the syringe, which was connected to the liquid supply line of the printhead, to prevent the water from dripping outward under the influence of gravity.

### 2.2.2 Image processing

The grayscale images obtained from the experiments appear uniform in brightness, except at the interfaces (Fig. 2.1c). This is the result of the relatively high X-ray energy, which essentially overexposes the images. However, due to the coherence of the X-ray beam, the X-rays are refracted at the interfaces and form a pair of a dark and a bright fringe at the location of the interface as the waves propagate from the printhead to the camera [80]. The distance between the setup and the camera was optimized (approximately 0.4 m) to achieve the highest contrast of said interface-fringes, where the gas-liquid interface is located between the dark and the bright fringe [92,93]. In Fig. 2.1c, it is shown that the dark part of the fringe is located at the liquid side while the bright part is located at the air side.

The analysis of the images was performed in Matlab using the Canny edge detection method. An example of the image processing result on the frame shown in Fig. 2.2a is presented in Fig. 2.2b. To extract the volume of air in the nozzle from the images, we use the axis of symmetry of the nozzle being in the middle between the two nozzle side walls (black dash-dotted line) and

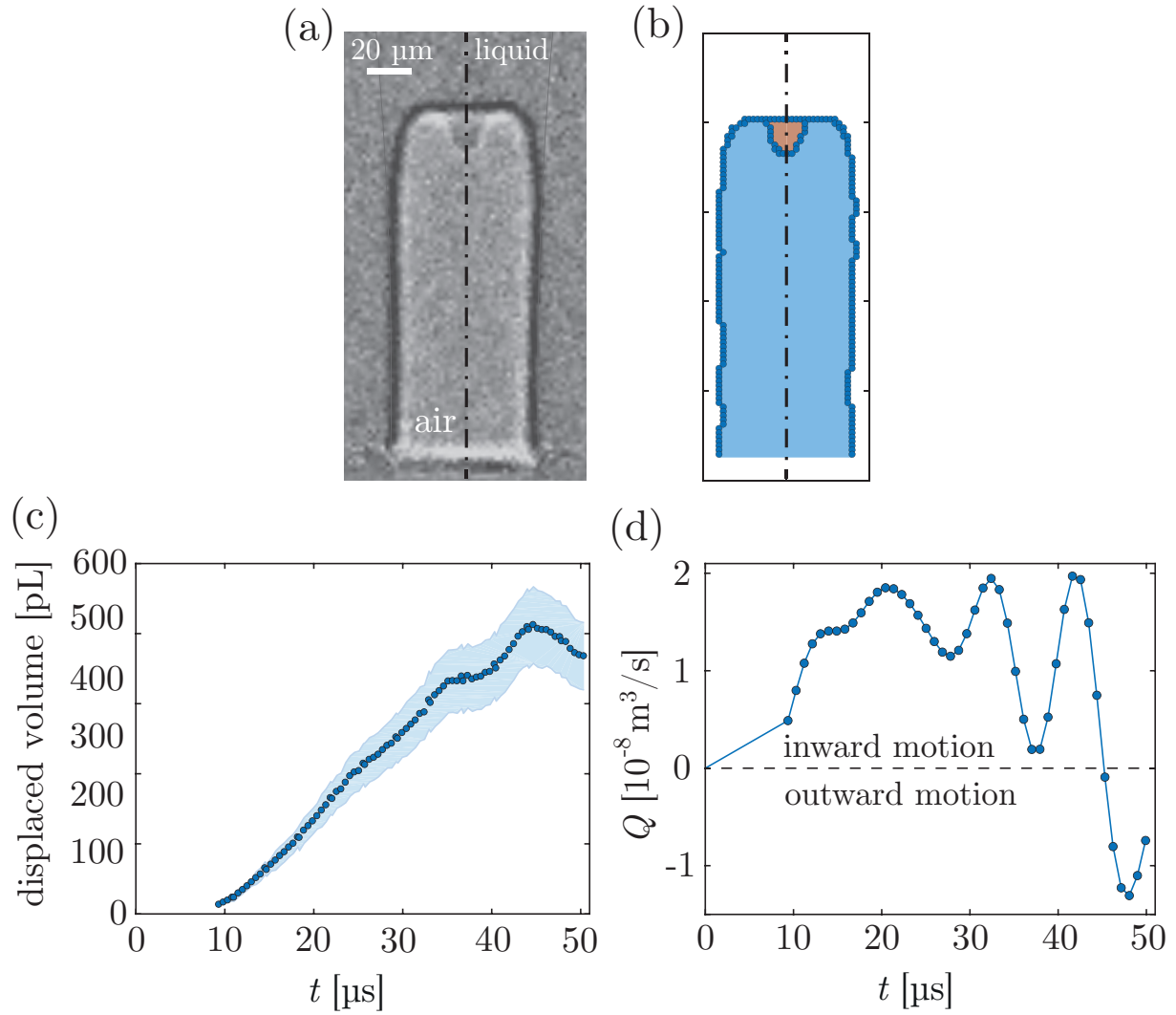


Figure 2.2: (a) Experimental snapshot where the black dash-dotted line is the axis of symmetry of the nozzle. (b) Edge detection result of the snapshot shown in (a). The total volume minus the volume in the orange area results in the volume of the blue region. (c) Extracted volume over time for  $V_{max} = 70$  V and  $\tau = 34$   $\mu\text{s}$ . (d) Flow rate ( $Q$ ) as determined from the volume curve in (b). The experimentally obtained  $Q(t)$  was input to the numerical simulations shown in Fig. 2.4.

then extract the distance of each edge point (the blue datapoints in Fig. 2.2b) to the axis of symmetry. Two consecutive radii were then used to calculate the volume of a truncated cone, by assuming cylindrical symmetry [94]. The total volume is the summation of all truncated cones along the center line, indicated by the blue region. When an outward-directed liquid jet was formed into the



air-filled cavity, as in Fig. 2.2a, the volume of the liquid jet was found in the same way (orange area) and then subtracted from the total volume to obtain the volume of air. The resulting displaced volume of air over time is shown in Fig. 2.2c. The meniscus position could not be analyzed for times before  $9\text{ }\mu\text{s}$  as it was optically overlapping with the glass-air interface. Therefore, the experimentally measured displaced volume was linearly interpolated between  $t = 0$  and  $t = 9\text{ }\mu\text{s}$ , from zero to the first measured displaced volume. The curve in Fig. 2.2c was smoothed and resampled (Matlab's smoothing spline with smoothing parameter of 0.7), and its derivative provides the volume flow rate  $Q$  (Fig. 2.2d), which was used as an input in the numerical simulations.

## 2.3 Numerical method

### 2.3.1 Governing equations

To gain insight into the mechanism of bubble entrainment, numerical simulations were performed with the free software program BASILISK [95], which solves partial differential equations on an adaptive Cartesian mesh (quad/octree discretization). The governing equations of our system are,

$$\nabla \cdot \mathbf{u} = 0, \quad (2.1)$$

$$\rho \left( \frac{\partial \mathbf{u}}{\partial t} + \mathbf{u} \cdot \nabla \mathbf{u} \right) = -\nabla p + \nabla \cdot \left[ \mu \left( \nabla \mathbf{u} + \nabla \mathbf{u}^T \right) \right] + \sigma \kappa \delta_S \mathbf{n}, \quad (2.2)$$

depicting the conservation of mass and momentum in an incompressible formulation, respectively. In the above equations,  $\mathbf{u}$  is the velocity vector field,  $p$  the pressure,  $\rho$  the density, and  $\mu$  the dynamic viscosity. The last term in Eq. (2.2) describes capillary forces, modelled as continuous surface forces (CSF) [96], where  $\sigma$  is the surface tension coefficient,  $\kappa$  is the curvature of the interface,  $\delta_S$  is a characteristic function defined as 1 at the interface and 0 elsewhere, and  $\mathbf{n}$  is the normal vector to the interface.

These equations were solved via a finite volume discretization. The numerical scheme is detailed in [97–99]. To account for multiple phases, a geometric Volume-of-Fluid (VoF) method was employed [100], in which the interface has a sharp representation. In our two-phase framework, a volume fraction  $c$  delimits both phases. It is equal to 1 in water, to 0 in air, and to values in between in cells containing an interfacial segment. The volume fraction is



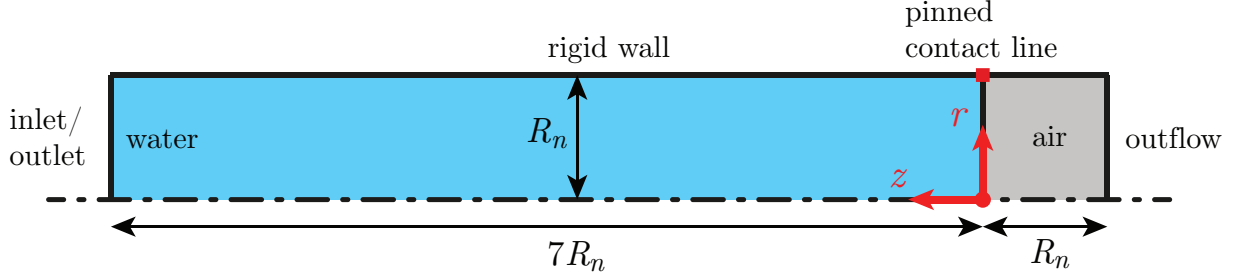


Figure 2.3: Schematic of the axisymmetric numerical domain (to scale), with the boundary conditions specified. The bottom boundary is the axis of symmetry, depicted by the dot-dashed line.

advected with the local velocity field, thus obeying the following equation,

$$\frac{\partial c}{\partial t} + \mathbf{u} \cdot \nabla c = 0. \quad (2.3)$$

The flow was modeled in a one-fluid formulation, with one continuous velocity field. Jumps of the local fluid properties, such as density and viscosity, were allowed across the interface, where they were defined as arithmetic averages, weighted by the volume fraction:  $\{\rho, \mu\} = c\{\rho_1, \mu_1\} + (1 - c)\{\rho_2, \mu_2\}$ , where 1 and 2 are subscripts denoting water and air, respectively. In the presence of capillary forces, jumps in pressure across the interface are also taken into account.

### 2.3.2 Numerical setup

Figure 2.3 depicts the numerical domain in the initial quiescent configuration. The experimental nozzle is tapered, with its local radius being a function of the axial coordinate  $z$ . However, in our numerics, this tapering is neglected. Therefore, the nozzle is modeled in axisymmetric cylindrical coordinates with constant radius  $R_n = 35 \mu\text{m}$ , corresponding to the radius of the nozzle exit. We compare our numerical results with experiments performed at a low driving voltage, where the liquid does not retract much into the nozzle, and where the effect of the tapering of the experimental nozzle is thus expected to be limited. The numerical domain is rectangular, with dimensions  $[8 : 1] R_n$ . The origin is set at the nozzle exit, indicated by the polar coordinates' unit vectors in Fig. 2.3. Liquid water initially occupies the region of the domain where  $z \geq 0$ .

Air occupies the remaining region where  $z < 0$ .

The bottom boundary is the axis of symmetry, depicted by the dot-dashed line. The top boundary has the conditions of a rigid wall, i.e.  $\mathbf{u} = \mathbf{0}$ ,  $\partial p / \partial r = 0$ . Generally, the VoF method allows accurate control over the contact line behavior via the setting of well defined boundary conditions on the volume fraction  $c$  [101]. For example, one can fix a specific contact angle throughout the simulation or pin the contact line at specific locations. In the present work, we pin the contact line at the nozzle exit, analogously to experimental observations (Fig. 4.1d), by setting a condition on the volume fraction,

$$c(r = R_n) = \begin{cases} 1, & \text{if } z \geq 0, \\ 0, & \text{otherwise.} \end{cases} \quad (2.4)$$

The right boundary has outflow conditions, where the pressure is set to a gauge constant  $p = 0$ , and  $\partial \mathbf{u} / \partial z = \mathbf{0}$ . Finally, the flow is driven at the left boundary, having the conditions of an inlet/outlet. Although the flow is continuously transient, and not fully developed, a Poiseuille velocity profile is prescribed at the left boundary for it to respect the no-slip boundary condition at the rigid wall,

$$u_z(r, t) = -\frac{2Q(t)}{\pi R_n^2} \left[ 1 - \left( \frac{r}{R_n} \right)^2 \right], \quad (2.5)$$

where  $u_z$  is the axial component of the velocity. This parabolic profile is defined as  $\int u_z(r, t) dA = -Q(t)$ , where  $Q(t)$  is the instantaneous flow rate through the nozzle, as measured from the experiment (Fig. 2.2c). The pressure is set to a zero Neumann boundary condition in the normal direction, i.e.  $\partial p / \partial z = 0$ . The input flow rate  $Q(t)$  and the boundary conditions are not changed when varying the viscosity of the liquid.

Adaptive mesh refinement was employed in the numerical simulations, based on the error of the volume fraction  $c$  and the velocity field  $\mathbf{u}$ . Therefore, the grid was refined at the interface and in the regions of interest. The smallest grid size attained in the simulations was  $\Delta = R_n/128$ , which was found sufficient for our current purposes.

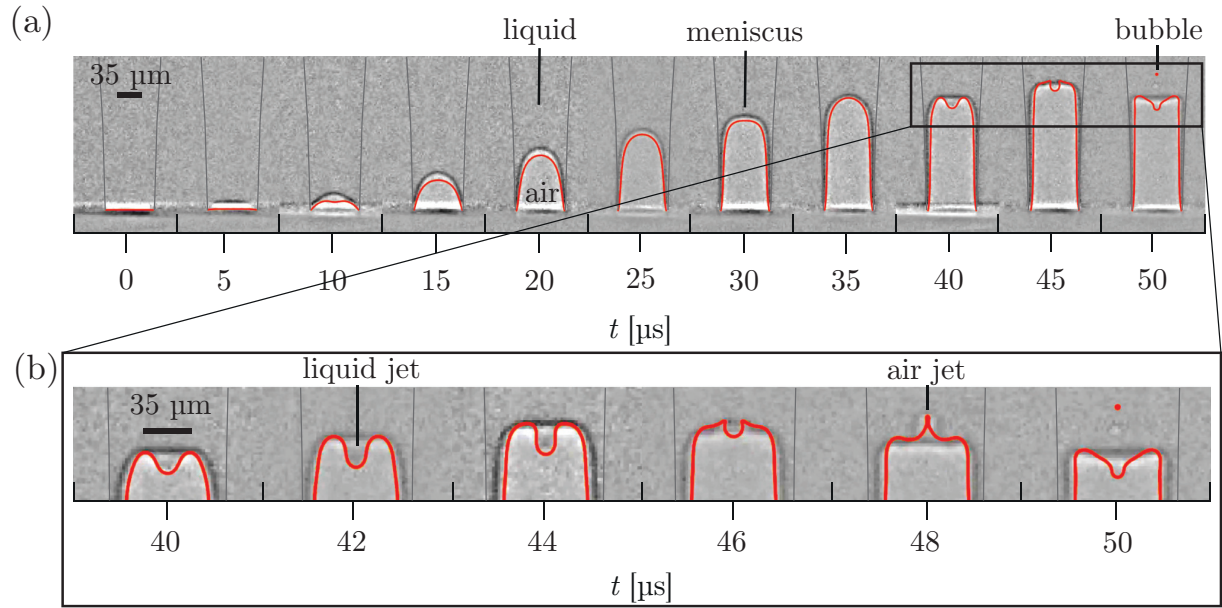


Figure 2.4: (a) Meniscus position during different time instants of the bubble entrainment phenomenon as observed in the experiment (grayscale images) and the numerical simulations (red curves) for  $V_{max} = 70$  V and  $\tau = 34$   $\mu\text{s}$ . (b) A zoomed-in image of the same bubble entrainment phenomenon. The outline of the nozzle is highlighted with gray lines.

## 2.4 Results & discussion

### 2.4.1 Phenomenology and numerical validation

Figure 2.4a shows a typical example of a bubble entrainment process inside the nozzle of the piezoacoustic printhead as observed using X-ray imaging. The corresponding numerical simulations are depicted by the solid red curves. Good agreement is observed between the experimental and numerical results, with only slight discrepancies due to the missing tapering in the numerical simulations. The motion of the meniscus near the moment of bubble pinch-off is shown in more detail in Fig. 2.4b. The bubble entrainment process can be described as follows: First, the meniscus retracts inward (10–35  $\mu\text{s}$ ), thereby becoming concave in shape after which it is accelerated outwards (40  $\mu\text{s}$ ), producing a liquid jet in the center (Fig. 2.4b). Subsequently, another outward acceleration moves the outer region of the meniscus outward (46–48  $\mu\text{s}$ ) whereas the center of the meniscus stays behind, causing the central jet to recoil, thereby forming an inward air jet in the center (48  $\mu\text{s}$ , (Fig. 2.4b)). When this air jet pinches off, a bubble is entrained (50  $\mu\text{s}$ ), similar to the bubble

entrainment process described before in [76].

### 2.4.2 Bubble pinch-off classes

In the search for different bubble pinch-off regimes, several parameter scans were performed. Note that the aim of this section is to provide a phenomenological, rather than a one-to-one quantitative comparison between the experiments and the numerics. Experimentally, the driving amplitude  $V_{max}$  and pulse width  $\tau$  were varied while the liquid properties were kept constant. For high driving amplitudes, the meniscus retracts further into the nozzle whose tapering starts to have a significant effect on the dynamics, leading to large discrepancies between the experiments and the numerics. Therefore, to numerically capture the different classes of bubble entrainment that were experimentally observed, inertia's effect on the meniscus oscillations is replicated by changing the liquid viscosity, while the flow rate boundary condition was kept constant (constant low amplitude driving). The different bubble entrainment classes are depicted in Fig. 2.5.

We start with the reference case, depicted in Figs. 2.5b and e, and shows the pinch-off of a spherical bubble from the central air jet. No bubble is entrained when the pulse width is decreased in the experiment (Fig. 2.5a), or when the viscosity is increased in the numerics (Fig. 2.5d). On the other hand, when in the experiment the driving amplitude is increased, or when the viscosity is decreased in the numerics, two bubbles are entrained as shown in Figs. 2.5c and 2.5f, respectively. The first bubble appears when the central liquid jet is present. At this moment, the rim at the base of the liquid jet pinches off to form a bubble resulting in a toroidal bubble that quickly becomes spherical due to surface tension, to minimize its surface energy, as also illustrated in the inset of Fig. 2.5f. Toroidal bubble pinch-off was also mentioned in ref. [76]. The second entrained bubble again pinches-off spherically from a central jet, similar to the scenario shown in Figs. 2.5b and e. It is evident from Fig. 2.5 that even though the parameters varied in the experiments (voltage and pulse width) and the numerics (liquid viscosity) are different, the simulations can still capture the meniscus motion and the bubble entrainment (both from the central jet and from the rim of the liquid jet) with a high degree of accuracy.

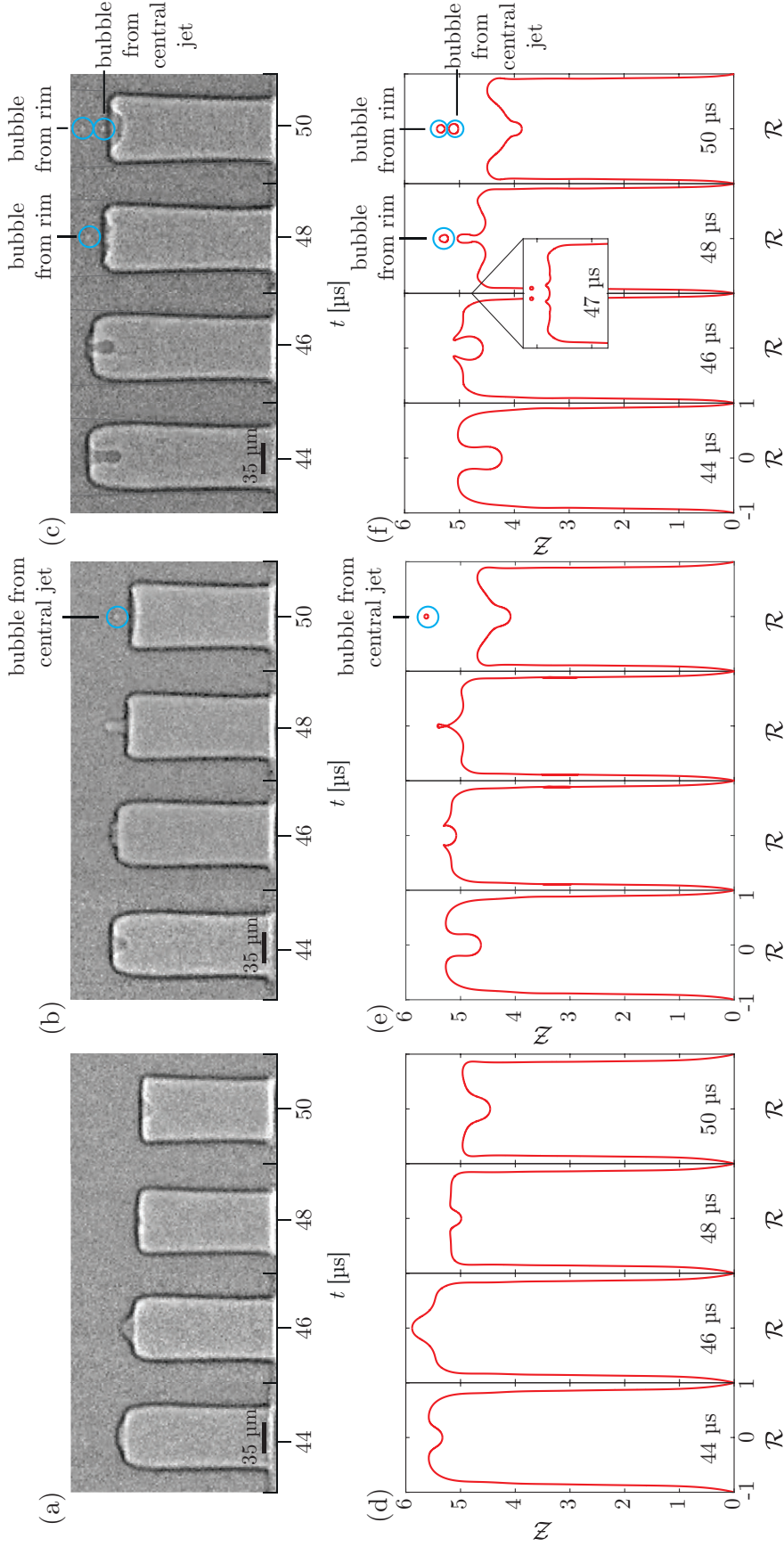


Figure 2.5: (a) No bubble entrainment in the experiment with  $V_{max} = 70$  V and  $\tau = 32$  μs. (c) One bubble is entrained in the experiment at  $V_{max} = 70$  V and  $\tau = 34$  μs, which is the same experiment as in Fig. 2.4. (c) Two bubbles are entrained in the experiment at  $V_{max} = 80$  V and  $\tau = 34$  μs. (d) No bubble entrainment in the numerics with a viscosity of  $1 \text{ mPa} \cdot \text{s}$ , which is the same simulation as in Fig. 2.4. (e) One bubble is entrained in the numerics with a viscosity of  $1 \text{ mPa} \cdot \text{s}$ , which is the same simulation as in Fig. 2.4. (f) Two bubbles are entrained in the numerics with a viscosity of  $0.5 \text{ mPa} \cdot \text{s}$ . In all the numerical results, the nozzle dimensions are non-dimensionalized by the nozzle radius  $R_n = 35$  μm.

### 2.4.3 Physical mechanism of pinch-off

In this section, we identify the mechanism of bubble entrainment using the information provided by the numerical simulations. The traditional picture of the process leading to bubble pinch-off is one driven by surface tension, and the focusing of capillary waves at the axis of symmetry, inducing jetting. Typical examples include bubble bursting at the interface [58,102], drop impact on a pool [54,59], and sequentially bubble (droplet) pinch-off by a Rayleigh-Plateau instability. This picture is supported by the absence of bubble entrainment in Fig. 2.5a, where the liquid is more viscous, as viscosity is known to dampen capillary waves [103]. However, hypothetical simulations with (an unphysical) zero surface tension showed that the process leading to bubble pinch-off is *not* driven by surface tension. Similar meniscus oscillations were observed and, although unphysical, pinch-off eventually happens when the protruding meniscus was thinner than the grid size. Thus, for this system, capillary waves do not govern the meniscus deformations leading to pinch-off.

To further unravel the mechanism of bubble entrainment, we plot the velocity vector field in Fig. 2.6. Fig. 2.6 shows that the flow-focusing mechanism deforms the meniscus, as detailed before in ref. [76]. In addition, we now observe well-defined vortical rings that are associated with the flow-focusing at the curved interfaces. These vortical rings alternate in direction. For a deeper understanding of the origin of these vortical rings, we examine the vorticity equation:

$$\frac{\partial \boldsymbol{\omega}}{\partial t} + (\mathbf{u} \cdot \nabla) \boldsymbol{\omega} = (\boldsymbol{\omega} \cdot \nabla) \mathbf{u} + \frac{1}{\rho^2} \nabla \rho \times \nabla p + \nabla \times \left( \frac{\nabla \cdot \mathcal{D}}{\rho} \right), \quad (2.6)$$

where  $\boldsymbol{\omega} = \nabla \times \mathbf{u}$  is the vorticity and  $\mathcal{D}$  is the viscous stress tensor. The assumption leading to Eq. (2.6) is an incompressible flow with conservative body forces. The second term on the right hand side of Eq. (2.6) is the baroclinic torque, describing the generation of vorticity due to the misalignment of density and pressure gradients. This torque is ubiquitous in geophysical flows [104], but also present in flows with much smaller length scales [105–107]. This term is particularly relevant in our study since it is responsible for the generation of vorticity at the interface, thus leading to flow-focusing, and eventually to bubble pinch-off. In Fig. 2.7, this mechanism is illustrated by showing four time instants of the numerical simulation. For each time-point, three panels are shown with, from left to right, (i) the dimensionless pressure



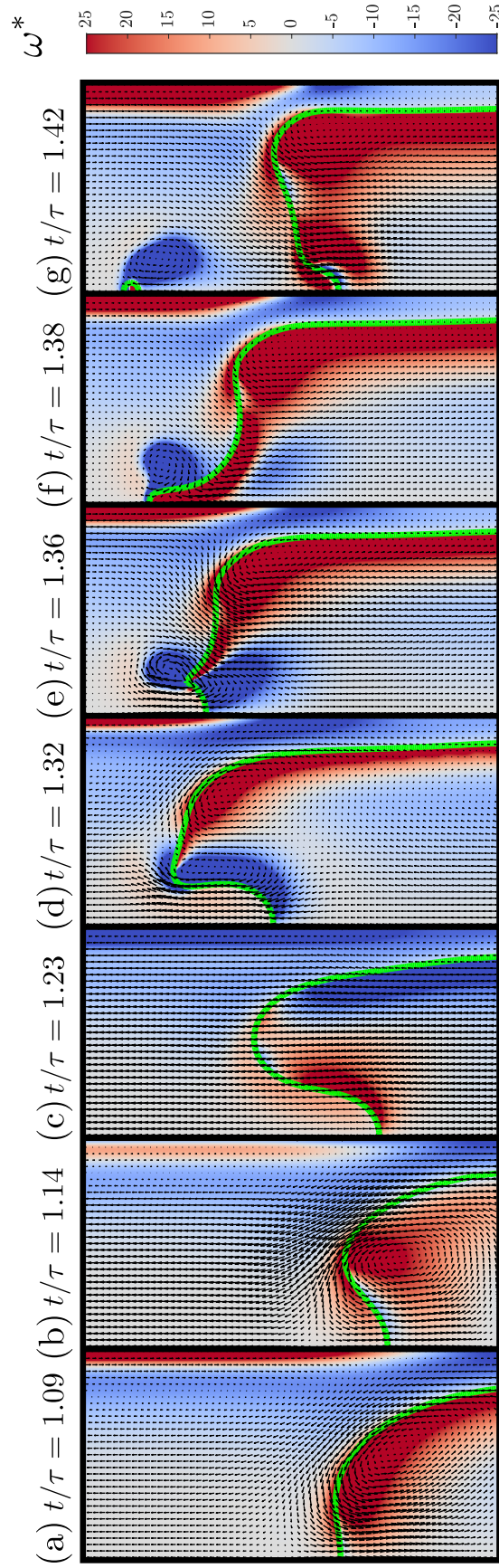


Figure 2.6: Snapshots from numerical simulations of the meniscus oscillations leading to bubble entrainment. The velocity is depicted as a vector field, and the dimensionless vorticity  $\omega^* = \omega\tau$  is illustrated in the background as a color code. In each snapshot, the interface is drawn in green. This is the  $V_{max} = 70\text{ V}$  and  $\tau = 34\text{ }\mu\text{s}$  case, where the fluid properties are as those in the experiment.

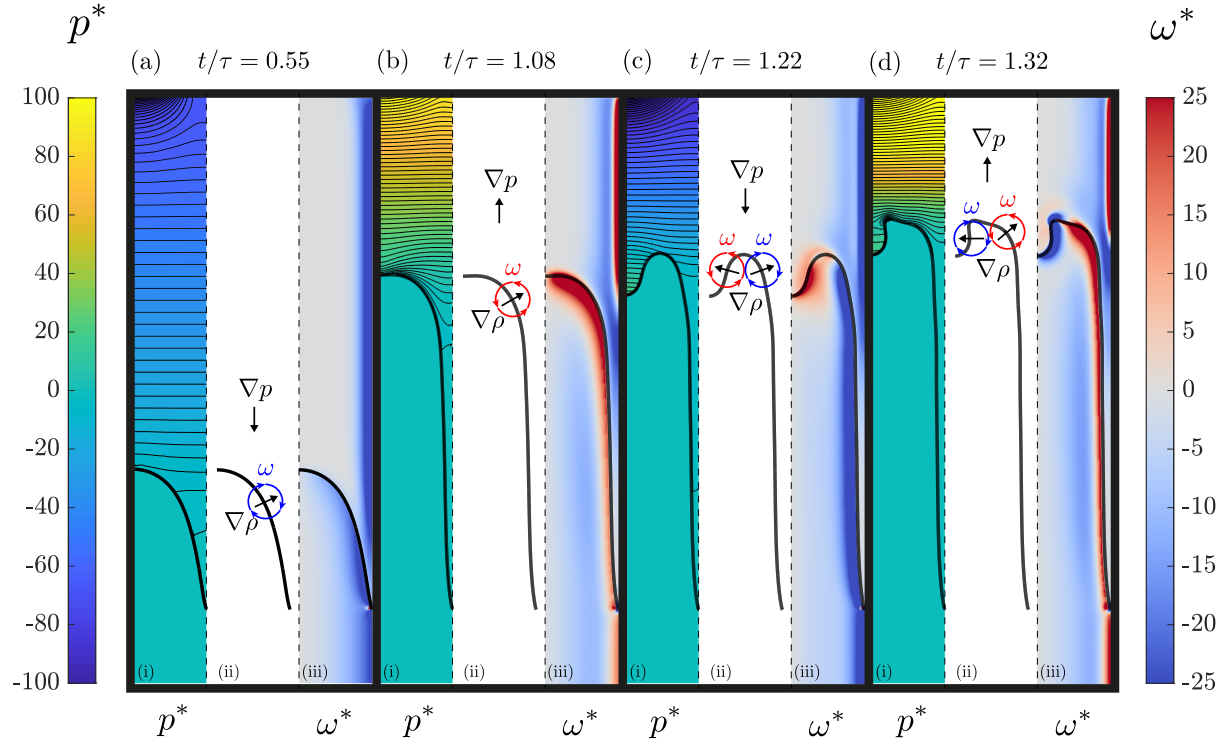


Figure 2.7: Illustration of the mechanism of meniscus oscillation and bubble entrainment. Four time instants are shown,  $t/\tau \in \{0.55, 1.08, 1.22, 1.32\}$ . Each time point contains three panels, showing, from left to right, the dimensionless pressure  $p^* = p\tau / (\rho_l R_n^2)$  with isocontours, an explanatory schematic of the baroclinic torque generated at the interface, and the dimensionless vorticity  $\omega^* = \omega\tau$ .

field with isocontours, (ii) an explanatory schematic, as well as (iii) the dimensionless vorticity. At  $t/\tau = 0.55$ , the meniscus is retracting inside the nozzle due to a pressure drop near the piezo (top boundary of the domain). The pressure field (i) reflects this behavior and clearly shows the direction of the pressure gradient. In the schematic (ii), the gradient of density is also shown across the interface (arrow inside circle), pointing to the heavier fluid. The baroclinic torque, generated at the interface, is therefore clockwise (blue circular arrow). It must be noted that this vorticity is proportional to  $\rho^{-2}$ . Therefore, it is much more pronounced in air than in water, as seen in the corresponding vorticity field (iii). At  $t/\tau = 1.08$ , the meniscus is being pushed outwards. The gradient of pressure thus changes sign, and the generated vorticity at the interface becomes counter-clockwise (red circular arrow). This induces flow-focusing at  $r = 0$ , the central axis, (Fig. 2.6a-b), thus contributing to the deformation of the meniscus, into the shape shown at  $t/\tau = 1.22$ .



Then, the meniscus is being retracted. With the current topology, the gradient of density has two different directions, and thus two oppositely rotating vortical rings, focusing the flow as shown in Fig. 2.6c. At  $t/\tau = 1.32$ , the meniscus is being pushed again, and so the vortical rings' rotation alternates, focusing the flow at the interface as shown in Fig. 2.6d. Although the pressure isobars are closely packed at the point of highest curvature in Fig. 2.7d(i), giving rise to a higher pressure gradient; the flow focusing does not happen there. This observation presents further argument in favor of the vorticity as the flow-focusing mechanism in the present work. A clockwise vortical ring persists at the tip of the protruding meniscus (Fig. 2.6f), thus contributing to bubble pinch-off, which is determined at the latest stage by capillary forces in a Rayleigh-Plateau like mechanism.

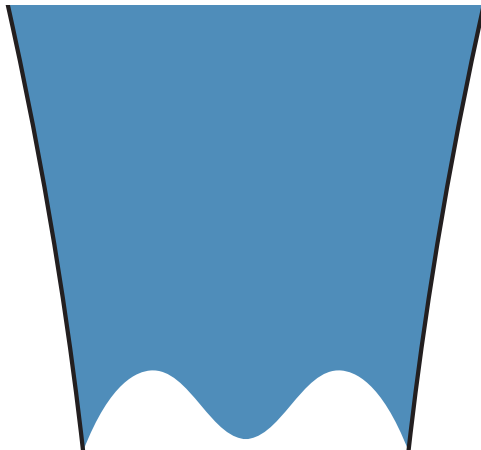
The last term in Eq. (2.6), which can be written as  $\nu \nabla^2 \omega$ ,  $\nu$  being the kinematic viscosity, is a diffusion term. Therefore, as the viscosity of the liquid increases, the vorticity generated at the interface gets diffused further into the bulk of the fluid. Hence, its flow focusing effect decreases, which can support the observation of no bubble pinch-off in Fig. 2.5d.

Since boundary integral simulations assume an irrotational flow, vortices are usually a missing ingredient. However, Fraters *et al.* (2021) [76] still obtained a proof of concept of the flow focusing mechanism leading to pinch-off by imposing an *ad-hoc* boundary condition on the velocity. Also, in their work, the contact line was not pinned and the interface was initialized with a certain curvature that was optimized to capture the experimental observations. We attribute the flow-focusing in their BI simulations to pressure impulses due to the abrupt changes in the imposed velocity field, similar as the interpretation by Peters *et al.* (2013) [52]. That process is therefore similar to the flow-focusing induced on the curved meniscus in the capillary tube impact experiments performed by Antkowiak *et al.* (2007) [51]. However, the current DNS clearly show that the flow-focusing, leading to bubble pinch-off from an inkjet meniscus, is vorticity-induced rather than being the result of pressure impulses that induce flow-focusing on the curved interfaces.

## 2.5 Conclusion

The oscillating flows in an inkjet printhead can lead to geometric flow-focusing through which an inward gas jet can form on the retracted concave meniscus. The gas jet can pinch-off to entrain an air bubble. The study of the bubble pinch-off phenomena using ultrafast X-ray phase-contrast imaging provided a complete visualization of the oscillating meniscus, which was input to direct numerical simulations. The numerical simulations demonstrated that the presence of vortical rings leads to geometric flow-focusing, which in turn can result in bubble pinch-off. The vortical rings in this system are a manifestation of the baroclinic torque at the interface. The viscosity of the liquid influences the diffusion of vorticity from the interface into the bulk; therefore, increasing the viscosity will also reduce the probability of bubble entrainment. These results provide a fundamental understanding of the oscillating meniscus and the resulting flows inside an inkjet printhead that allow for a more complete understanding the bubble entrainment process in an inkjet nozzle.

## Predicting the meniscus shape modes of an inkjet nozzle interface



□

---

In preparation as: Martin van den Broek, **Maaïke Rump**, Edgar Ortega Roano, Roger Jeurissen, Hans Reinten, Devaraj van der Meer, Detlef Lohse, Michel Versluis, Guillaume Lajoinie, and Tim Segers, *Meniscus mode shapes in inkjet printing*, where Maaïke extended the manuscript written by Martin with Edgar's BI results and the analysis of the non-axisymmetric modes using Guillaume's code.

## Abstract

Liquid-air meniscus shape oscillations have a large influence on the printing process in drop-on-demand inkjet printing. However, a theoretical and experimental understanding of such oscillations is still limited, owing to the small length scales and short time scales involved. In this work we obtain experimental time-resolved 3D topography profiles of an oscillating meniscus driven at frequencies from 1 kHz to 400 kHz with an accuracy of length scales down to tens of nanometers and microsecond timescales. Furthermore, we obtain the resonance curve for multiple modes of the system and compare the measured resonance frequencies with those obtained from the capillary dispersion equation and from boundary integral simulations.

### 3.1 Introduction

Inkjet printing is a versatile industrial application of microfluidics as it allows for highly controlled non-contact deposition of picoliter droplets [1,2,108]. It finds application beyond graphics printing, including the printing of electronics [33,38,109], pharmaceuticals [13], and biomaterials [11,12,39]. In piezo-actuated drop-on-demand inkjet printing, droplets are typically generated by driving the liquid-air meniscus at its fundamental first order mode resulting in droplet diameters typically of the order of the nozzle diameter [1]. However, smaller droplets can be formed by driving the meniscus into higher order shape oscillations [28]. This allows for a method of producing a range of droplet sizes without the need of different nozzle sizes. Higher order meniscus modes can originate from instabilities such as the Rayleigh-Taylor instability [48] or a parametric instability [110,111]. It can also originate from an asymmetry in the nozzle, e.g. due to nonuniform wetting of the nozzle perimeter or due to the presence of a dirt particle or crevice. On the other hand, since the liquid-air meniscus acts as an elastic membrane, it can also be excited, in a more controlled way, into higher order shape modes, e.g. by increasing the excitation frequency. The eigenfrequencies of the admissible modes of an undriven liquid-air meniscus are well described by the capillary dispersion relation and Bessel functions [112-115], which relate the angular frequency  $\omega$  to the wavenumber  $k$  in terms of the liquid surface tension  $\gamma$  and liquid density  $\rho$ . However, an inkjet printhead is an acoustic resonator with a driving frequency-dependent volume flow rate. Thus, a coupling between the resonance frequencies and the driving volume flow rate is expected to change the resonance frequencies

compared to the undriven system. In the present work, we aim to understand the resonance frequencies of the driven liquid-air meniscus in a piezoacoustic drop-on-demand inkjet nozzle. To this end, we map the modal landscape of a non-jetting nozzle using digital holographic microscopy.

## 3.2 Experimental and numerical methods

### 3.2.1 Capillary dispersion relation

The relation between wavelength and frequency on a surface dominated by surface tension is described by the capillary dispersion relation. For an air-water surface, this becomes:

$$\omega^2 = \frac{\gamma}{\rho} |k|^3, \quad (3.1)$$

where  $\omega$  is the angular frequency,  $\gamma$  is the surface tension,  $\rho$  is the density of water, and  $k$  is the wavenumber that relates to the wavelength  $\lambda$  via  $\lambda = 2\pi/k$ . When the surface is restricted, like the pinning of the meniscus at the nozzle exit, the oscillating surface has modes. The modes depend on the shape and size of the nozzle. The mode shape  $S$  in a cylindrical geometry has a radial part described by the  $s$ 'th order Bessel function, and an azimuthal part described by the cosine function:

$$S(r, \theta) \sim J_s(kr) \cos(s\theta) \quad \text{with} \quad s = 0, 1, \dots \quad (3.2)$$

The azimuthal mode number is indicated by  $s$ , while the radial modes are determined from the roots of the Bessel function. Each order Bessel function has an infinite number of positive roots  $\alpha_{s,m}$ . Thus  $\alpha_{s,m}$  is the  $m$ 'th positive root of the  $s$ 'th order Bessel function, which provides the wavenumber of each mode as  $k_{s,m} = \alpha_{s,m}/R$  with  $R$  the radius of the nozzle exit. Combining Eqs. (3.1) and (3.2) gives the eigenfrequencies of the modes of an undriven cylindrical oscillating pinned meniscus.

### 3.2.2 Set-up

A single nozzle printhead (AD-K Microdrop pipette) filled with highly purified water (milliQ) was used. Here, the printhead consists of a cylindrical piezoelectric transducer bonded around a glass capillary tube with a tapered end radius of 35  $\mu\text{m}$ . The printhead was connected to a syringe pump in order

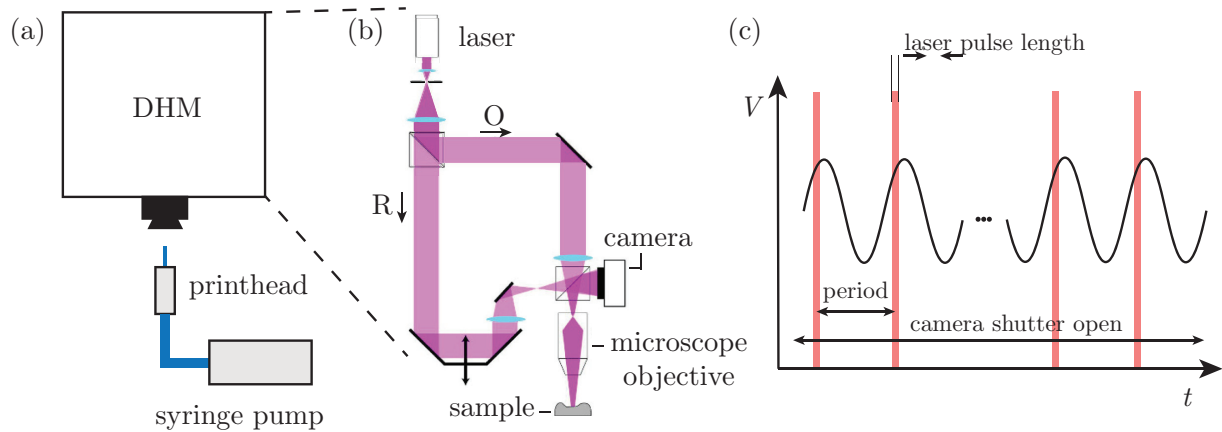


Figure 3.1: (a) A schematic overview of the set-up used in the experiments. (b) Details of the beam paths inside the DHM, with the object beam indicated with O and the reference beam with R. (c) Working principle of the DHM to obtain sufficient illumination for a single frame.

to provide a flat meniscus at the nozzle exit, see Fig. 3.1a. The height profile of the meniscus was determined using digital holographic microscopy, a non-contact optical method to quantify the 3D topography from a single hologram at sub-micron height resolution [116]. In order to create a hologram, a beam splitter in the DHM (Lyncee Tec R1000) divides a 666 nm wavelength laser into a reference laser beam and an object laser beam, indicated in Fig. 3.1b. The object beam passes through a 63 $\times$  microscope objective (Zeis) onto the sample, and is reflected back into the DHM, where it interferes with the reference beam. The small difference in optical path length creates information on the phase change, in addition to the change in intensity. The use of the reflected object beam limits the spatial gradient of the studied object, which must not exceed a 22 $^\circ$  angle with this objective, as the laser beam will otherwise not be reflected back into the DHM. Both the intensity and phase information are contained within the hologram, which is captured by a CCD camera (Mikrotron EoSens 4CxP).

### 3.2.3 Procedure

In order to obtain the meniscus oscillations shape at different phase-angles when driven at 100 kHz and higher frequencies, measurements were performed stroboscopically. To acquire an image of a fast moving surface without motion blur, the surface should have minimal motion during the illumination.

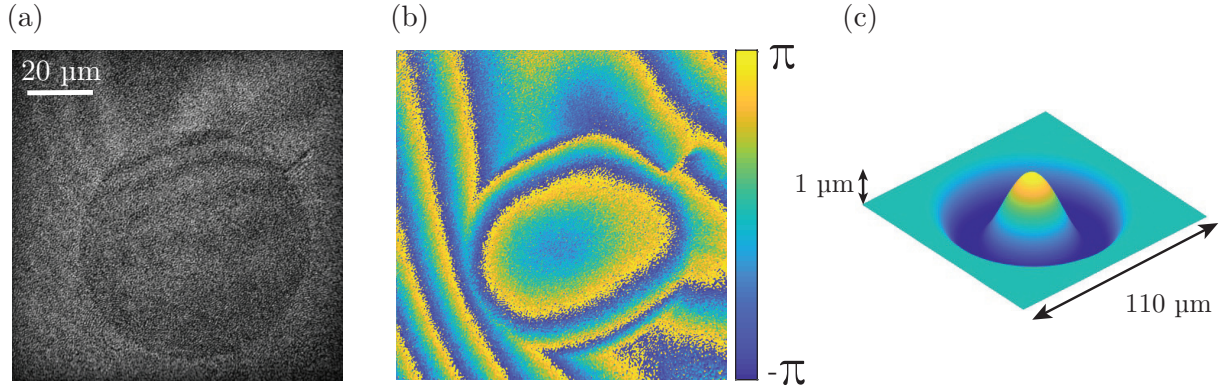


Figure 3.2: (a) Intensity snapshot of the nozzle exit. (b) The same snapshot now showing the unwrapped phase information. (c) A 3D presentation of the height profile after unwrapping the hologram. The color indicates the height, with blue to yellow indicating low to high.

Therefore, the laser pulse length is on the order of 10 ns (Lyncee Tec). However, such a single laser pulse provides insufficient illumination intensity to produce a measurable hologram. Therefore, during the sinusoidal actuation of the inkjet piezo actuator, the camera shutter opens and the laser pulses multiple times at the same phase delay within the oscillation cycle until the same illumination intensity is acquired as in the static illumination mode (calculated by the DHM software), see Fig. 3.1c. This process was repeated for 10 different phases in the oscillation period, resulting in a total of 20 frames, covering two oscillation cycles at one driving frequency. The collected intensity and phase information of the hologram are further processed for analysis.

The full modal landscape was characterized for driving frequencies from 1 kHz to 400 kHz with steps of 1 kHz, where the driving amplitudes range from 0.7 to 77 V. The driving amplitude was limited to prevent droplet formation as well as by the maximum slope of  $22^\circ$  set by the technique of reflection based DHM. The meniscus oscillation amplitude decreases with increasing driving frequency. Therefore, the driving voltage was increased for frequencies above 130 kHz to be able to visualize the motion of the meniscus.

### 3.2.4 Data analysis

Figure 3.2a and b are the intensity and phase information, respectively, that are contained within a single holographic snapshot. The intensity image is the

typical image obtained from bright field microscopy. The phase image displays the phase difference between the objective and reference beam. The phase difference is a measure of height given by the fraction of the wavelength of the laser (666 nm). Therefore, the height profile can be extracted by unwrapping this phase image, which means adding or subtracting the appropriate number of multiples of  $2\pi$  to obtain the total phase difference, and thereby the total height with respect to the nozzle exit [117]. The resulting unwrapped image is shown in Fig. 3.1c.

To recover the surface modes from the experimental results, we first develop the surface into its Fourier series, bearing in mind that the surface is, at most,  $2\pi$  periodic:

$$S(r, \theta, t) = \sum_{s=0}^{\infty} S_s(r, t) \cos(s\theta + \phi_s), \quad (3.3)$$

where  $S_s$  is the Fourier coefficient of each surface mode  $s$  described as a function of the radius  $r$  and time  $t$ ,  $\theta$  is the angular coordinate and  $\phi_s$  is the phase of each surface mode. We then apply the Hankel transform to each independent (and orthogonal) component of the Fourier series:

$$S(r, \theta, t) = \sum_{s=0}^{\infty} \int_{r=0}^{\infty} \bar{S}(k, t) J_s(kr) k \, dk \cos(s\theta + \phi_s), \quad (3.4)$$

where  $\bar{S}(k, t)$  is the Hankel transform, and  $J_s(kr)$  is the Bessel function of the first kind corresponding to the surface mode  $s$ . Here we choose to express the Fourier series in the parameters of phase and amplitude since the phase represents the physical orientation of the mode in our experiment. Furthermore, we automatically have  $\phi_0 = 0$  for  $s = 0$  since its amplitude of the sin is always 0 in the Fourier series. Note that the choice of order  $s$  for the Hankel transform of the Fourier coefficients  $S_s(r)$  is no coincidence as the form given above is that obtained by solving the potential flow equation using variable separation. The inverse Hankel transform allows for computing the coefficients  $S_s(k, t)$ :

$$\bar{S}_s(k, t) = \int_{r=0}^{\infty} S_s(r, t) J_s(kr) r \, dr, \quad (3.5)$$

which uses the orthogonality of the Bessel functions. By orthogonality of the trigonometric functions:

$$S_0(r, t) = \frac{1}{2\pi} \int_{\theta=0}^{2\pi} S(r, \theta, t) d\theta, \quad (3.6)$$



and, for  $s > 0$ :

$$S_s(r, t) = \frac{1}{\pi} \int_{\theta=0}^{2\pi} S(r, \theta, t) \cos(s\theta + \phi_s) d\theta. \quad (3.7)$$

Using the inverse Bessel transform:

$$\bar{S}_0(k, t) = \frac{1}{2\pi} \int_{\theta=0}^{2\pi} \int_{r=0}^{\infty} S(r, \theta, t) J_0(kr) r \, dr d\theta \quad (3.8)$$

for  $s = 0$  and, for  $s > 0$ :

$$\bar{S}_s(k, t) = \frac{1}{\pi} \int_{\theta=0}^{2\pi} \int_{r=0}^{\infty} S(r, \theta, t) J_s(kr) r \, dr \cos(s\theta + \phi_s) d\theta. \quad (3.9)$$

We easily recognize the surface integral:

$$\bar{S}_0(k, t) = \frac{1}{2\pi} \oint_{\xi} S(r, \theta, t) J_0(kr) d\xi \quad (3.10)$$

for  $s = 0$  and, for  $s > 0$ :

$$\bar{S}_s(k, t) = \frac{1}{\pi} \oint_{\xi} S(r, \theta, t) J_s(kr) \cos(s\theta + \phi_s) d\xi. \quad (3.11)$$

Although this step may seem trivial, it has a direct and important consequence as we can now compute this surface integral directly in the cartesian grid where the image is naturally defined. This makes the projection both faster and more precise by avoiding a cartesian to polar coordinate transformation that over-emphasizes the small radii.

Since the interface is pinned at the radius of the nozzle ( $R$ ), the eigenmodes of the cavity obey the relation:

$$J_s(kR) = 0, \quad (3.12)$$

which holds true for  $k_m = \alpha_m/R$  where  $\alpha_m$  is the  $m^{th}$  root of the Bessel function  $J_s(x)$ . Note that the roots  $\alpha_m$  are different for each  $s$  number. In order to detect the presence of these specific eigenmodes as a function of the driving frequency, we reduce the projection relation to the discrete set of  $k$  values of interest:

$$\bar{S}_{0,m}(t) = \frac{1}{2\pi} \oint_{\xi} S(r, \theta, t) J_0(k_m r) d\xi \quad (3.13)$$

for  $s = 0$  and, for  $s > 0$ :

$$\bar{S}_{s,m}(t) = \frac{1}{\pi} \oint_{\xi} S(r, \theta, t) J_s(k_m r) \cos(s\theta + \phi_s) d\xi. \quad (3.14)$$

In order to determine the phase  $\phi_s$  for each  $s$ -number, we first compute the root mean square (rms) value map of the surface oscillations over time in its native cartesian coordinates:

$$S_{rms}(x, y) = \frac{1}{T} \sqrt{\int_{t=0}^T S(x, y, t)^2 dt}, \quad (3.15)$$

where  $T$  is the duration of the recording. This map is then transformed to polar coordinates and averaged in the radial direction:

$$S_{rms,mean}(\theta) = \frac{1}{R} \int_{r=0}^R S_{rms}(r, \theta) dr. \quad (3.16)$$

This vector is then filtered in the Fourier domain to remove the higher order components in  $\theta$  (we are typically interested in  $\theta \leq 5$ ). The phase  $\phi_s$  is finally extracted by maximizing the cross-correlation value between  $S_{rms,mean}(\theta)$  and  $\cos(s\theta + \phi_s)$  as a function of  $\phi_s$ . Knowing the phase for each  $s$ -number allows for computing the modal projection as described above. The resulting experimental modal coefficients for the modes  $m = 1$  to 5 at  $s = 0$  are displayed in Fig. 3.3

The amplitude of each mode is then computed using the fast Fourier transform algorithm (fft) in Matlab. In the following, we extract the response amplitude of each mode at the fundamental frequency since we focus on the linear response of the interface. The method can thus also be easily extended to nonlinear (i.e., harmonic) responses.

In the low oscillation amplitude regime, the obtained modal amplitude as a function of frequency then depends linearly on the pressure driving. This driving, however, is unknown. In order to cancel the effect of the unknown driving, each modal amplitude is normalized with respect to the sum of the modal amplitudes of modes  $m = 0$  to 5, which are the modes visible (above noise level) in the considered frequency range:

$$S_{norm,s,m}(f) = \frac{S_{s,m}(f)}{\sum_{m=0}^5 S_{s,m}(f)} \quad (3.17)$$

This normalization is thus operated independently for each  $s$  number and reveals the dominant mode.

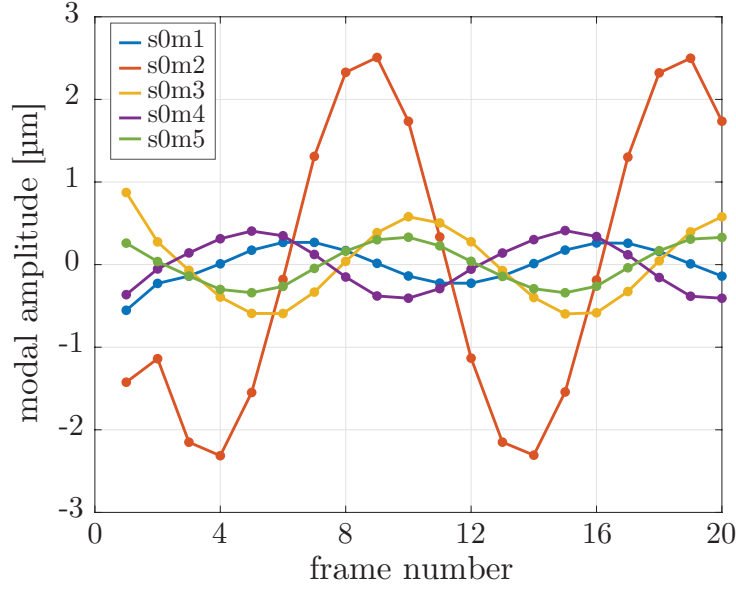


Figure 3.3: The modal coefficients of the first five axisymmetric modes from the experimental data, plotted versus the frame number. These datapoints were taken at a driving frequency of 70 kHz and a driving amplitude of 2 V. The solid lines are there to provide visual aid.

### 3.2.5 Boundary Integral simulations

Boundary integral (BI) simulations were performed to compare the experimental results to the resonance frequencies of a driven system, besides comparing them to the undriven system described by the capillary dispersion relation. The system was simulated as axisymmetric with irrotational, incompressible, and inviscid flow, where we neglect gravitational effects. The geometry and velocity input boundary condition are the same as in the work in Ch. 1 [76], except that the meniscus was fixed at all time on the contact line. Furthermore, the driving in this work is a sinusoidal function with an amplitude chosen such that the meniscus shape amplitude does not pinch-off a droplet. This amplitude was fixed for all driving frequencies. A snapshot of the meniscus shape at 95  $\mu\text{s}$  after initiating the driving with a frequency of 75 kHz is shown in Fig. 3.4a.

As we are studying a resonance phenomenon with an inviscid flow, the amplitude of the meniscus will keep on growing when the driving is at the resonance frequency. Therefore, the simulations were only run for the first 250  $\mu\text{s}$  after

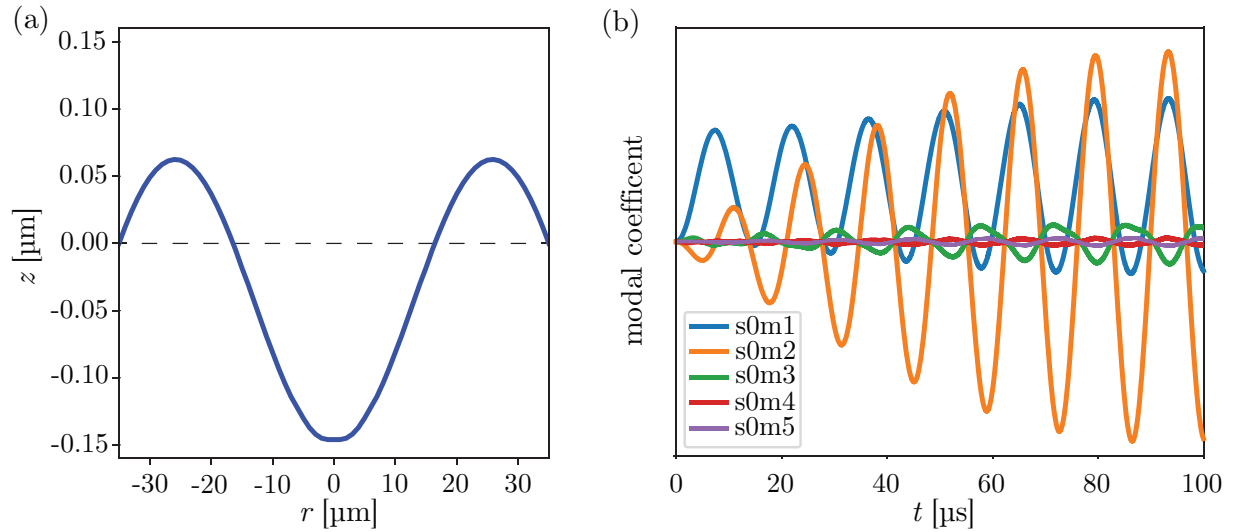


Figure 3.4: (a) The meniscus shape after driving the system for  $95 \mu\text{s}$  with a driving frequency of  $75 \text{ kHz}$ . (b) The modal coefficients of the first five axisymmetric modes from the numerical simulations during the first  $100 \mu\text{s}$  of driving the system at a frequency of  $75 \text{ kHz}$ .

initiating the driving frequency. The modal coefficients were calculated from the meniscus shape using the same method as that of the experimental results, described in section 3.2.4. Figure 3.4b shows the different modal coefficients over the first  $100 \mu\text{s}$  at a driving frequency of  $75 \text{ kHz}$ , showing a clear growth over time, and indicating that the driving frequency is close to resonance. The normalization of these results was done by first taking the absolute value of the curves shown in Fig. 3.4b, secondly, by taking the area underneath the curve for each mode, and finally normalizing this area by the summation of all areas. The normalization provides a quantitative description of the dominant mode, and this result can then be compared with the experimental data.

### 3.3 Results & discussion

First, we verified that the meniscus oscillations are driven in the linear regime and stationary. Parametric instabilities can occur at subharmonic frequencies [111]. In order to verify linear stability, the meniscus was driven at twice the imaging frequency, where no subharmonic oscillations were observed. Next, the full modal landscape is characterized, where a range of the axi- and non-axisymmetric meniscus oscillations were observed, see Fig. 3.5a and c, re-

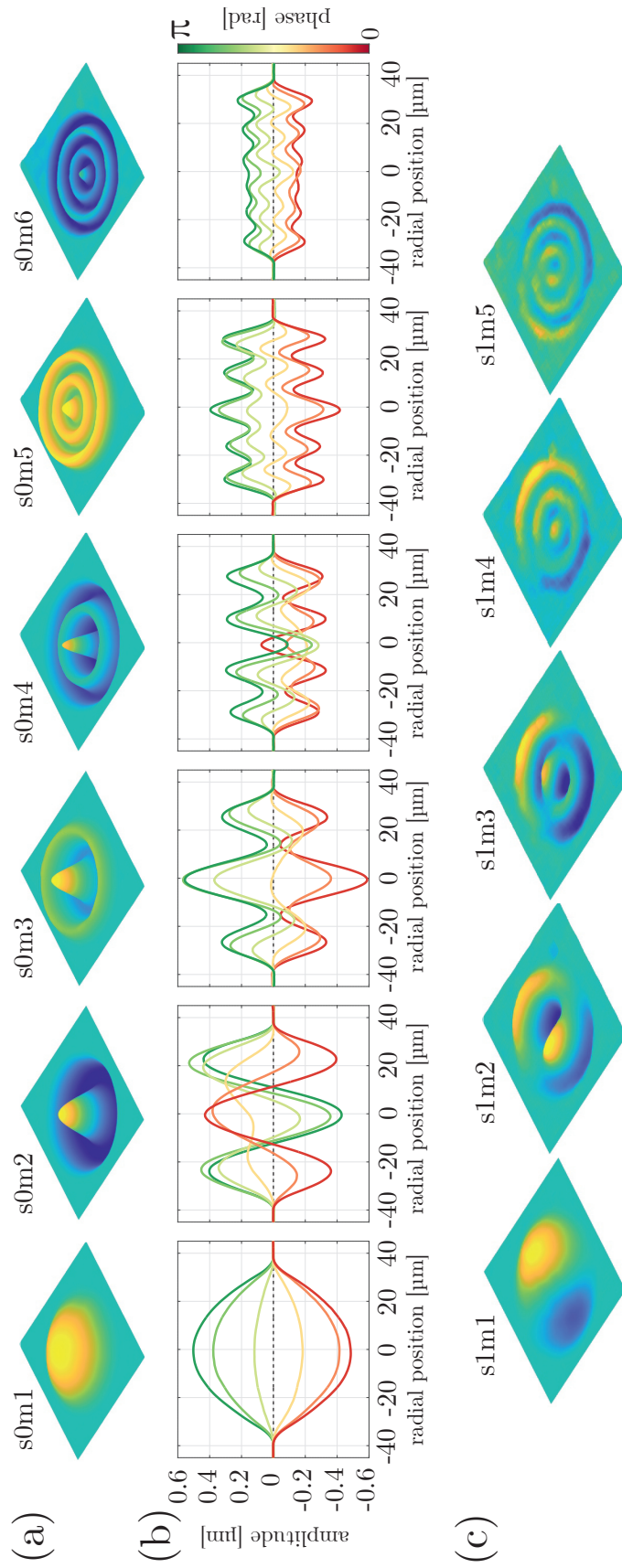


Figure 3.5: (a) Measured axisymmetric surface oscillation shapes obtained at different frequencies and a nozzle radius of 35  $\mu\text{m}$  and (b) the corresponding cross-sections. (c) Measured non-axisymmetric surface oscillation shapes using the same nozzle.

spectively. Note in Fig. 3.5b that the nodes of the oscillating meniscus are not located at a zero amplitude. Instead, the nodes oscillate around the meniscus exit at the same frequency as the driving frequency, confirming that the meniscus modes are driven by volume flow rate.

Figure 3.5a also shows that the fundamental first mode (parabolic mode shape) for low frequencies does not have nodes, and thus will always move with the driving frequency. The reason we observe this mode is because it is driven by the slosh mode, which occurs when the entire liquid column inside the printhead oscillates in-phase against the spring of the pinned meniscus [118][119]. The resonance frequency of the slosh mode depends on the liquid properties of the ink and the inner dimensions of the printhead. Thus, at low frequencies, the meniscus dynamics is not determined by the volume flow rate.

Furthermore, non-axisymmetric meniscus oscillations were also observed as shown in Fig. 3.5c. These oscillations have no net mass displacement. Therefore, they are not directly driven by the liquid bulk behind the meniscus. In theory, a perfectly pinned meniscus subjected to only perpendicular forces is limited to only axisymmetric modes. In reality, small asymmetric perturbations including angled fracture plane, nozzle damages, irregular pinning can all lead to non-axisymmetric modes.

The amplitude response of the meniscus varies greatly for each driving frequency due to an increase in flow rate at acoustic mode resonance. Figure 3.6a shows the amplitude of the center of the meniscus as a function of driving frequency, which is therefore a good representation of the acoustics of the printhead. In order to decouple the acoustics from the observed meniscus modes, the modal coefficients are normalized first by the driving voltage, and then by the sum of all determined modal coefficients (Eq. 3.17). The result for the s0m2 mode are shown in Fig. 3.6b as a function of driving frequency and for different driving amplitudes. The result shows that the normalized coefficient is independent of the driving voltage, meaning that the system is driven in the low-energy or linear regime. Note the sharp dips in the curve, this occurs at the frequencies where non-axisymmetric modes are observed. Furthermore, these results demonstrate that the modal landscape is independent of the printhead acoustics.

The resonance curves of the first five axisymmetric meniscus modes (s0m1-

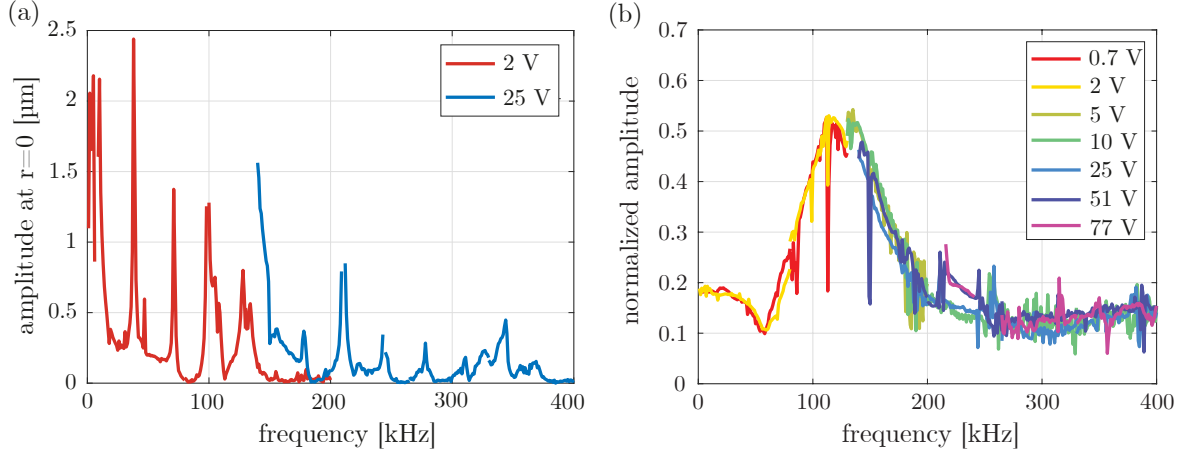


Figure 3.6: (a) The amplitude of the meniscus oscillation, measured at the center of the nozzle, versus the driving frequency. (b) The normalized amplitude for the s0m2 mode for different driving voltages.

s0m5) are shown in Fig. 3.7a. These curves were obtained similar to Fig. 3.6b, followed by taking the average over all the different driving amplitudes and using a moving average smoothing function. The fundamental mode (s0m1) is also included, even though the driving is different from the other modes, to present the complete system. The thin lines are the results of the BI simulations, which are discussed later. The same procedure is applied to the non-axisymmetric modes s1 to s3 in Figs. 3.7b-d, respectively. Non-axisymmetric modes higher than s3 had a too low signal to noise ratio to identify the different modes and are therefore not presented. The results of all these modes in Fig. 3.7 show a shift towards higher resonance frequencies for the m modes with increasing s number, as expected from the increase in root values of the Bessel function.

The Bessel function is also incorporated in the capillary dispersion relation for this cylindrical geometry. Therefore, the eigenfrequencies of the capillary dispersion relation are expected to show a similar increasing trend. To compare these eigenfrequencies to the resonance frequencies of the experimental results, we extract the maximum of the resonance curves shown in Fig. 3.7. These results are displayed as a function of the wavenumber corresponding to each mode (red) in Fig. 3.8 together with the eigenfrequencies for the same wavenumbers of the capillary dispersion relation (blue). As expected, a similar trend is observed. The offset between the two trends is expected to be

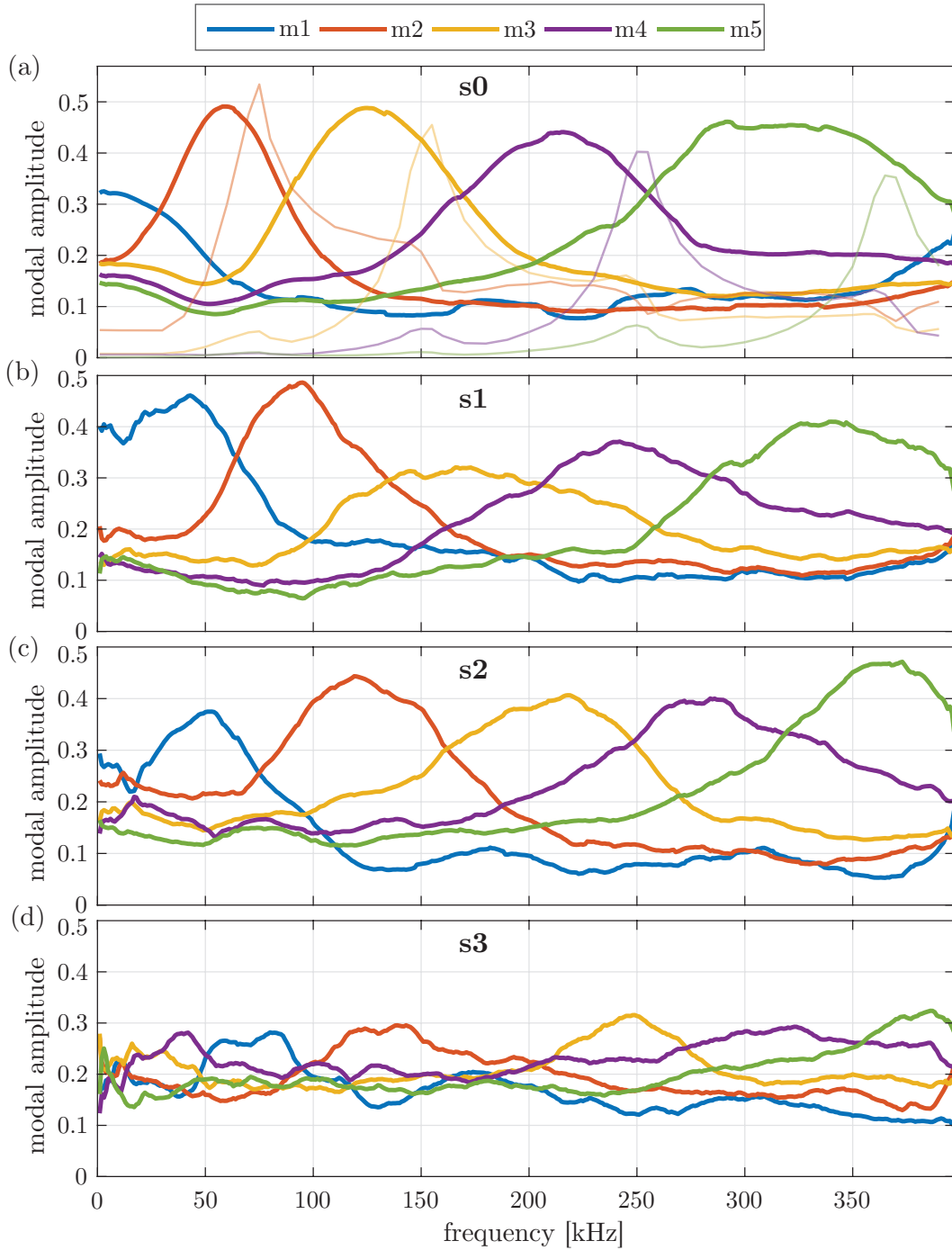


Figure 3.7: The resonance curves of modes m1 to m5 as a function of driving frequency with the amplitude normalized with the total amplitude for (a) modes s0m1 to s0m5, (b) modes s1m1 to s1m5, (c) modes s2m1 to s2m5, (d) modes s3m1 to s3m5.



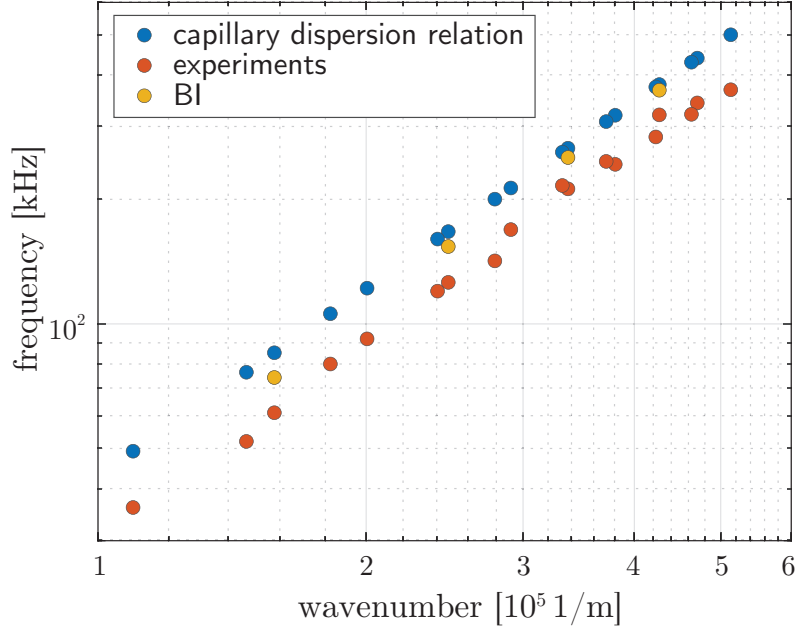


Figure 3.8: The eigenfrequencies of the capillary dispersion relation (blue) and resonance frequencies from the experiments (red) and BI simulations (yellow) versus the wavenumber for a water filled print head.

due to the capillary dispersion relation describing an undriven system, while experimentally system we investigate is a driven system.

To verify that the difference between the trends in Fig. 3.8 is indeed due to the driving, we turn to our BI simulations. The results of these simulations are shown in Fig. 3.7a for modes s0m2 to s0m5 as thin lines with the same color as the corresponding experimental results. To compare the peaks of these curves, they are also included in Fig. 3.8 (yellow datapoints). As discussed before, the non-axisymmetric modes are not driven by the liquid bulk behind the meniscus, and therefore the BI simulations only present the axisymmetric modes. The BI-derived resonance frequencies are shown not to overlap with the experimental results, although they are closer to the experimental results than those obtained from the capillary dispersion relation. Interestingly, the results do overlap when the surface tension of the liquid in the BI simulations was reduced from 72 mN/m to 50 mN/m, as shown in the appendix (Fig. 3.9). The correspondence for lower surface tension can be explained by contamination on the liquid surface during the experiments, but seems unlikely as the resonance curves in Fig. 3.7 were collected during multiple days of experimen-

tation. Another reason for the discrepancy could be the inviscid assumption of the BI method, which is the origin of the narrower resonance curves. The damping effect due to viscosity not only broadens the resonance peak, it also lowers the resonance frequency. However, water is typically considered as an inviscid liquid, which suggests that the viscosity of water should not be a major factor. One other physical aspect not taken into account is the coupling between the printhead acoustics and the meniscus oscillation shape, or the motion of the glass capillary tube during driving. Further investigation is required to fully understand the differences between the undriven system in the capillary dispersion relation and the driven system in the presented experimental results.

### 3.4 Conclusion

In summary, we have obtained high resolution experimental recordings of the meniscus modes for different driving modes of an inkjet nozzle using digital holographic microscopy. A full scan was made for the modal landscape, which was demonstrated to be independent of the printhead acoustics. In order to efficiently excite higher order meniscus shape oscillations, the acoustic resonance frequency of the printhead and the modal resonance frequency of the meniscus have to be matched. To achieve this, it has to be accurately predicted when each meniscus modes is excited, and as this is a driven system, the capillary dispersion relation does not hold. The results from BI simulations suggests the including the driving in a theoretical description should be able to predict the resonance frequencies. The accuracy can be improved further once the offset between BI and experimental results can be explained. Nevertheless, the demonstrated ability to experimentally measure the relevant phenomena at these microscopic time- and length scales opens up the world to new interface science related to high frequency and small length scale systems including inkjet printing.

### 3.5 Appendix

The boundary integral simulations were run again with a lower surface tension of the simulated liquid to improve the match with the experimental data. The resonance curve is shown in Fig. 3.9 with a surface tension of 50 mN/m. We also include these new results in the resonance frequency versus wavenumber curve in Fig 3.10

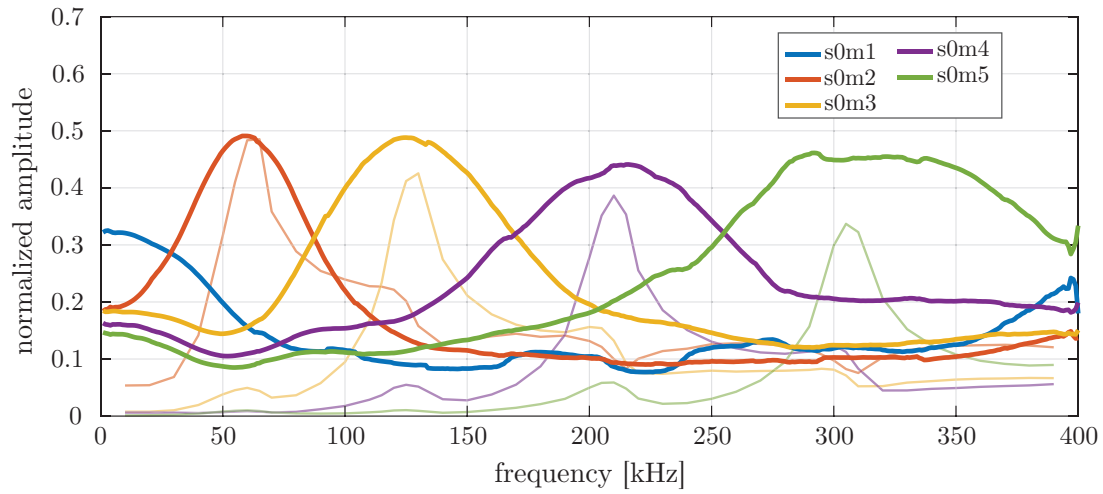


Figure 3.9: The amplitude normalized with the total amplitude for axisymmetric modes s0m1 to s0m5 as a function of frequency. The resonance curves of the BI simulations for the modes s0m2 to s0m5 are included with transparent lines of the same color as the corresponding mode. The BI simulations are set to a surface tension of 50 mN/m.

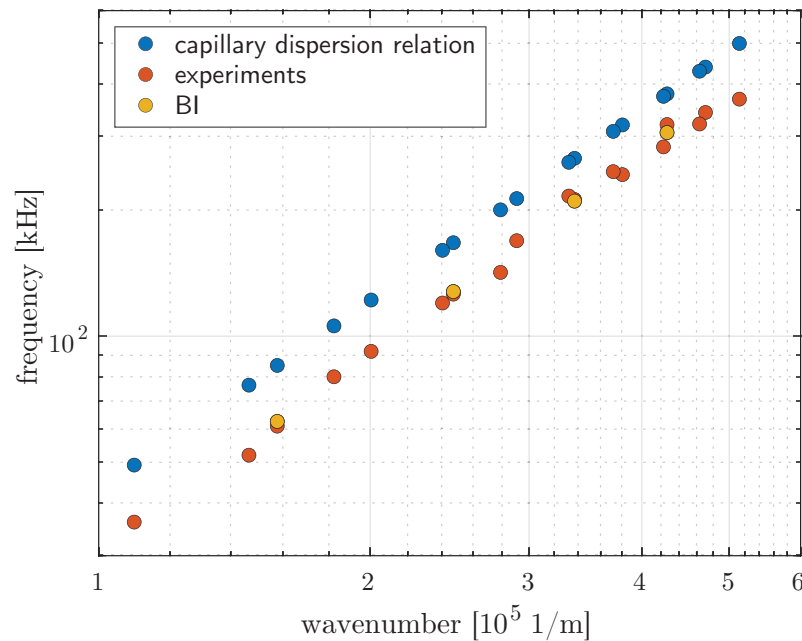


Figure 3.10: The eigenfrequencies of the capillary dispersion relation (blue) and resonance frequencies from the experiments (red) versus the wavenumber for a water filled print head. The BI simulation (yellow) now has a modified surface tension of 50 mN/m.

4

## Selective evaporation at the nozzle exit in piezoacoustic inkjet printing



□

---

Submitted as: **Maaïke Rump**, Uddalok Sen, Roger Jeurissen, Hans Reinten, Michel Ver-  
sluis, Detlef Lohse, Christian Diddens, and Tim Segers, *Selective evaporation at the nozzle  
exit in piezoacoustic inkjet printing*

## Abstract

In practical applications of inkjet printing the nozzles in a printhead have intermittent idle periods, during which ink can evaporate from the nozzle exit. Inks are usually multicomponent where each component has its own characteristic evaporation rate resulting in concentration gradients within the ink. These gradients may directly and indirectly (via Marangoni flows) alter the jetting process and thereby its reproducibility and the resulting print quality. In the present work, we study selective evaporation from an inkjet nozzle for water-glycerol mixtures. Through experiments, analytical modeling, and numerical simulations, we investigate changes in mixture composition with drying time. By monitoring the acoustics within the printhead, and subsequently modeling the system as a mass-spring-damper system, the composition of the mixture can be obtained as a function of drying time. The results from the analytical model are validated using numerical simulations of the full fluid mechanical equations governing the printhead flows and pressure fields. Furthermore, the numerical simulations reveal that the time independent concentration gradient we observe in the experiments is due to the steady state of water flux through the printhead. Finally, we measure the number of drop formation events required in this system before the mixture concentration within the nozzle attains the initial (pre-drying) value, and find a stronger than exponential trend in the number of drop formations required. These results shed light on the complex physiochemical hydrodynamics associated with the drying of ink at a printhead nozzle, and help in increasing the stability and reproducibility of inkjet printing.

## 4.1 Introduction

Drop-on-demand (DoD) inkjet printing is well-known for its highly-controlled and non-contact deposition of picoliter droplets [1–4]. The high degree of reproducibility associated with inkjet printing, along with the ability to print across a wide range of liquid properties, has opened inkjet printing to a wide use in a multitude of application areas beyond graphics printing, including the fabrication of electronic displays [6, 7], electronics printing [8–10], and in life sciences [11–13]. Typically, the inks used in inkjet printing are multicomponent, consisting not only of colored pigments and surfactants, but also of a collection of cosolvents with varying volatilities. Hence, selective evaporation of one or more of these components is inherent to inkjet printing [120].

In inkjet printing, selective evaporation is mainly studied in the context of the drying sessile droplet formed after drop impact on the substrate [121,122]. The dominant theme in this line of research has been the ‘coffee stain effect’ [123], or its suppression through, e.g. solutal [122,124–127] or thermal [128,129] Marangoni effects. Recent studies have also shown that selective evaporation can induce complex physicochemical hydrodynamics in multicomponent systems, leading to remarkable observations such as segregation [130–134] and crystallization [135,136]. Interestingly, even at small length scales, evaporation-driven segregation can cause gravity-dominated flows [137–139].

Selective evaporation is also important on the residual droplets of ink typically present on the nozzle plate [140]. Here, preferential evaporation of an ink component can introduce a concentration gradient, resulting in a Marangoni flow [140,141]. This flow can transport dirt particles towards the nozzle, which may result in bubble entrainment and nozzle failure [17,75,76] – events that are highly undesirable in inkjet printing.

A third area in inkjet printing where selective evaporation is important is within the print-nozzle itself. During the continuous ejection of droplets, the ink within the inkchannel and its nozzle remain well-mixed. However, in the course of printing a more complex and multicolored pattern—typically using multiple printheads each with thousands of nozzles—a number of nozzles remain idle during certain periods of time. During this idle period, selective evaporation takes place at the nozzle exit, thereby changing the local composition and properties of the ink, which can lead to major inaccuracies in droplet volume and speed due to a change in surface tension and/or viscosity of the ink. Hence, it is of utmost importance to be able to probe, and understand the effects of selective evaporation of ink at the nozzle exit in order to mitigate disturbing consequences and develop robust inkjet printing.

One way to probe the effect of selective evaporation on the liquid composition within the nozzle is to observe the droplet formation process. However, the extraction of physical liquid properties directly from those observations is non-trivial as there is no direct description of the droplet formation as function of the liquid properties. Instead, it requires a corresponding numerical model that accurately describes the drop formation process [29,30]. Another method is to probe the acoustic ringdown characteristics of the inkchannel by

measuring the piezo-signal after the piezo has actuated the system [1,19]. The acoustics of today's printheads—typically fabricated in silicon using micro-electromechanical systems (MEMS) technology—resemble that of a Helmholtz resonator [118,142]. The acoustic ringdown frequency is then governed by the mass of ink in the nozzle and the restrictor and by the compliance (spring constant) of the ink chamber and its ink volume (Fig. 4.1(a)). Damping results mainly from viscous dissipation in the restrictor and the nozzle. Therefore, a change in the oscillatory behavior and damping of the ink channel acoustics can directly be connected to changes in ink properties in the nozzle.

In the present work, we investigate the effects of the idle, or drying time, on the selective evaporation of a multicomponent ink at the nozzle exit of a piezo-acoustic inkjet printhead. We measure the acoustic ringdown signal of the inkchannel, and develop an analytical lumped-element model to gain physical insight into the physicochemical composition of the ink within the nozzle. We also compare the conclusions drawn from the experiments to the results of the numerical simulations of the complete evaporation and jetting process.

The chapter is organized as follows: In section 4.2, we describe the experimental procedure and in section 4.3 we introduce the analytical model for analyzing the printhead acoustics. In section 4.4, we present the numerical method and section 4.5 contains the results and the corresponding discussion. The chapter ends with conclusions and an outlook.

## 4.2 Printhead, model ink, and experimental procedure

A schematic of the employed inkchannel, which is part of an experimental printhead (Canon Production Printing, Venlo, The Netherlands), is shown in Fig. 4.1(a). The ink reservoir feeds the ink chamber with its piezo actuator via a restrictor channel. The nozzle with a radius of  $8\text{ }\mu\text{m}$  is connected to the ink chamber via a feedthrough channel. The symbols in Fig. 4.1(a) will be explained in the modeling section. The printhead was driven by a trapezoidal pulse with ramp times of  $1\text{ }\mu\text{s}$ , and a high time of  $2\text{ }\mu\text{s}$ . The waveform was generated by an arbitrary waveform generator (Agilent 33220A) and amplified by a broadband amplifier (Falco System WMA-300), resulting in a pull-push motion of the liquid in the nozzle. After driving the piezo, the ringdown of the inkchannel acoustics was measured by switching the piezo-connections to

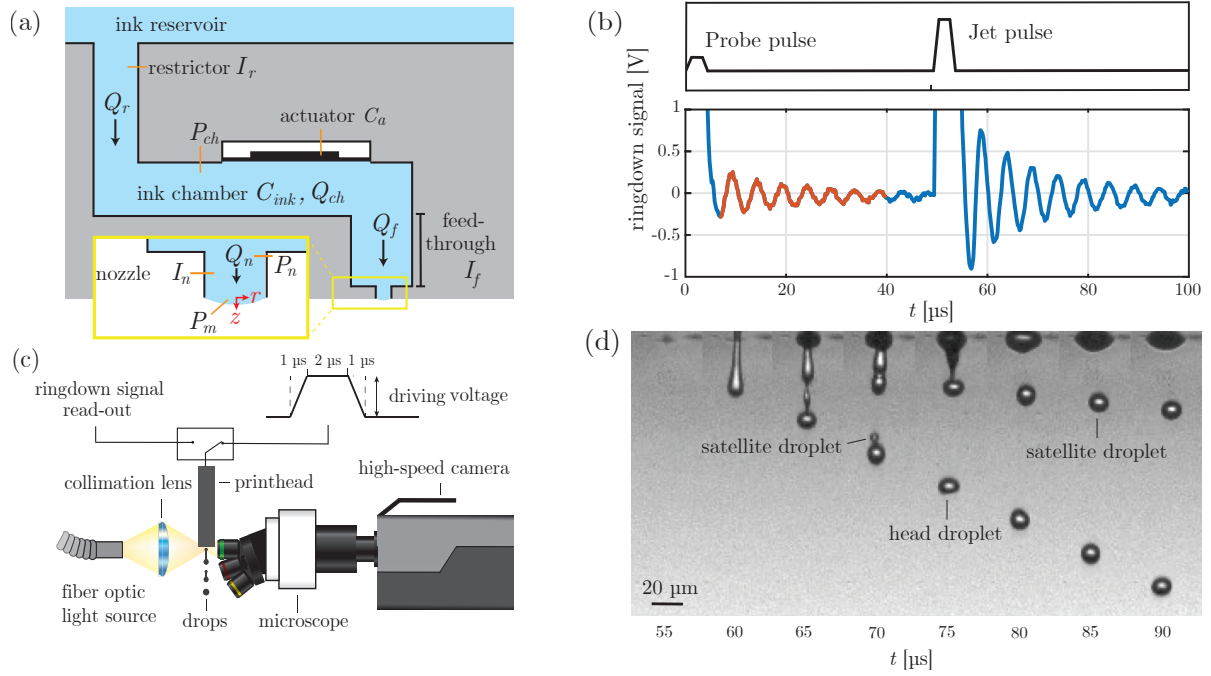


Figure 4.1: (a) A schematic of the employed ink channel with the ink chamber, restrictor, feedthrough, and nozzle. The ink channel is driven by a piezoelectric actuator attached to a flexible membrane, with compliance  $C_a$ . Also indicated are the inertances of the restrictor  $I_r$ , the feedthrough  $I_f$ , and the nozzle  $I_n$ . The arrows indicate the direction of the flow rate in the restrictor  $Q_r$ , the feedthrough  $Q_f$ , and the nozzle  $Q_n$ . The pressure in the ink chamber is indicated by  $P_{ch}$ , the pressure in between the feedthrough and nozzle is  $P_f$ , and the Laplace pressure at the meniscus is  $P_m$ . The compliance of the ink  $C_{ink}$  in the ink chamber and the flow rate through the ink chamber  $Q_{ch}$  are also indicated. (b) The driving waveforms and their corresponding piezo signals as recorded by the oscilloscope. The region that is used for the extraction of the ringdown frequency and decay rate is highlighted in red. The actuation pulses are indicated above the graph. (c) A schematic of the experimental setup. The printhead was driven by a 1-2-1 μs trapezoidal pulse. Subsequently, the piezo connections switched to the read-out circuit to probe the ringdown of the inkchannel acoustics. A light source back-illuminated the jetted droplets and images were captured by a high-speed camera. (d) A typical drop formation process with no drying time.



an oscilloscope (Tektronix TDS5034B) via a transimpedance amplifier as described in [140].

The model ink used in the present study was a mixture of 10 wt% glycerol (Sigma-Aldrich) in MilliQ water, which has a density  $\rho$  of 1020.4 kg/m<sup>3</sup> [143], a viscosity  $\mu$  of 1.1 mPa s [144], and a surface tension  $\gamma$  of 68.3 mN/m [145]. To prevent the liquid from dripping out of the printhead due to gravity, the ink channel was always kept at an underpressure of 8 mbar.

The experimental measurement procedure was as follows. First, 999 droplets were jetted at a DoD frequency of 1 kHz to make sure that the liquid mixture in the nozzle had the same composition as that in the bulk. Whether or not this amount of jetted droplets was enough was verified using the measured resonance frequency, as we will also describe in section 4.5.3. Next, the jetting was stopped for the predetermined drying time, which led to evaporation from the stationary liquid meniscus at the nozzle exit. The relative humidity in the lab was 38 %  $\pm$  3 %. By purging nitrogen gas across the nozzle plate, measurements at low relative humidity (0 %) were performed. When the desired drying time had passed (the control parameter in the experiments), the piezo was driven by two pulses: A 5 V probe pulse and a 20 V jet pulse (see Fig. 4.1b). The amplitude of the probe pulse was a quarter the amplitude of the jet pulse to drive the inkchannel acoustics while preventing liquid to be jetted outward. The second pulse was at full amplitude and produced a droplet. The ringdown signals of both pulses were recorded and the signal due to the probe pulse (red curve in Fig. 4.1b) was used for further analysis in Matlab, where the ringdown frequency and decay rate of the ringdown signal were determined by fitting a damped cosine:  $e^{-\beta t} \cos \omega t$ , where  $\beta$  is the decay rate due to damping, and  $\omega$  the angular frequency.

The droplet formation process driven by the jet pulse was recorded using a high-speed camera (Shimadzu HPV-X2, 10<sup>6</sup> frames-per-second). It allowed validation of our finite element numerical simulations to thereby gain insight in the local concentration gradients within the nozzle and the feedthrough. The imaging setup (Fig. 4.1c) consisted of a modular microscope (BXFM-F, BXFM-ILHS, Olympus) and a 20 $\times$  objective (SLMPLN, Olympus). The resulting imaging resolution was 1.86  $\mu$ m/pixel. Back-illumination was provided by a fiber-optic light source (LS-M352, Sumita). The waveform generator and camera were triggered with their appropriate delays at nanosecond precision

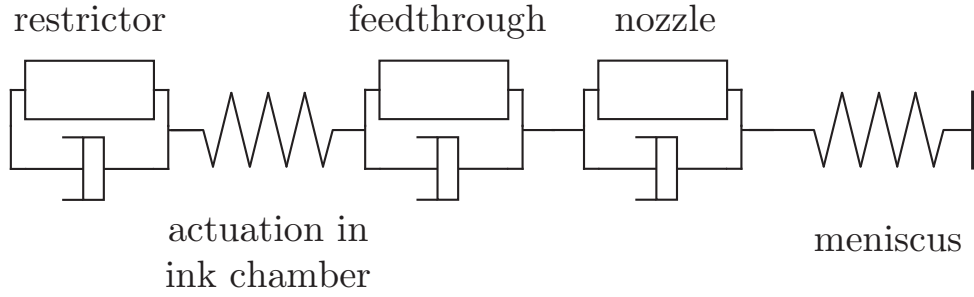


Figure 4.2: Lumped element model of the ink channel shown in Fig. 4.1a where the restrictor, feedthrough, and nozzle are composed of a mass and a damper. The ink chamber and meniscus are both represented by a spring.

using a pulse-delay generator (BNC 575, Berkeley Nucleonics Corp). A typical droplet formation process is shown in Fig. 4.1d. The figure shows a liquid jet being ejected, which eventually breaks up to form a head droplet and a satellite droplet [32].

### 4.3 Analytical model of the printhead acoustics

A lumped element model, similar to that of ref. [142], was developed to describe the acoustics in the inkchannel to relate the measured ringdown signal to the mixture composition in the nozzle (see Fig. 4.2). Unlike in [142], we describe the acoustics in the frequency domain to include viscous damping, similar to what was done in [19]. The flow in the nozzle in response to the probe pulse is oscillatory and the resulting flow profile depends on the competition between the inertia of the oscillating velocity field and viscosity, characterized by the Womersley number in the nozzle [146]:

$$Wo_n = R_n \sqrt{\frac{\omega \rho_n}{\mu_n}}, \quad (4.1)$$

with  $R_n$  the radius of the nozzle,  $\omega$  the angular frequency of oscillations, and  $\rho_n$  and  $\mu_n$  the ink density and dynamic viscosity in the nozzle, respectively. The flow rate  $Q_n$  in a cylindrical nozzle is determined by, next to the pressure pulse, the oscillation frequency, and has been derived analytically in closed form by Womersley [146]. Here, it is rewritten as the ratio of the pressure difference across the inertance of the nozzle ( $P_f - P_m$ , see Fig. 4.1a) to the flow rate in the nozzle ( $Q_n$ ) to obtain the acoustic impedance  $Z_n$  of the nozzle,

given by:

$$Z_n = \frac{P_f - P_m}{Q_n} = i\omega I_n \left( 1 - \frac{2J_1(i^{3/2}W_{on})}{i^{3/2}W_{on}J_0(i^{3/2}W_{on})} \right)^{-1}, \quad (4.2)$$

with  $P_f$  the pressure at the nozzle inlet,  $P_m$  the Laplace pressure at the meniscus (described in more detail after Eq. 4.7), and  $J_0$  and  $J_1$  the ordinary Bessel functions of the first kind of zeroth and first order, respectively.  $I_n$  is the acoustic inertance of the nozzle, given by:

$$I_n = \frac{\rho_n L_n}{A_n}, \quad (4.3)$$

with  $A_n$  the cross-sectional area of the nozzle and  $L_n$  the length of the nozzle. The effective inertance of the nozzle is larger than that given by Eq. 4.3 as the fluid just outside the nozzle in the feedthrough takes part in the oscillations. This increase in inertance is captured by an increase in nozzle length of:  $\Delta L = \pi R_n/4$ , as described by Landau and Lifshitz [147], amounting to  $I_n = 1.08 \times 10^8 \text{ kg/m}^4$  for the 10 wt% glycerol solution. For the acoustic impedance of the restrictor  $Z_r$  and the feedthrough  $Z_f$ , similar equations are used:

$$Z_r = -\frac{P_{ch}}{Q_r} = i\omega I_r \left( 1 - \frac{2J_1(i^{3/2}W_{or})}{i^{3/2}W_{or}J_0(i^{3/2}W_{or})} \right)^{-1}, \quad (4.4)$$

$$Z_f = \frac{P_{ch} - P_f}{Q_f} = i\omega I_f \left( 1 - \frac{2J_1(i^{3/2}W_{of})}{i^{3/2}W_{of}J_0(i^{3/2}W_{of})} \right)^{-1}, \quad (4.5)$$

with the corresponding inertance of the restrictor  $I_r = 1.19 \times 10^8 \text{ kg/m}^4$  and that of the feedthrough  $I_f = 1.26 \times 10^7 \text{ kg/m}^4$ . The inner dimensions of the printhead can deviate from the intended values due to fabrication inaccuracies of the MEMS chip. As the exact dimensions could not be measured, we used the length of the restrictor as a fitting parameter.

The total compliance of the ink channel  $C_{ch}$  (volume change per unit pressure) has contributions from the flexible piezo actuator  $C_a$  and the volume of ink  $V_{ink}$  in the ink chamber ( $C_{ink} = V_{ink}\rho c^2$ , with  $c$  the speed of sound in the ink) which leads to  $C_{ch} = C_a + C_{ink}$ . The total compliance of the employed ink channel was  $C_{ch} = 10.8 \times 10^{-21} \text{ m}^3/\text{Pa}$ , as obtained from investigations on the resonance behavior of the printhead [1]. The pressure change in the ink

chamber (Fig. 4.1a) due to its change in volume is given by:

$$P_{ch} = \frac{1}{C_{ch}}(V_r - V_f), \quad (4.6)$$

with  $V_r$  the displaced volume from the restrictor into the ink chamber and  $V_f$  that from the ink chamber into the feedthrough. The flow rate into the ink chamber equals  $Q_{ch} = Q_r - Q_f$ , where the flow rate is the derivative of the displaced volume with respect to time. By assuming simple harmonic motion ( $V(t) = V_A e^{i\omega t}$ , with  $V_A$  a constant amplitude), it follows that the acoustic impedance of the compliant ink channel is given by:

$$Z_{ch} = \frac{P_{ch}}{Q_{ch}} = \frac{1}{i\omega C_{ch}}. \quad (4.7)$$

The surface tension of the meniscus at the nozzle exit adds another compliance to the system. The compliance of the meniscus can be estimated from the amount of liquid volume sustained by the surface tension of the meniscus, as shown in [118]. However, instead of assuming that the meniscus protrudes from the nozzle as a hemisphere, which is non-linear, we assume small displacements, for which the meniscus is approximately a paraboloid. The meniscus surface protrudes from the plane of the nozzle plate by a distance  $z(r)$ , which is a function of the radial coordinate  $r$ :

$$z(r) = z_m \left( 1 - \frac{r^2}{R_n^2} \right), \quad (4.8)$$

with  $z_m$  the maximum height of the meniscus. The Laplace pressure  $P_m$  is the product of surface tension  $\gamma$  and the surface curvature  $\kappa = -\nabla^2 z = 4z_m/R_n^2$ . The volume displacement is obtained by integrating the meniscus displacement over the area of the meniscus, resulting in the compliance of the meniscus:

$$C_m = \frac{V_m}{P_m} = \frac{z_m \frac{1}{2} \pi R_n^2}{\gamma 4 z_m R_n^{-2}} = \frac{\pi R_n^4}{8\gamma}, \quad (4.9)$$

which is independent of  $z_m$  and results in  $C_m = 23.6 \times 10^{-21} \text{ m}^3/\text{Pa}$ . The acoustic impedance of the meniscus is then given by:

$$Z_m = \frac{P_m}{Q_m} = \frac{1}{i\omega C_m}. \quad (4.10)$$

To find the resonance frequencies of the inkchannel represented by the coupled impedances, mass continuity from the feedthrough to the nozzle, i.e.  $Q_f =$

$Q_n$ , is added to the system of equations in order to balance the number of unknown variables with the number of equations such that the coupled system of equations can be solved. The expressions for the impedances are then written in matrix form [142], as follows:

$$\begin{bmatrix} 0 & 0 & 0 & 0 & 1 & -1 \\ 0 & 1 & 0 & 0 & -\frac{1}{i\omega C_m} & 0 \\ 0 & -1 & 1 & 0 & -i\omega I_n f(Wo_n) & 0 \\ 1 & 0 & -1 & 0 & 0 & -i\omega I_f f(Wo_f) \\ 1 & 0 & 0 & -\frac{1}{i\omega C_{ch}} & 0 & \frac{1}{i\omega C_{ch}} \\ -1 & 0 & 0 & -i\omega I_r f(Wo_r) & 0 & 0 \end{bmatrix} \times \begin{bmatrix} P_{ch} \\ P_m \\ P_n \\ Q_r \\ Q_n \\ Q_f \end{bmatrix} = 0, \quad (4.11)$$

The corresponding determinant is found to be:

$$\begin{aligned} & -\omega^2 I_r f(Wo_r) (I_f f(Wo_f) + I_n f(Wo_n)) \\ & + \frac{I_n f(Wo_n) + I_f f(Wo_f) + I_r f(Wo_r)}{C_{ch}} \\ & + \frac{I_r f(Wo_r)}{C_m} - \frac{1}{\omega^2 C_{ch} C_m}. \end{aligned} \quad (4.12)$$

with:

$$f(Wo) = \left( 1 - \frac{2J_1(i^{3/2}Wo)}{i^{3/2}WoJ_0(i^{3/2}Wo)} \right)^{-1}. \quad (4.13)$$

The determinant in Eq. 4.12 of the  $6 \times 6$  matrix in Eq. 4.11 is equated to zero to find the resonance frequencies of the system:

$$\begin{aligned} & -\omega^4 I_r f(Wo_r) [I_f f(Wo_f) + I_n f(Wo_n)] \\ & + \omega^2 \left[ \frac{I_n f(Wo_n) + I_f f(Wo_f) + I_r f(Wo_r)}{C_{ch}} + \frac{I_r f(Wo_r)}{C_m} \right] \\ & - \frac{1}{C_{ch} C_m} = 0. \end{aligned} \quad (4.14)$$

The complex solution of this determinant gives the oscillation frequencies of the system, where the real part is the ringdown frequency. For a finite viscosity, the eigenvalue is complex and the positive imaginary part is the decay rate, showing that energy is dissipated by damping in the system. As the equation is not a polynomial function, we employed Matlab's `fsolve` function (Levenberg-Marquardt method) to find the roots. The root corresponding to the Helmholtz resonance mode of the system was found by providing the

Helmholtz resonance frequency of the inviscid case as the initial value. First, this was done for the case where the model ink viscosity, density, and surface tension correspond to a 10 wt% glycerol in water mixture. The root that was found was then used for the next iteration of the model where the concentration of glycerol in the nozzle was increased by 1 wt%. This process was repeated until the 100 wt% glycerol concentration was reached. The viscosity, density, and surface tension of glycerol-water mixtures were obtained from [143–145]. The glycerol concentration in the analytical model is only changed in the nozzle and it was kept constant in the rest of the system at all times.

In addition to the ringdown frequency and decay rate, we also compute the ringdown signal itself. We therefore first determine the total lumped acoustic impedance of the ink channel:

$$Z_{tot} = \left( \frac{1}{Z_r} + \frac{1}{Z_n + Z_f + Z_m} + \frac{1}{Z_{ch}} \right)^{-1}. \quad (4.15)$$

The flow rates through the feedthrough and nozzle toward the meniscus are the same, assuming incompressibility, and therefore,  $Z_n$ ,  $Z_f$ , and  $Z_m$  are summed. The inverse sum is taken with the other components as these impedances are connected in parallel. The real part of  $Z_{tot}$  is plotted in Fig. 4.3a as function of frequency for 10 wt% glycerol (solid blue curve), for 10 wt% glycerol with its viscosity artificially doubled (red curve), and 10 wt% glycerol with its surface tension artificially halved (green curve). The peak at 200 kHz corresponds to the Helmholtz resonance mode of the system where the masses (inertances) of the restrictor and nozzle oscillate 180° out-of-phase and the spring constant is given by the compliance of the ink chamber [142]. The low frequency mode around 60 kHz corresponds to the slosh mode that is characterized by the in-phase movement of the masses of the nozzle, feedthrough, ink chamber, and restrictor against the compliance of the meniscus [119] such that for the inviscid case:

$$f_{slosh} = \frac{1}{2\pi} \sqrt{\frac{1}{C_m(I_r + I_f + I_n)}} = 69 \text{ kHz}. \quad (4.16)$$

Note that the inertance of the ink chamber was neglected as it is much smaller than the other contributions. Also note from Fig. 4.3a that both the frequency of the modes and their damping (width of the peak) are sensitive to the liquid properties in the nozzle. The frequency of the slosh mode is mostly affected by a change in surface tension, while its damping (peak width) is only sensitive to viscosity. The Helmholtz resonance frequency decreases by an increase in

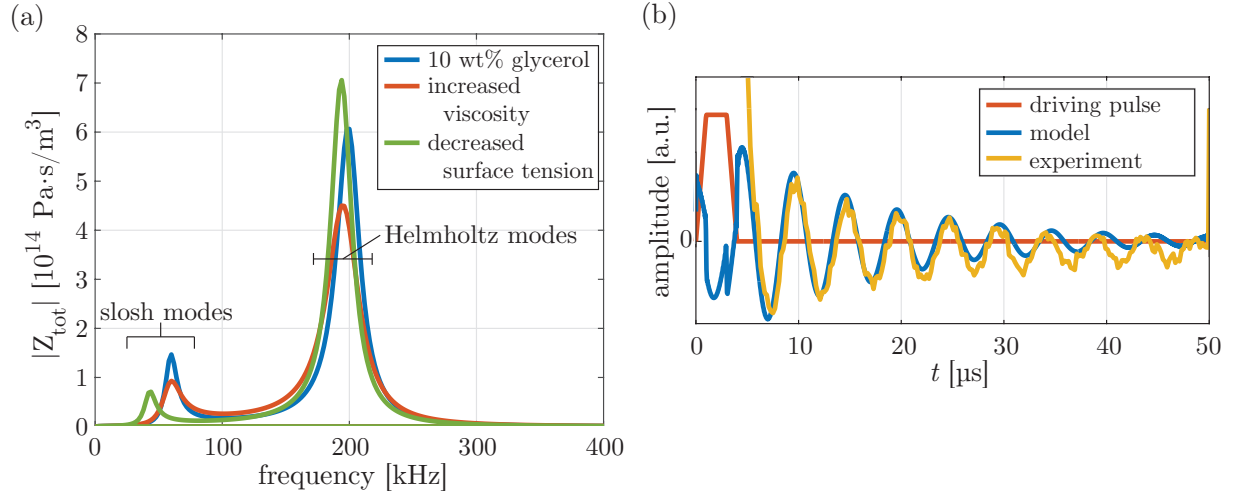


Figure 4.3: (a) Real part of the total impedance given by Eq. 4.15 with a 10 wt% glycerol concentration in all components of the printhead (blue), with double the viscosity in the nozzle (red), and half the surface tension in the nozzle (green). (b) Driving pulse (red) with the corresponding ringdown signal for the 10 wt% glycerol experiment (yellow) with no drying time, and the analytical model (blue).

viscosity and a decrease in surface tension. The damping of the Helmholtz mode increases with an increase in viscosity.

The computation of the ringdown signal is continued by relating the pressure in the channel to the piezo driving voltage. In the linear regime of the piezo, the volume change at constant pressure in the ink channel is proportional to the driving voltage with a proportionality constant  $\alpha$  (units of  $\text{m}^3/\text{V}$ ). Using the definition of the acoustic impedance  $Z = P/Q$ , the pressure in the ink channel in response to a driving pulse can be expressed as:

$$p = i\omega\alpha Z_{tot} V_{pulse}(\omega), \quad (4.17)$$

with  $V_{pulse}(\omega)$  the discrete Fourier transform of the time-dependent driving voltage.

The piezo ringdown signal in the experiments is a measure of the piezo current [148]. The linearized relation between piezo current and pressure in the ink channel is given by [19]:

$$I(\omega) = i\omega\alpha p, \quad (4.18)$$



such that the modeled piezo ringdown signal in the frequency domain becomes

$$I(\omega) = -\omega^2 \alpha^2 Z_{tot} V_{pulse}(\omega). \quad (4.19)$$

Eq. (4.19) is then inverse-Fourier-transformed to obtain the piezo ringdown signal in the time domain. A comparison between the modeled piezo ringdown signal and the experimental ringdown signal is shown in Fig. 4.3b. The experimental ringdown signal only appears after 5  $\mu$ s because the amplitude of the probe pulse is a lot higher than the amplitude of the ringdown signal (see Fig. 4.1b). Figure 4.3b shows the modeled piezo ringdown signal for 10 wt% glycerol, along with the experimental result for a drying time of 1.5 ms. The comparison between the results from the model and from the experiment show good agreement.

## 4.4 Numerical model

While the average concentration of glycerol in the nozzle can be estimated from the ringdown signal using the analytical model, a numerical model can be used to simulate the drying process and thereby provide key insight into the dynamical process of glycerol diffusion leading to its enhanced concentration. Moreover, the simulations can provide insight into the local distribution of glycerol in the nozzle and the jetted droplet, information that is not available in the experiment.

Simulating the entire process, i.e. the selective evaporation of water from the nozzle followed by a jetting event, is a challenging problem. The first challenge is that the time scales are drastically different, namely evaporation happening for a duration of hundreds of seconds, whereas the jetting is on the order of microseconds. This demands a flexible and stable temporal integration method that can easily switch the relevant time scales by several orders of magnitude. Furthermore, the scenario is inherently a multi-component and multi-phase problem with phase transitions and mass transfer, while the fluid properties depend on the local liquid composition. Consequently, the numerical implementation requires to allow for multi-component mass transfer across the liquid-gas interface, account for Marangoni flow, and must consider local variations of the mass density and viscosity. Finally, resolving the entire jetting dynamics would demand considering the fluid-structure interaction of the actuating piezo and the coupling between the free-surface flow dynamics at the nozzle and acoustics in the chamber. In this section, we describe how these

challenges are tackled in the present simulation framework.

As a general framework, we have used a sharp-interface arbitrary Lagrangian-Eulerian finite element method (ALE-FEM) expressed in axisymmetric cylindrical coordinates. This comes with the benefit that the liquid-gas interfaces are always exactly represented by sharp curves, which easily allows to incorporate Marangoni flow and mass transfer. Furthermore, FEM is solved implicitly via Newton's method, which provides a stable solution method along with flexible time stepping on the two different time scales of evaporation and jetting. The implementation is based on the finite element library OOMPH-LIB [149, 150].

#### 4.4.1 Evaporation phase

During the evaporation phase, the fluid dynamical equations in both the surrounding gas and the liquid phase are solved. Since there is no actuation, i.e. no applied pulse, all parts of the driving are deactivated in this phase. However, if long drying times are considered, it is important to consider the entire system, i.e. from the nozzle over the feedthrough, the chamber and the restrictor into the ink reservoir domain. Otherwise, the diffusive replenishment of water from the ink reservoir domain is not accurately accounted for in the long-time limit. In the following, the governing equations for solving the evaporation phase are described. These resemble the equations which have been successfully used in previous works on the evaporation of multi-component droplets on substrates, e.g. in [151].

#### Vapor diffusion in the gas phase

We assume diffusion-limited evaporation, i.e. the evaporation rate of water can be obtained by solving the vapor diffusion equation for the partial mass density  $c$  of water vapor in the gas phase by:

$$\partial_t c = D_{\text{vap}} \nabla^2 c, \quad (4.20)$$

subject to the boundary conditions:

$$c = c_{\text{VLE}}(w) \quad \text{at the liquid-gas interface} \quad (4.21)$$

$$c = c_{\infty} \quad \text{far away,} \quad (4.22)$$

i.e. the vapor-liquid equilibrium (VLE) according to Raoult's law  $c_{\text{VLE}}(w)$  at the liquid-gas interface, where  $w$  is the concentration of water (as weight

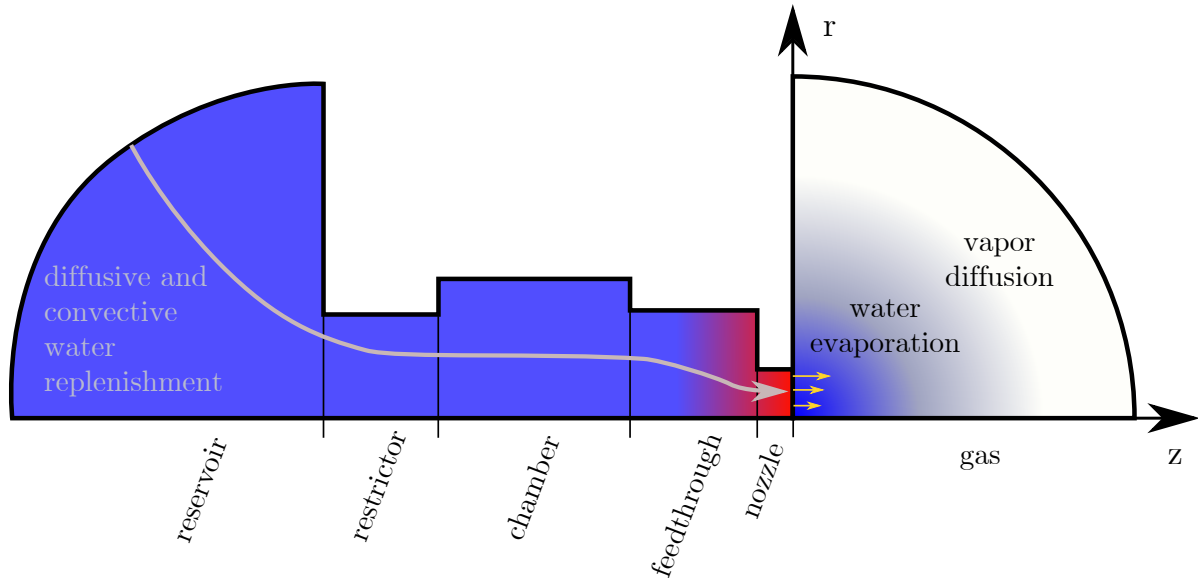


Figure 4.4: Schematic of the evaporation phase (not true to scale). The print-head geometry is assumed to be axisymmetric. Water evaporates into the gas phase, leaving behind an enhanced glycerol concentration. Water is replenished by diffusion and convection through the entire system towards the nozzle, as indicated by the gray arrow.

fraction) in the liquid. For this condition, the liquid water concentration  $w$  is converted to mole fractions, and the corresponding activity coefficient for the glycerol-water mixture is calculated via AIOMFAC [152] to account for the non-ideality of the mixture within Raoult's law. The ambient water vapor concentration  $c_\infty$  far away is not directly imposed at the distant boundaries of the considered gas domain, since it would induce considerable errors originating from the finite size of the considered gas mesh. Instead a Robin boundary condition mimicking an infinite domain is used, which is based on a multi-pole expansion truncated at monopole order [153]. The mass-transfer rate of water is given by the diffusive flux at the liquid-gas interface, i.e. by taking the normal derivative:

$$j = -D_{\text{vap}} \partial_n c. \quad (4.23)$$

In comparison to water, the volatility of glycerol is negligible, so that we do not account for glycerol evaporation here.

### Multi-component flow in the liquid phase

The bulk flow in the liquid phase is governed by the Navier-Stokes equations with a composition-dependent mass density  $\rho$  and viscosity  $\mu$  together with the advection-diffusion equation for the water concentration  $w$  with a composition-dependent diffusivity  $D(w)$ :

$$\rho (\partial_t \mathbf{u} + \mathbf{u} \cdot \nabla \mathbf{u}) = -\nabla p + \nabla \cdot [\mu (\nabla \mathbf{u} + (\nabla \mathbf{u})^t)], \quad (4.24)$$

$$\partial_t \rho + \nabla \cdot (\rho \mathbf{u}) = 0, \quad (4.25)$$

$$\rho (\partial_t w + \mathbf{u} \cdot \nabla w) = \nabla \cdot (\rho D \nabla w). \quad (4.26)$$

The composition-dependent properties, i.e.  $\rho(w)$ ,  $\mu(w)$ ,  $D(w)$  and also the surface tension  $\sigma(w)$  were obtained by fitting experimental data from [144, 145, 154]. At the liquid-gas interface, normal and tangential stress balances, i.e. Laplace pressure and Marangoni shear, are applied without consideration of the stresses in the gas phase, which can be disregarded due to the small density and viscosity ratios:

$$\mathbf{n} \cdot \mathbf{T} \cdot \mathbf{n} = \kappa \sigma \quad (4.27)$$

$$\mathbf{n} \cdot \mathbf{T} \cdot \mathbf{t} = \nabla_S \sigma, \quad (4.28)$$

with the stress tensor  $\mathbf{T} = -p\mathbf{1} + \mu(\nabla \mathbf{u} + (\nabla \mathbf{u})^t)$  and the normal and tangent  $\mathbf{n}$  and  $\mathbf{t}$ , respectively.  $\kappa$  is, as before, the curvature of the interface and  $\nabla_S$  is the surface gradient operator. The kinematic boundary condition considering water evaporation reads

$$\rho (\mathbf{u} - \mathbf{u}_I) \cdot \mathbf{n} = j, \quad (4.29)$$

which connects the normal liquid bulk velocity  $\mathbf{u}$  with the normal interface velocity  $\mathbf{u}_I$  via the evaporation rate  $j$ . The liquid-solid interfaces within the simulated printhead geometry are no-slip boundary conditions. Finally, the evaporation of water leads to a change of the liquid composition near the interface, which is incorporated via the boundary condition

$$-\rho D \nabla w \cdot \mathbf{n} = (1 - w)j. \quad (4.30)$$

The far field in the reservoir is again mimicking an infinite domain by a far-field Robin boundary condition. Furthermore, a constant underpressure of 8 mbar is applied as in the experiments, which results in a slightly inwardly curved meniscus.

#### 4.4.2 Probe pulse and jetting pulse

When it comes to jetting, the relevant time scales are several orders of magnitude smaller than those during the drying phase. Given the short time scales and the fast convection velocities during jetting, the diffusion-limited evaporation model as used during the evaporation phase is also questionable in this stage. Therefore, the gas phase and with it the evaporation dynamics are disregarded during the jetting process. The friction of the jetted droplet in the gas phase is in general not entirely negligible, but the influence on the drop formation is. This has been shown by the excellent agreement between experiments and frictionless numerics in slender jet approximation [94]. In the ALE-FEM simulation here, the deactivation of the gas phase and evaporation implies setting  $j = 0$  in Eqs. (4.29) and (4.30). For the comparison with the analytical model evaporation is not considered at all, but the nozzle is artificially filled with a prescribed glycerol concentration.

#### Modeling of the chamber and the restrictor dynamics

To account for the acoustics in the chamber, the simulation domain is truncated at the transition from the feedthrough to the chamber. The flow in the chamber is hence not solved directly, but instead the dynamics is characterized by the chamber pressure  $P_{\text{ch}}$  like in the analytical model, Eq. 5. The chamber pressure dynamics is therefore approximated by the following first order ODE:

$$C_{\text{ch}} \dot{P}_{\text{ch}} = -\alpha \dot{V}_{\text{pulse}} + Q_f - Q_r. \quad (4.31)$$

Here,  $C_{\text{ch}}$  is the acoustic compliance of the chamber,  $\alpha$  is a conversion factor from the applied voltage to a displaced volume due to the actuation by the pulse  $V_{\text{pulse}}$ . It is noteworthy that  $\alpha$  is the only free parameter in the entire simulations, which has been fitted to reproduce the best match with the experimental jetting (cf. Fig. 5). Finally, the chamber pressure is influenced by in- and outflow from both sides, i.e. the feedthrough and the restrictor, which are represented by the terms  $Q_f$  and  $Q_r$ , respectively. The flow in the feedthrough and the nozzle is solved as before by the full multi-component flow dynamics, i.e. Eqs. (4.24) to (4.29). However, at the top of the feedthrough, where it is usually connected to the chamber, the radial velocity  $u_r$  is set to zero, whereas the chamber pressure  $P_{\text{ch}}$  (minus the constant underpressure of 8 mbar) is imposed as driving force. The volume flux  $Q_f$  is then directly obtained by integration of the axial velocity over the fictive interface to the

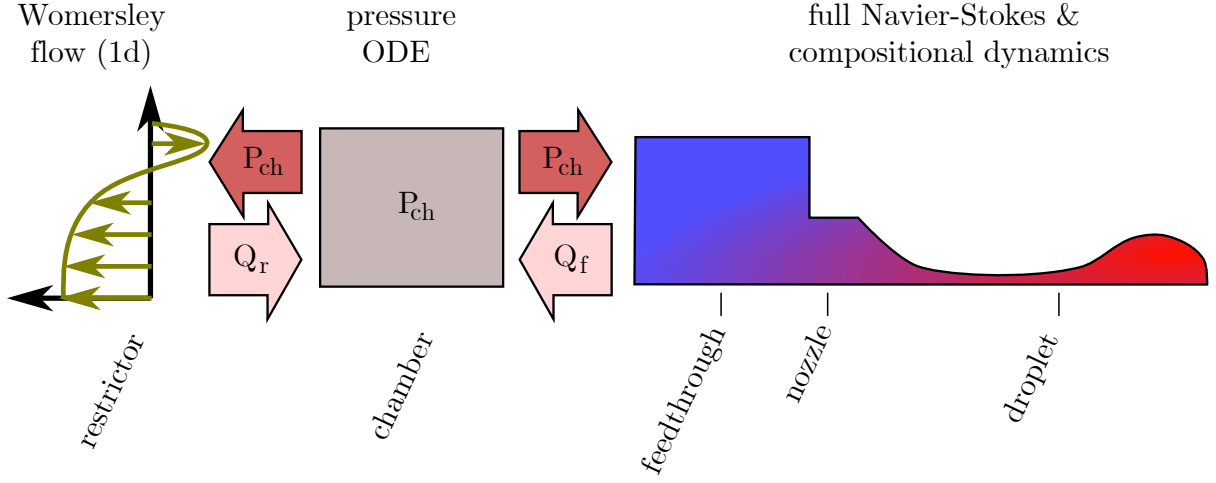


Figure 4.5: Schematic during the probe pulse and in the jetting phase (not to scale). The axial restrictor flow is solved on a 1D radial mesh, the chamber pressure is approximated by the ODE of eq. (4.31) and only the part comprising feedthrough, nozzle, and the droplet formation is solved by the full flow and compositional equations. The color gradient from blue to red sketches the increase in glycerol concentration.

chamber at the top of the feedthrough, i.e.

$$Q_f = 2\pi \int u_z r \, dr. \quad (4.32)$$

The flow in the restrictor is treated in a similar way. However, since the restrictor geometry can be assumed to be a long cylinder (radius  $R_r$  and length  $L_r$ ) and given the fact that the liquid mixture inside the restrictor is nearly homogeneous, it is sufficient to solve the axial Womersley flow [146] on a one-dimensional radial mesh, i.e.

$$\rho \partial_t u_z = \frac{P_{ch}}{L_r} + \mu \left( \frac{1}{r} \partial_r u_z + \partial_r^2 u_z \right) \quad (4.33)$$

with  $u_z|_{r=R_r} = 0$ . The feedback to the chamber pressure  $P_{ch}$  via the volume flux  $Q_r$  is then calculated analogously to eq. (4.32).

### Sharp-interface ALE method with topological changes

While the sharp-interface ALE method has the benefits of easily and accurately incorporating Marangoni flow and evaporation, one of its major drawbacks compared to e.g. volume-of-fluid or phase-field models is the treatment

of topological changes, i.e. the pinch-off of droplets from the jet and their potential in-air coalescence. For simple axisymmetric problems, however, these events can be treated by mesh reconstruction, i.e. after each accepted time step, the liquid-gas interface is tested for parts that run nearly parallel to the axis of symmetry. If these are close to the axis (i.e. within 2 % of the nozzle radius), the pinch-off position is estimated by finding the thinnest spot of the tail that also shows a profile of local relative outflux, i.e. a relative velocity that changes sign in the vicinity. Whenever such a position can be found, the liquid-gas mesh is artificially split and reconnected to the axis of symmetry. Afterwards, a new separated mesh is constructed and all relevant fields are interpolated from the previous mesh, whereby the data of nodes at the liquid-gas interface are interpolated by the data stemming from the previous, still connected, interface. A similar treatment is done for droplet coalescence. Here, the liquid-gas interface is re-connected, whenever two distinct parts of the interface overlap at the axis of symmetry.

While this method introduces an artificial length scale, i.e. the thickness threshold for a pinch-off to occur, all other numerical methods already intrinsically have these artificial scales, be it the cell size in a volume-of-fluid approach, the interface thickness in a phase field approach or the regularization radius in the slender jet (lubrication theory) method [155]. The method used here for topological changes also showed perfect agreement with experiments on droplets colliding in mid-air [156].

## 4.5 Results & discussion

### 4.5.1 Influence of drying on drop formation

Figure 4.6 compares snapshots from numerical simulations and experiments for a drying time of 100 ms. Figure 4.6(a) shows the water-vapor concentration field around the nozzle after a drying time of 100 ms. The evaporation rate is indicated by the green arrows and it is at maximum at the nozzle boundaries, as expected. The velocity field in the liquid is shown in the left half of each numerical snapshot (colorbar on top of the snapshots). The right half of the numerical snapshots shows the glycerol concentration (colorbar constant for all images). Good agreement is observed between the numerical and the experimental results. Note that the probe pulse alters the glycerol distribution at the nozzle exit. Furthermore, we observe that the glycerol enriched liquid



at the nozzle exit forms a shell around the jet and subsequently around the droplets.

The final snapshot in Fig. 4.6(g) shows the comparison between numerics and experiment for when no drying has taken place (which is taken as 1.5 ms in the experiments). Note that the drop formation is very similar to the case with 100 ms drying time even though the doubled glycerol concentration at the nozzle exit after 100 ms drying time (Fig. 4.6(a)). Nevertheless, the modified liquid properties will most likely change the drying and spreading behavior of the printed droplet and thus this observation is in any case important for the overall inkjet printing process.

In Fig. 4.6h we see in blue the driving voltage of the piezo, with first the probe pulse and later the jet pulse. As a response to these driving pulses, we see in red the numerically obtained pressure in the ink chamber. The next section focuses on the measurements of this ringdown signal of the ink channel acoustics, to study whether the changes in ink properties in the nozzle due to selective evaporation can be acoustically monitored.

### 4.5.2 Acoustically probing the drying phenomenon

The experimental results of the ringdown frequency and decay rate for different drying times are shown in Fig. 4.7a and Fig. 4.7b, respectively. For the experiments at a relative humidity of 38 %, there are two measurements points at each drying time, each from a different experiment, demonstrating its reproducibility. From Fig. 4.7a, it can be observed that the ringdown frequency decreases with increasing drying time, and the decay rate in Fig. 4.7b shows an increase with drying time, but only after 1 s. Furthermore, a decrease in humidity seems to amplify the changes in ringdown frequency and decay rate, as observed from the 0 % relative humidity measurements in Figs. 4.7a and 4.7b (light blue datapoints). This suggests that these changes are a consequence of the faster drying process. Finally, the low relative humidity datapoints seem to plateau after a drying time of 2000 s for both the ringdown frequency and the decay rate. This plateau will be explained later from our numerical simulations.

First, the analytical model described in section 4.3 is used to show that the ringdown frequency and decay rate change by varying the glycerol concentration in the nozzle. The resulting output from the model is shown in Fig. 4.8

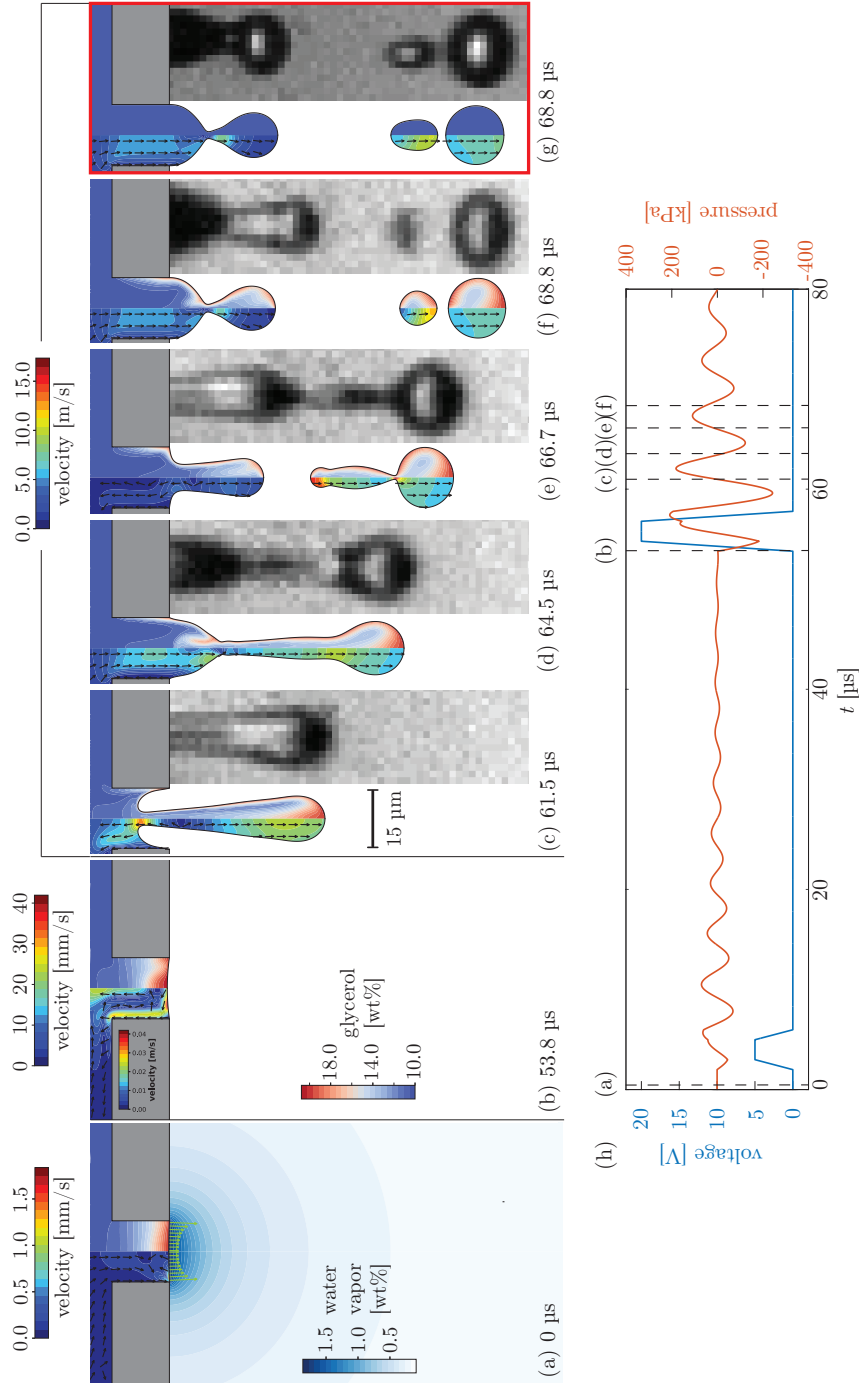


Figure 4.6: Snapshots from numerics and the corresponding experiment for the droplet formation process with a drying time of 100 ms (Movie available online). The numerical simulations provide two color schemes inside the liquid: the left hand side shows the velocity profile while the right hand side shows the glycerol concentration. The water evaporation rate is around  $100 \text{ g}/(\text{m}^2\text{s})$ . Snapshots (a) and (b) show the nozzle before droplet formation, and (c)-(f) show the droplet formation process. (g) Snapshot at same time as (f) but for the case of 1.5 ms drying time. (h) Demonstrates the actuation pulses (blue) and numerical pressure signal in the ink chamber (red), where the time instants of the snapshots are also indicated.

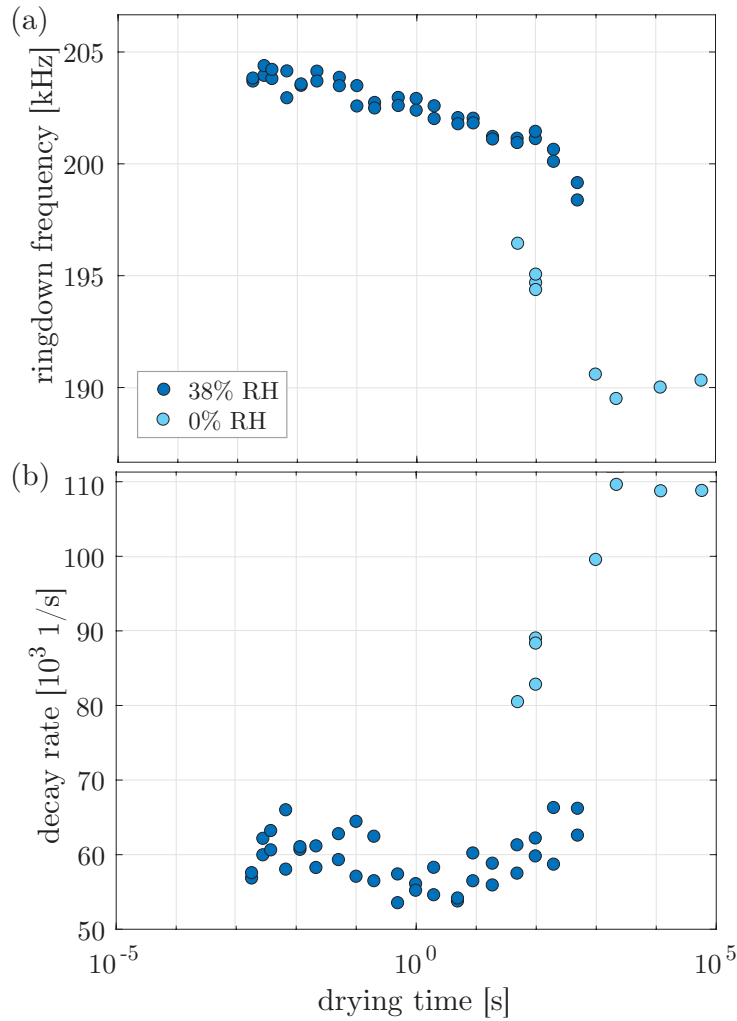


Figure 4.7: Experimentally measured (a) ringdown frequency and (b) decay rate of the ringdown signal of the probe pulse for different drying times at 38 % relative humidity (RH) and 0 % relative humidity (RH).

together with all the experimental results from Fig. 4.7. The experimental results for a humidity of 0% are indicated by the arrows at A. It can be observed that the decrease in ringdown frequency and increase in decay rate are a result of the increasing glycerol concentration in the nozzle, and that there is a match between the trends of the experiment and the analytical model. Note that the analytical model describes a homogeneous glycerol concentration in the nozzle, while the experiments are expected to contain a gradient in concentration. The arrow at B shows the result for a closed nozzle exit (obtained by manually blocking the nozzle exit). This provides a ringdown frequency and decay rate at the other end of the curve, that also matches

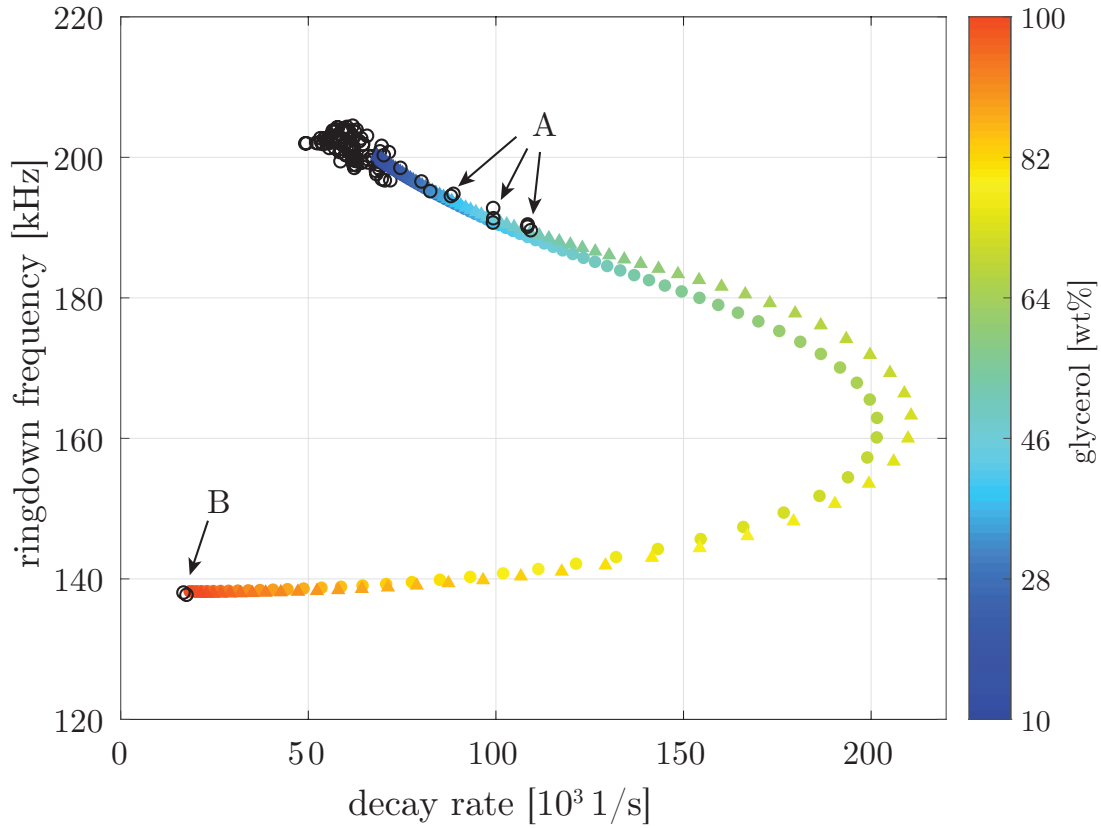


Figure 4.8: Ringdown frequency and decay rate obtained from experiments (open o), analytical model (filled o), and numerical simulations ( $\Delta$ ). The colorbar indicates the glycerol concentration inside the nozzle for the analytical and numerical model. The arrows at A point towards the experimental results obtained at 0% relative humidity. The arrow at B points toward the results from the manually closed nozzle.

very well with the model. The data in Fig. 4.7 can be physically explained by describing the printhead as a mass-spring-mass and damper system, with the two moving masses representing the restrictor and the nozzle as they have the highest acoustic inertance. The amplitude of the motion of the mass that represents the nozzle decreases with increasing glycerol concentration due to increased density and viscosity. The point where the glycerol concentration is at its maximum (see Fig. 4.8) is the location where the mass of the nozzle does not move anymore, decoupling it from the acoustics inside the printhead and thus effectively rendering a closed nozzle, which is exactly what happens when the nozzle is manually closed off. The good agreement between the analytical model and the experimental measurements demonstrates that compositional

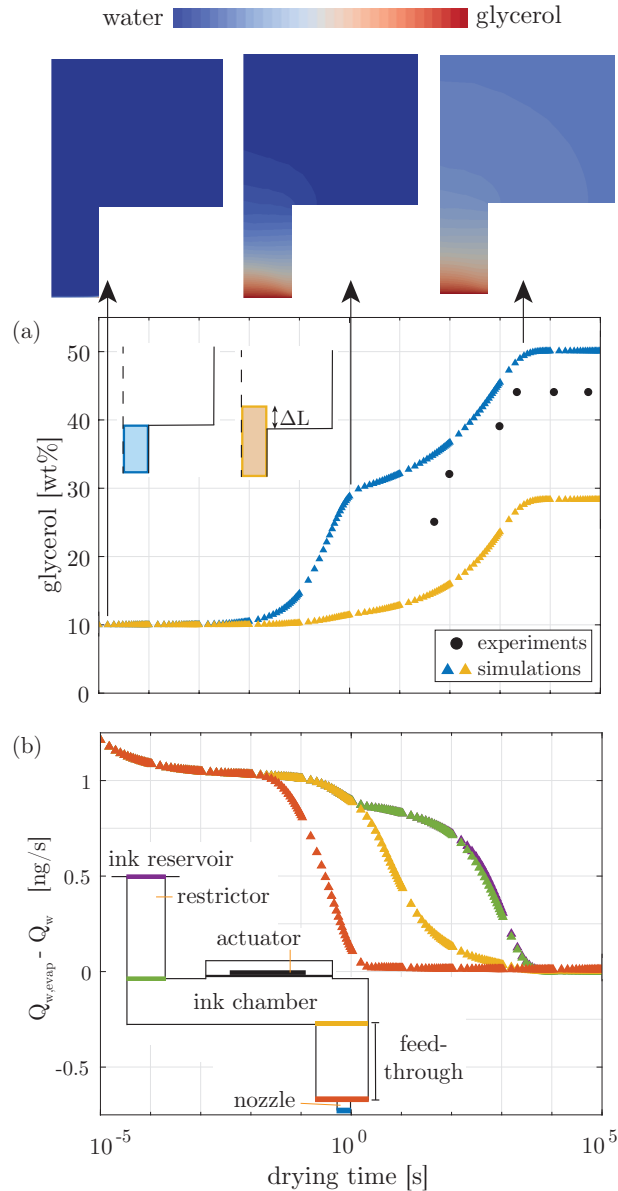


Figure 4.9: (a) Evolution of the glycerol concentration in the nozzle during drying time. The numerical results ( $\triangle$ ) show the average glycerol concentration for two different nozzle lengths: the geometrical length of the nozzle (blue); and an effective nozzle length (yellow). The experimental ringdown frequency and decay rate are converted to a glycerol concentration in the nozzle using the analytical model (o). The numerical snapshots above the figure show the glycerol concentration in the nozzle and the feedthrough at the indicated drying times. (b) Results from the numerical simulations showing the difference between the flow rates of water out of the nozzle (through evaporation  $Q_{w,evap}$ ) and through the boundaries between the other regions (through advection and diffusion  $Q_w$ ). The different colors indicate the region boundaries as illustrated in the inset.

changes of the ink in the nozzle can be acoustically measured.

Next, the plateau that is observed in both the ringdown frequency and the decay rate after a drying time of 2000 s is investigated. The analytical model indicates that the average concentration in the nozzle is 44 wt% glycerol. The numerical model described in section 4.4 is employed to further investigate this. To validate the numerical model, the ringdown frequency and decay rate that are obtained from increasing a homogeneous glycerol concentration in the nozzle in the simulations are also included in Fig. 4.8 (triangular markers). It can be seen that the numerical data agrees well with those from the analytical model. The simulations especially agree well with the experimental datapoints, which is the region of interest. The small deviation between the analytical and numerical models at high decay rates is expected to originate from the nozzle length that is not corrected for viscous friction in the analytical model, but only for its inertia [157].

The plateau is now investigated by simulating the evaporation process at 0 %RH and extracting the glycerol concentration in the nozzle by taking the average value in the nozzle. Figure 4.9a presents two curves for the numerically obtained average glycerol concentration in the nozzle: one where the average concentration is taken from the geometrical area of the nozzle (blue) and one where the area is extended into the feedthrough by the length  $\Delta L$  to account for the inertia of the flow (yellow datapoints, see section 4.3). Furthermore, a kink is visible in both numerical curves, at  $\sim 1$  s. As shown in the snapshots in Fig. 4.9a, the kink appears when the concentration gradient reaches the feedthrough. To explain: the diffusion in the nozzle can be approximated as one dimensional as long as the concentration gradient extends upward into the nozzle. When the concentration gradient reaches the feedthrough, the channel widens and therefore the diffusion becomes three dimensional (upward and sideways). This effectively creates a larger reservoir of water to diffuse into the nozzle, thereby resulting in a decreased rate at which the concentration of glycerol in the nozzle is increasing. After some time, the concentration gradient in the feedthrough reaches the channel walls, and the diffusion becomes steady and one-dimensional again. The time of the kink can be approximated by the mass transfer timescale for the water/glycerol mixture to travel the length of the nozzle in a solution of 10 wt% glycerol:  $\tau_n \approx L_n^2/D = (15 \mu\text{m})^2/0.6 \times 10^{-9} \text{ m}^2/\text{s} = 0.4 \text{ s}$ . These results show that the experimentally observed plateau in glycerol concentration after long drying

times ( $>2000$  s) is also obtained from the numerical simulations.

To also include the experimental results in Fig. 4.9a, the glycerol concentration in the nozzle is estimated from the experimentally measured ringdown frequency and decay rate using our analytical model. Both experiments and numerical simulations show an initial increase in glycerol concentration in the nozzle, eventually reaching a plateau after the same drying time. This indicates that the mass of water lost via evaporation at the nozzle exit is replenished through the transport of water upstream of the nozzle at the same rate, resulting in a steady state. This picture is confirmed by extracting the difference in flow rate of water between evaporation out of the nozzle  $Q_{w, \text{evap}}$  and transport through the different regions in the printhead  $Q_w$ , see Fig. 4.9b. Initially, the water loss due to evaporation is faster than the water replenishment from the reservoir. As the local concentration of glycerol gradually increases, the water evaporation rate decreases, and so does the transport of water inside the printhead. At the moment the plateau is reached, the transport of water through each region is the same as the rate of evaporation. With the same approach for the kink at  $\sim 1$  s, the timescale can be estimated for when the concentration gradient has passed through the system:  $\tau_s \approx L_{\text{total}}^2/D = (1.2 \text{ mm})^2/0.6 \times 10^{-9} \text{ m}^2/\text{s} = 2400 \text{ s}$ . This suggests the observed plateau occurs as soon as the concentration gradient reaches the ink reservoir and again demonstrates that the observed plateau in glycerol concentration is the result of a steady state of the water flux through the system.

### 4.5.3 Recovering the liquid composition

Until now, the focus has been on the change in the liquid composition during the drying period. However, for all practical purposes, in the inkjet printer it is important to get back to the initial liquid composition to recover the well-controlled drop formation. Therefore, we now investigate the number of droplet formation events required to achieve the initial (pre-drying) liquid composition after a certain period of drying. To do so, the ringdown signals of the probe pulses of the first 1000 droplets after different drying times were measured. Figure 4.10a displays the resonance frequency for the different drop numbers for different drying times. The lowest horizontal row shows the frequencies before the first droplets after the drying time, and is the same as the frequencies in Fig. 4.7a for 38 %RH. At short drying times there is no variation in resonance frequency with drop number. With increasing drying time, more droplet formation events are required to return to the resonance



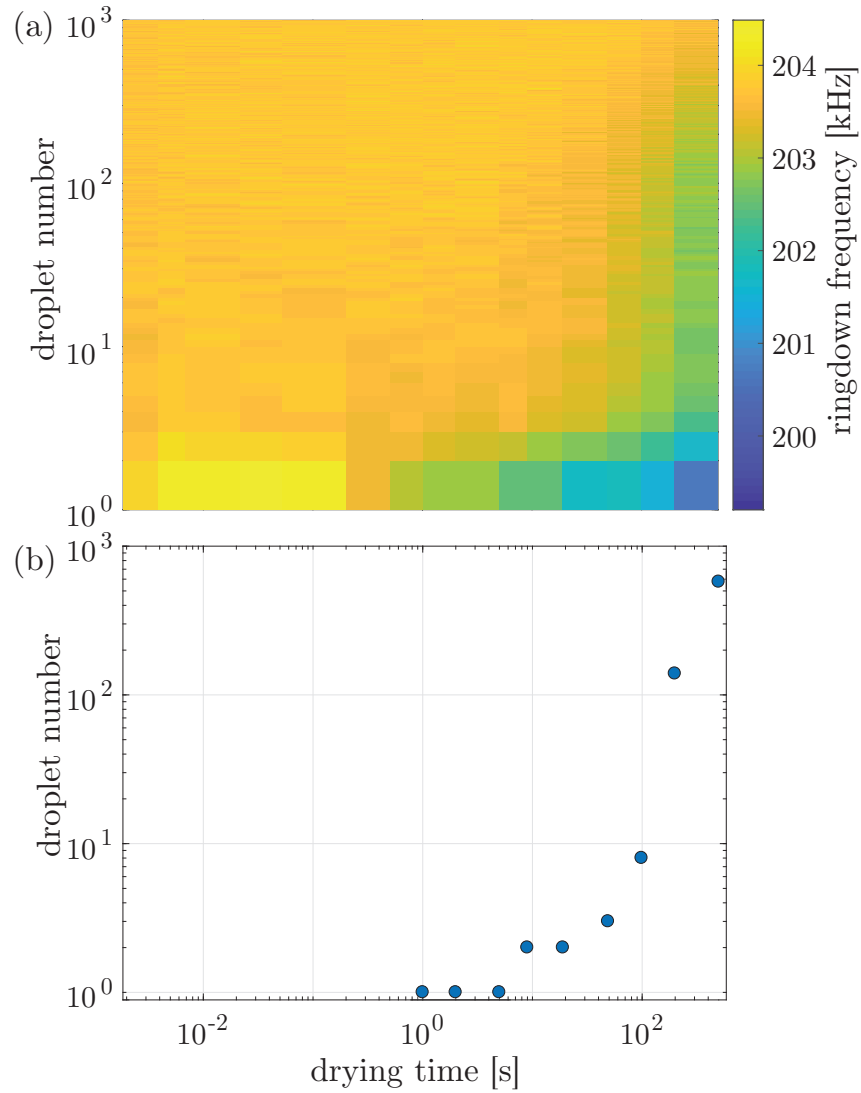


Figure 4.10: (a) The resonance frequency of the ringdown signal for the first 1000 droplets that form after different drying times. (b) The number of droplets that have to be jetted before the resonance frequency is back to within 0.5% of the resonance frequency without drying.

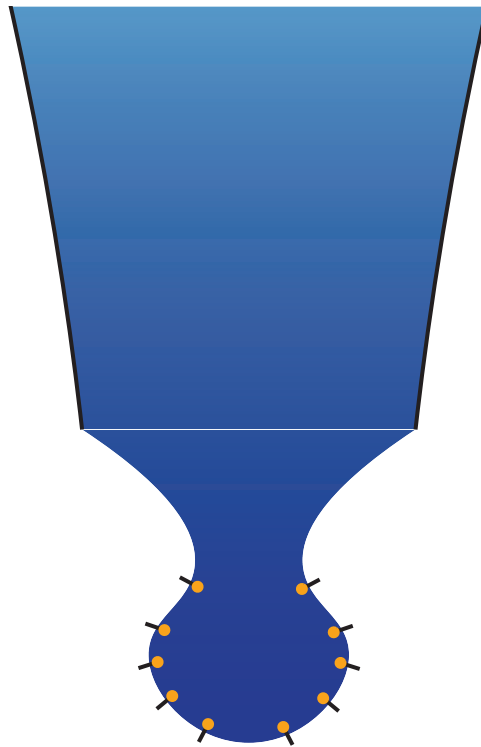
frequency of the shorter drying times. This is evident from Fig. 4.10b, which shows the number of droplet formations required for the resonance frequency to return to within 0.5% of the original resonance frequency. As can be observed from Fig. 4.10b, the number of droplets required for the recovery increases more than exponentially with drying time. This can be the result of the concentration gradient in the liquid extending beyond the nozzle region for long drying times, where the flow is more complex during the jetting process, containing stagnant fluid and a vortex as shown in [17].

## 4.6 Conclusion & outlook

In drop-on-demand inkjet printing there can be loss in control over the print quality due to intermittent periods of no jetting during the printing process. During these idle periods, the nozzle can dry out and a multicomponent ink (in this case, a mixture of water and glycerol) can change in composition at the nozzle exit because of selective evaporation. By measuring the ringdown signal of the ink channel acoustics in response to a probe pulse, the change in ringdown frequency and decay rate are measured for different drying times. An analytical model is proposed, which enables the calculation of the glycerol concentration in the nozzle from the experimentally-measured ringdown frequency and decay rate. It was also observed that after an extended drying time, an equilibrium is reached between the amount of water lost at the nozzle exit through evaporation and the amount of water transported from the bulk to the nozzle exit via advection and diffusion. The result is a liquid composition that does not change with drying time anymore. Finally, the amount of jetted droplets required to recover from the drying process is observed to increase stronger than exponentially with drying time.

Being able to probe the local concentration of a multi-component mixture at the nozzle exit allows for the investigation of more complex problems, such as the influence of a variety of components typically used to control sessile droplet evaporation in inks, including particles and surfactant. Thus, the results presented here allow for a better understanding of the requirements to control the printing process, to non-invasively measure the change of concentration during evaporation, and to measure the effectiveness of mitigation strategies such as fluid mixing (non-jetting) pulses during drying periods, which we have observed to influence the concentration profile.

## Role of surfactants on droplet formation in DoD piezoacoustic inkjet printing



□

---

In preparation as: **Maaïke Rump**, Christian Didden, Uddalok Sen, Michel Versluis, Detlef Lohse, and Tim Segers, *Role of surfactants on droplet formation in DoD piezoacoustic inkjet printing*

## Abstract

In piezo acoustic drop-on-demand inkjet printing a single droplet is produced for each piezo driving pulse. Selective evaporation is inherent to inkjet printing as inks are typically multicomponent and include surfactants. Here, we study the influence of surfactants on droplet formation in piezo-acoustic inkjet printing while we vary the time between the formation of two successive droplets over 5 orders of magnitude, i.e., from microseconds to minutes. During jetting, a large amount of new surface area is created when the liquid is ejected from the nozzle. Jetting occurs on a microsecond timescale, which is shorter than the typical timescale of surfactant adsorption. Here, we vary the time between the ejection of two droplets to allow surfactants to accumulate on the meniscus. At a waiting time of milliseconds to one second, we observe a change in break-up dynamics, but no effect on the droplet velocity and volume. When the waiting time is longer than one second, when evaporation starts to play a role, the droplet velocity and volume increases. We measured the surface tension of the ejected droplets from their dynamics in flight, which showed that the increased local concentration of surfactant due to evaporation allows for faster surfactant adsorption on the freshly formed surface. Interestingly, increasing the bulk concentration of surfactant does not lead to an increase in droplet velocity, as viscosity starts to play a role as well. Thus, the increased local concentration of surfactant due to evaporation is required to increase the droplet velocity. Numerical simulations demonstrate that the increased concentration at the nozzle exit covers the droplet during the droplet formation process, thereby allowing for surfactant adsorption along the freshly formed surface.

## 5.1 Introduction

Drop-on-demand inkjet printing is a method that provides accurate and highly reproducible picoliter deposition of liquids which does not require substrate contact [1-4]. A wide range of liquids with different physical properties can be jetted, which has resulted in many different applications of inkjet printing beyond printing graphics on paper, such as the fabrication of electroluminescent displays [6,7], the printing of electronic circuits [8-10], and bioprinting in the life sciences [11-13].

Inks in inkjet printing generally contain surfactants to control the spreading

and drying behavior of the droplet on the paper [27]. They lower the surface tension [158] and thereby increase the spreading of the droplet [159,160] as well as compete with the coffee stain-effect [122,161,162] with the goal to provide a homogeneous distribution of the pigment particles [151]. However, before the ink reaches the paper it is jetted from the nozzle, where the surfactants are also present. That leads to the question: Is there an influence of surfactants on droplet formation in inkjet printing?

During droplet formation, a fresh surface is generated at the microsecond timescale. A decrease in surface tension through surfactant adsorption is understood to be a process that is typically at least 3 orders of magnitude smaller than the timescale of the jetting process [163]. Surfactant adsorption is a dynamic process, leading to a dynamic surface tension, where the dynamic surface tension decreases until the maximum surfactant packing density is reached corresponding to the equilibrium surface tension. The equilibrium surface tension decreases further with an increase in bulk concentration until the critical micelle concentration (CMC) is reached. A further increase in surfactant concentration leads to expulsion of the surfactants through the formation of surfactant vesicles, or micelles. The adsorption rate, CMC, and equilibrium surface tension all depend the molecular size of the surfactant molecule, whether or not it is charged, and on its interaction potential with the solvent [161]. Numerous surfactants are available which further complicates a universal understanding of how surfactants control microscale fluid flow [158].

In inkjet printing, multiple timescales are involved, as illustrated in Fig. 5.1. The shortest timescale (left) is during droplet formation, followed by the time in between droplet formations (middle), which can extend to timescales where evaporation starts to play a role (right). The sub-millisecond timescale of droplet formation is generally considered to be too fast for adsorption of surfactant onto the newly formed liquid surface. Therefore, a non-homogeneous distribution of surfactant is expected, resulting in a gradient of surface tension [164]. The difference in surface tension along the interface can result in Marangoni flows, which have been shown to delay the thinning rate of a surfactant covered liquid column, and subsequently delay the break-up of the liquid column [164–171]. Antonolopoulo *et al.* [164] observed that the surfactants remain at the front of the liquid column, and that therefore the pinch-off from the nozzle is not influenced by the presence of surfactants, but only the break-

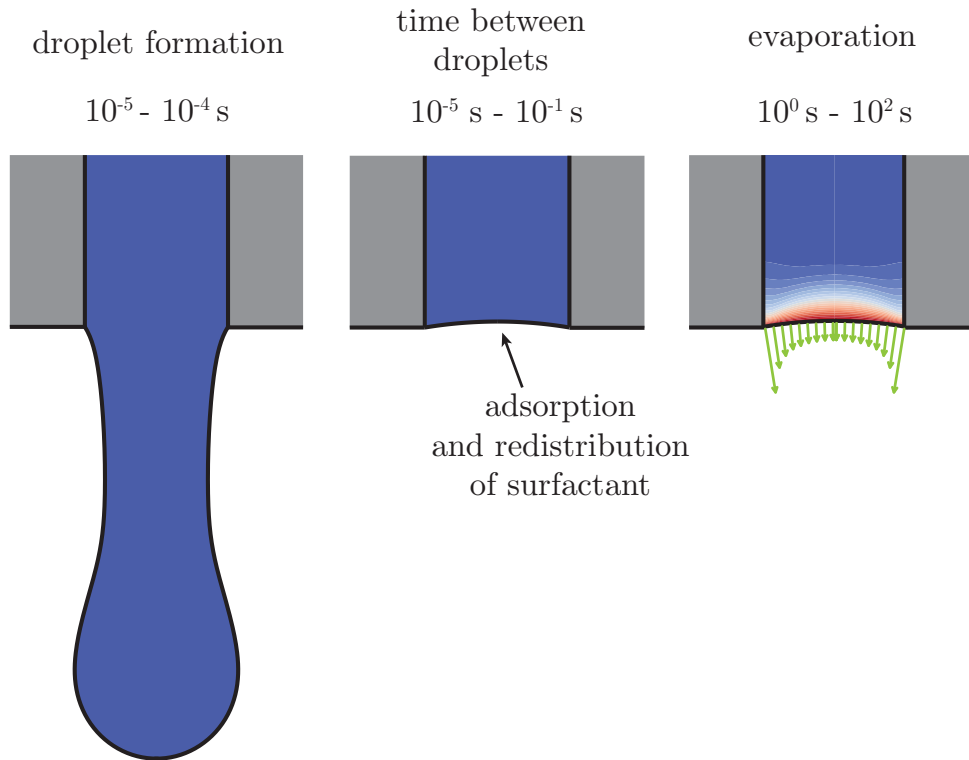


Figure 5.1: Timescales present at the nozzle exit in between droplet formation, during droplet formation, and in between printing processes.

up of the liquid tail into smaller droplets. Furthermore, only recently, studies have tried to incorporate the influence of surface rheology on the thinning of the liquid jet [172][173].

The time in between droplet ejection dictates the timescales during which we expect the surfactant adsorption to occur that in the end determines the surfactant concentration at the surface during droplet formation [164]. What should be considered is that after a droplet has been produced, the oscillates and requires some time to come to a static position. The liquid motion can increase the adsorption rate of the surfactants onto the surface. Here, we vary the time in between droplet ejections, or waiting time. It is expected that a lower surface tension of the meniscus leads to a faster ejection speed of the liquid during droplet formation, as less energy is required to form new surface area. Therefore, our focus here is on the expected change in droplet velocity and its corresponding volume while varying the waiting time.

When the timescale between droplets is increased, evaporation takes place,

which can locally increase the surfactant concentration at the nozzle exit. To the best of our knowledge, the influence of selective evaporation induced surfactant concentration gradients on droplet formation has not been investigated. Earlier studies in oil recovery suggest that a higher concentration does not increase the adsorption rate of the surfactant onto solids [174]. To confirm whether the same holds for liquid-air interfaces, we extend the waiting times as far as to timescales where evaporation occurs.

After the ejected liquid has pinched off from the liquid in the nozzle, often followed by another break-up of the trailing liquid jet, the formed droplets oscillate. The effective surface tension and viscosity can be extracted from the droplet oscillation frequency and damping [175–178]. Measuring the surface tension of the oscillating droplet on sub-millisecond timescale then provides the surface tension of the liquid during the droplet formation, giving direct insight in the surfactant concentration on the surface.

In the present work, we investigate the effects of surfactants on droplet formation and pinch-off from the nozzle in drop-on-demand inkjet printing. We utilize the measurement of the velocity and volume of the jetted liquid, the pinch-off time, and the surface tension of the formed droplets to investigate the influence of surfactants on drop formation, and its local distribution at the nozzle exit. We further employ numerical simulations in which we include evaporation effects to understand the experimental jetting observations. This work is organized as follows: in section 5.2, we describe the experimental procedure, while in section 5.3 we present the numerical method. Section 5.4 contains the results and discussion, and section 5.5 ends the work with conclusions and an outlook.

## 5.2 Experimental methods

### 5.2.1 Printhead and ink

Autodrop Pipettes (nozzle diameter: 70  $\mu\text{m}$  and 50  $\mu\text{m}$ ) from Microdrop Technologies GmbH (AD-K-501 and AD-H-501) were used as printheads in the present experiments. More details about this type of printhead can be found in Refs. [60, 61]. The printhead is set to drive the meniscus in a push-pull motion, thereby first ejecting the liquid and then retracting the meniscus, which leads to pinch-off.



Two different surfactants are used: the non-ionic gemini Dynol 607 (Air Products, 342 g/mol) and the more commonly used non-ionic Triton X-100 (Sigma-Aldrich, 647 g/mol). The CMCs of these aqueous solutions are  $2.92 \text{ mol/m}^3$  (0.1 wt%), see appendix Fig. 5.10, and  $0.22 \text{ mol/m}^3$  (0.014 wt%) [179], respectively. Dynol being a gemini surfactant entails that it has multiple hydrophilic heads and multiple hydrophobic tails, linked by spacers. The close packing of the hydrophobic tails results in gemini surfactants requiring less molecules to be present on the surface to reduce the surface tension compared to conventional surfactants [180]. Looking at the dynamic surface properties, after 50 ms Dynol has reduced the surface tension of water to  $40 \text{ mN/m}$  (see appendix Fig. 5.12) while Triton has only reduced the surface tension to  $60 \text{ mN/m}$  [181]. The surfactant solutions are supplied from a pressure controlled container set to a constant underpressure of 8 mbar to prevent the liquid from dripping out of the nozzle due to gravity.

## 5.2.2 Imaging setups

Two different setups have been used to perform the measurements. One setup uses stroboscopic imaging (see Fig. 5.2a), where the nozzle is illuminated by incoherent 8 ns pulses, from a laser-induced fluorescence (iLIF) system [43]. The iLIF system consists of a pulsed laser (Quintel EverGreen, dual cavity Nd:YAG,  $\lambda = 532 \text{ nm}$ , 7 ns), a fluorescent plate embedded in a highly efficient diffuser (Lavision, part nos. 1108417 and 1003144), and a lens to condense the light pulses onto the imaging plane of the microscope. The microscope (BX-FM Olympus) has a  $5\times$  objective (LMPLFLN  $5\times$ , numerical aperture of 0.13), a tube lens (U-TLU), and a high-resolution CCD camera (Lumenera, Lw135m,  $1392 \times 1040$  pixels,  $4.65 \mu\text{m}/\text{pixel}$  size). The resulting optical resolution is  $0.93 \mu\text{m}/\text{pixel}$ . The images captured by the camera were saved by in-house custom-made software on a personal computer, programmed in the graphical programming language LABVIEW (National Instruments).

A second setup (Fig. 5.2b) uses back-illumination by a fiber-optic light source (LS-M352, Sumita) and a high-speed camera (Shimadzu HPV-X2,  $10^6$  frames per second,  $400 \times 250$  pixels,  $32 \mu\text{m}/\text{pixel}$ ) to record the droplet formation process. The same  $5\times$  objective is used as well as a  $10\times$  objective (LMPLFLN  $10\times$ , numerical aperture of 0.25). The resulting imaging resolutions are  $6.64 \mu\text{m}/\text{pixel}$  and  $3.71 \mu\text{m}/\text{pixel}$ , respectively.

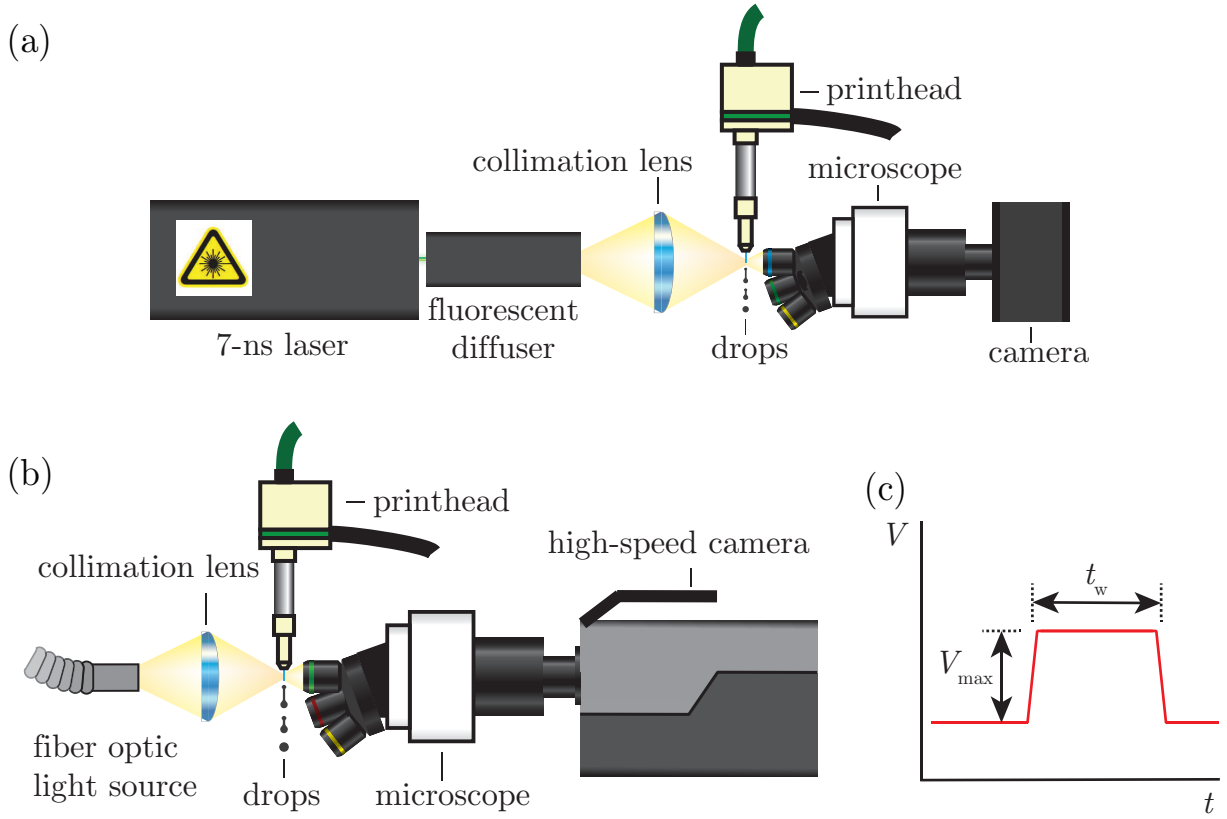


Figure 5.2: Schematic of the stroboscopic setup in (a) and the high-speed camera setup in (b). The pulse shape is sketched in (c), where  $V_{max}$  is the pulse amplitude, and  $t_w$  is the pulse width.

In both setups, the experiments start by jetting 999 droplets at a DoD frequency of 1 kHz to make sure the liquid mixture in the nozzle has the same composition as in the bulk. Then, the jetting was stopped for the predetermined time, which is the variable in the experiments. When the desired time had passed, the piezo was driven to produce a single droplet. The driving voltage of the piezo ( $V_{max}$ ) as well as the pulse width ( $t_w$ ) were varied to control the amount of liquid jetted from the nozzle (see Fig. 5.2c).

### 5.2.3 Image analysis

The acquired images were analyzed in MATLAB. First, the position and velocity of the liquid coming out of the nozzle were extracted by tracing the front of the ejected liquid along the direction of jetting, followed by a moving average smoothing and then taking the derivative of this smoothed position data. As soon as the liquid pinches from the nozzle, this time with respect to

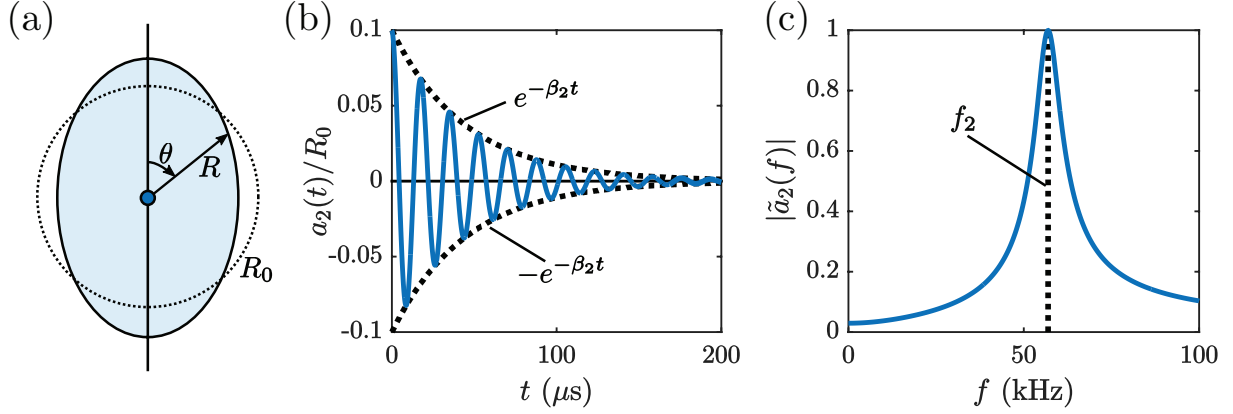


Figure 5.3: (a) Schematic showing the droplet during oscillation is symmetrical around the vertical axis. Indicated in the dotted line is the equilibrium droplet radius. (b) The amplitude versus time for the shape oscillation of mode  $n = 2$ . The damping rate is determined from the decay in amplitude. (c) The frequency of the shape oscillations is determined by the corresponding Fourier spectrum of the amplitude over time. This figure is adapted from [175].

the time of actuation of the piezo, is documented as the pinch-off time. The error in the pinch-off time is set to the interframe time of the experiment. Now the liquid is free from the nozzle and forms one or multiple droplets. Consecutively, the droplets were in the field of view for at least another 50  $\mu\text{s}$ . By recording the droplet during this time, the mean radius and its standard deviation were calculated from the series of datapoints. The linear fit to the position data and the fitting error provides the velocity of the droplet and its error margin, respectively. As the total volume of liquid jetted out of the nozzle was not constant, we quantified the sum of all droplet velocities and their mass, resulting in the momentum. Dividing the momentum by the total mass gives a mass-averaged velocity.

Finally, the frequency of the oscillating droplet was extract to calculate the surface tension. This method [175–178] is based on Rayleigh’s expression for the shape of an axisymmetrically deformed droplet as a sum of Legendre polynomials  $P_n$  [182]:

$$R(\theta, t) = \sum_{n=0}^{\infty} a_n(t) P_n(\cos(\theta)), \quad (5.1)$$

where  $\theta$  is the polar angle and  $a_n(t)$  is the time-dependent surface mode coefficient for different mode numbers  $n$ . Assuming an incompressible liquid, no

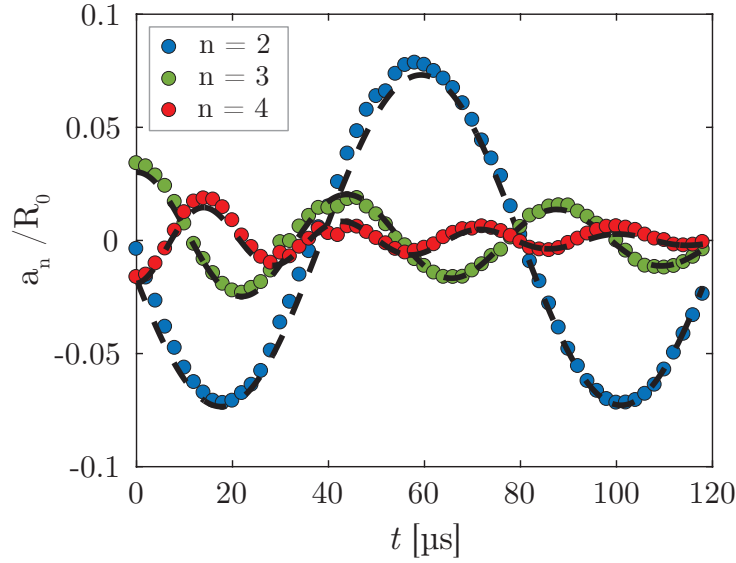


Figure 5.4: The oscillation modes  $n = 2$  (blue markers),  $n = 3$  (green markers), and  $n = 4$  (red markers) for 1 CMC Dynol during 1 kHz jetting. The surface tension  $\gamma$  is calculated from the best fit of Eq. 5.3 (dashed lines).

evaporation and no internal rotation,  $a_0(t) = R_0$ , where  $R_0$  is the radius of the undisturbed sphere (see Fig. 5.3a). By placing the coordinate system at the drop's center of mass, the next mode becomes zero as otherwise the droplet would change in volume ( $a_1(t) = 0$ ). Thereby, Eq. 5.1 simplifies to:

$$R(\theta, t) = R_0 + \sum_{n=2}^{\infty} a_n(t) P_n(\cos(\theta)). \quad (5.2)$$

The modal coefficients can be written as damped oscillations:

$$a_n(t) \sim e^{-\beta_n t} \cos(\sqrt{(\omega_n^2 - \beta_n^2)t}), \quad (5.3)$$

where  $\beta_n$  is the damping rate and  $\omega_n$  the angular frequency for each mode  $n$ . The extraction of the damping rate and eigenfrequency using Eq. 5.3 is demonstrated in Fig. 5.3b and c, respectively. The eigenfrequency can be related to the surface tension by:

$$\omega_n^2 = (2\pi f_n)^2 = n(n-1)(n+2) \frac{\gamma}{\rho R_0^3}, \quad (5.4)$$

where  $f_n$  is the eigenfrequency,  $\gamma$  is the surface tension, and  $\rho$  is the density. The bulk viscosity  $\mu$  can also be extracted from the damping rate of the droplet

oscillations:

$$\beta_n = (n - 1)(2n + 1) \frac{\mu}{\rho R_0^2}. \quad (5.5)$$

The influence of surface viscosity is not taken into account in this model. From the experimental measurements, the modes  $n = 2$  till  $n = 4$  are extracted, as is shown in Fig. 5.4.

### 5.2.4 Viscosity measurement

The bulk viscosities of aqueous Triton mixtures of concentrations above 1 CMC are measured by a capillary viscometer [183]. We push the solution through a 2.3 cm long and 150  $\mu\text{m}$  diameter capillary tube with a pressure of 1.5 bar. The viscosity can be calculated using the Hagen-Poiseuille equation:

$$\mu = \frac{\Delta P \pi r^4}{8 L Q}, \quad (5.6)$$

where  $\Delta P$  is the pressure drop across the length of the tube,  $r$  is the radius of the tube,  $L$  is the length of the tube, and  $Q$  is the flow rate through the tube. The flow rate is determined by weighing the amount of fluid that has passed through the tube in 60 s, and then dividing it by the density  $\rho$ .

## 5.3 Numerical model

We model the drying process to gain insight in the local distribution of Triton in the nozzle and during the droplet formation process, which cannot be obtained from experiments owing to the very short timescale of jetting. We limit ourselves to the local distribution of Triton instead of its adsorption kinematics, as incorporating surfactant material properties requires knowledge about adsorption and desorption rates for Triton concentrations exceeding the CMC value, which are, to the best of our knowledge, unknown at present.

Simulating the entire process, i.e. the preferential evaporation of water from the nozzle followed by a jetting event, is a challenging problem, which we have addressed in chapter 4. Therefore, we refer to this chapter for details and in the following section we describe the changes that were required while using a different printhead.

### 5.3.1 Evaporation phase

During the evaporation phase, the fluid dynamical equations in both the gas and the liquid phase are solved and all parts related to the droplet formation are deactivated. The employed governing equations for solving the evaporation are the same as in chapter 4 and also resemble the equations successfully used in the evaporation of multi-component droplets on substrates, e.g. in [151].

Specific to this work and the liquid mixture of Triton-water, is the unknown activity coefficient and is therefore set to 1. Therefore, no non-ideality of the mixture within Raoult's law is taken into account during the evaporation process. Furthermore, the composition-dependent properties  $\rho(w)$  and  $\mu(w)$  are described as linearly dependent on the composition, where  $w$  is the concentration of water (mass fraction) in the liquid. The surface tension  $\sigma(w)$  is described as the function  $A - B/(1 + C(1 - w)^2)$ , where the coefficients are set  $A = 33$ ,  $B = -39.5$ , and  $C = 36 \times 10^6$ . The result is a curve that reaches the CMC concentration with a surface tension is 37 mN/m, from which it slowly decreases to the value of 33 mN/m. The diffusivity  $D$  is fixed at a value of  $8 \times 10^{-11} \text{ m}^2/\text{s}$  [184]. Finally, similar to previous work, a constant underpressure of 8 mbar is applied as in the experiments, which results in a slightly inwardly curved meniscus.

### 5.3.2 Droplet formation

During the droplet formation process, evaporation is not taken into account as the time scales are several orders of magnitude smaller than during the evaporation phase. Furthermore, the droplet's friction with the gas phase is not entirely negligible, but the influence on drop formation is. This has been shown by the excellent agreement between experiments and frictionless numerics in slender jet approximation [94].

The acoustics are unknown for the printhead used in this work. Therefore, the pulse shape and amplitude is estimated to produce a similar droplet velocity and shape as in the experiments. These parameters are used in the model by setting a normal traction at the top of the nozzle:

$$\mathbf{n} \cdot \mathbf{T} \cdot \mathbf{n} = -\alpha V_{pulse}(t), \quad (5.7)$$

where  $\mathbf{n}$  is the normal,  $\mathbf{T}$  is the stress tensor ( $\mathbf{T} = -p\mathbf{1} + \mu(\nabla\mathbf{u} + (\nabla\mathbf{u})^t)$ ),  $V_{pulse}(t)$  is the pulse shape and amplitude, and  $\alpha$  is the pulse to pressure conversion factor, which is set to 400 Pa/V.

## 5.4 Results & discussion

### 5.4.1 Droplet velocity

We start our investigation on the role of surfactants on droplet formation at a typical timescale for Dynol surfactant adsorption (100 ms). Figure 5.5 compares the droplet formation process for pure water and that of an aqueous 1 CMC Dynol solution. We increased the piezo driving amplitude from 95 V to 125 V in steps of 10 V to increase the ratio of freshly formed liquid-gas interface to the surface area of the static meniscus at the nozzle exit before the jetting starts. The waiting time was 100 ms in both cases, i.e., the time between the 999 jetted droplets at a DoD frequency of 1 kHz and the droplet formation process that is shown in Fig. 5.5 was 100 ms. For the surfactant case, after 100 ms, the surface tension of the meniscus before the jetting starts is expected to be approximately 34 mN/m (see Fig. 5.10 in the appendix). Note from the left column in Fig. 5.5 that the presence of surfactants changes the details of the break-up dynamics between the head droplet and its tail for all tail lengths (driving voltages) imaged here. The time until break-up of the head droplet from the tail is always longer when surfactants are present. Also note that the positions of the head droplet and the back end of the tail remain mostly unaffected by the presence of the surfactants. The break-up and subsequent filament contraction resulting in the final configuration of two droplets at a later moment in time (95 – 105 V) remains mostly unchanged by the surfactants, see right column of Fig. 5.5. Furthermore, the details of the break-up of the filament (115 - 125 V) change in a similar way for the head droplet - tail break-up. Thus, at the short waiting time of 100 ms, the Dynol surfactant influences the details of the break-up dynamics of the ejected liquid while it has almost no effect on the velocity and volume of the resulting droplets.

This observation corresponds with the work by Antonopoulou *et al.* [164]. Their numerical simulations further demonstrate that the surfactant is transported towards the back of the head droplet liquid during droplet formation by the surface velocity. At the moment of break-up between head droplet and tail, the surfactants are located near the pinch-off location. The gradient in surface tension induces Marangoni flow, which delays the break-up between the head droplet and tail, which is indeed what we observe.

We continue our investigation by also considering timescales longer than 100 ms.



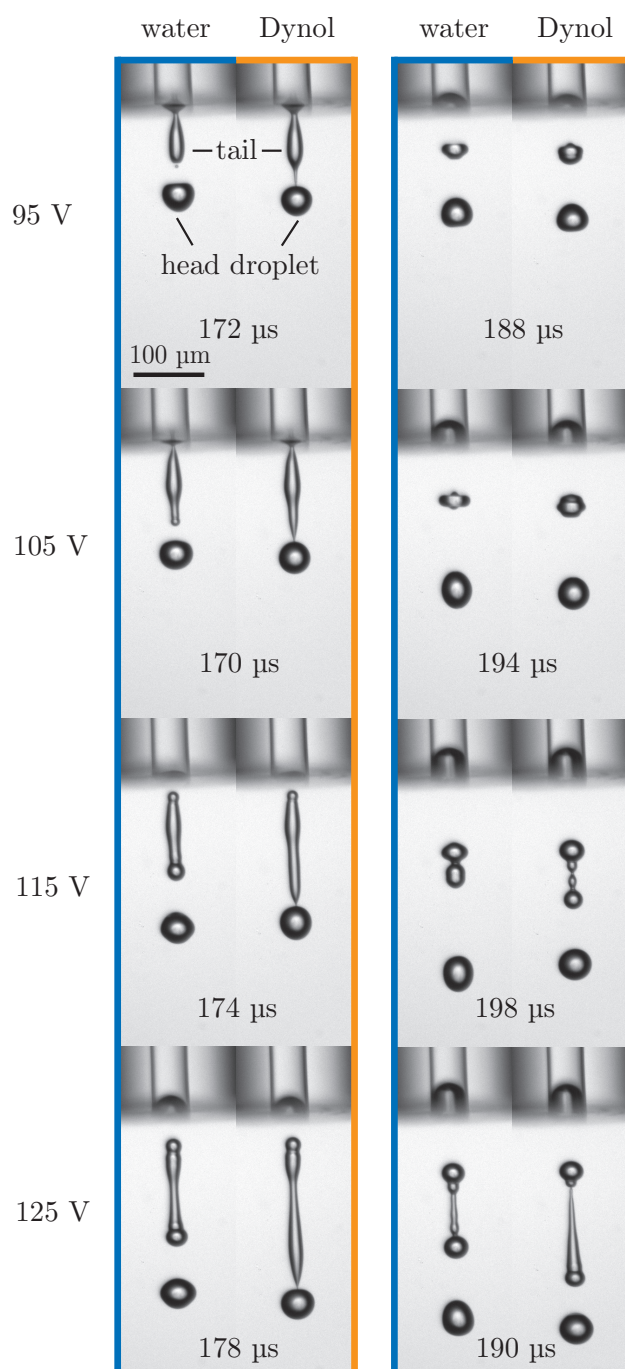


Figure 5.5: Droplet formation for water and an aqueous 1 CMC Dynol solution for different voltages and a waiting time of 100 ms. The left column compares the moment in time just before the break-up of the head droplet from the tail, while the right column compares a later moment in time.

For both the 1 CMC Dynol solution and pure water, the droplet velocity was measured as a function of the waiting time, which was varied over 5 orders of magnitude from milliseconds to minutes as shown in Fig. 5.6a. We attribute the minor difference in droplet velocity between pure water and the surfactant solution, as observed for waiting times shorter than 10 ms, to changes in wetting behavior of the surfactant solution at the nozzle exit. It was observed that at these waiting times, a surfactant solution was left on the nozzle plate from previous droplet formation, which decreased the velocity of the subsequent droplet (see appendix Fig. 5.11). This residual liquid disappeared for waiting times longer than 10 ms. More importantly, Fig. 5.6a shows that the droplet velocity increases monotonically with waiting time up to a 40% higher droplet velocity than that of pure water at a waiting time of 200 s. The droplet velocity of pure water remained relatively constant as the waiting time increased, i.e., it did not increase by more than 3%. Figure 5.6b shows that the total jetted volume of the surfactant-laden solution increased when the droplet velocity increased ( $t > 3$  s). The figure also shows that at waiting times longer than 3 s two droplets were formed, i.e., a head droplet and a satellite droplet. Therefore, we plot the sum of the momentum of both droplets in Fig. 5.6c. The total momentum was normalized by the total mass to obtain the mass-averaged velocity of the jetted liquid, which is plotted in Fig. 5.6a (red data points). The mass-averaged velocity is very similar to the velocity of the head droplet, i.e., the velocity of satellite droplet was very similar to that of the head droplet. Thus, at waiting times beyond 1 s, the kinetic energy of the jetted liquid increases dramatically with waiting time. The underlying question is: What governs this velocity increase and what are the timescales where it becomes apparent? Furthermore, what is the role of the surfactants on the observed velocity increase?

To find answers to these questions, we first measure the surface tension of the head droplet from its (damped) oscillation dynamics in free flight. Figure 5.6d demonstrates a correlation between the increase in droplet velocity and a decrease in surface tension. Remarkably, the surface tension of the head droplet decreases below that of pure water only at waiting times beyond 1 s, whereas Dynol is expected to be fully covering the meniscus interface (before the jetting starts) already at a 10 times shorter timescale (appendix Fig. 5.12). Another remarkable observation is that the surface tension of the head droplet plateaus at waiting times  $> 10$  s, whereas the droplet velocity keeps increasing. The questions from both these observations are: Why and how does the surface

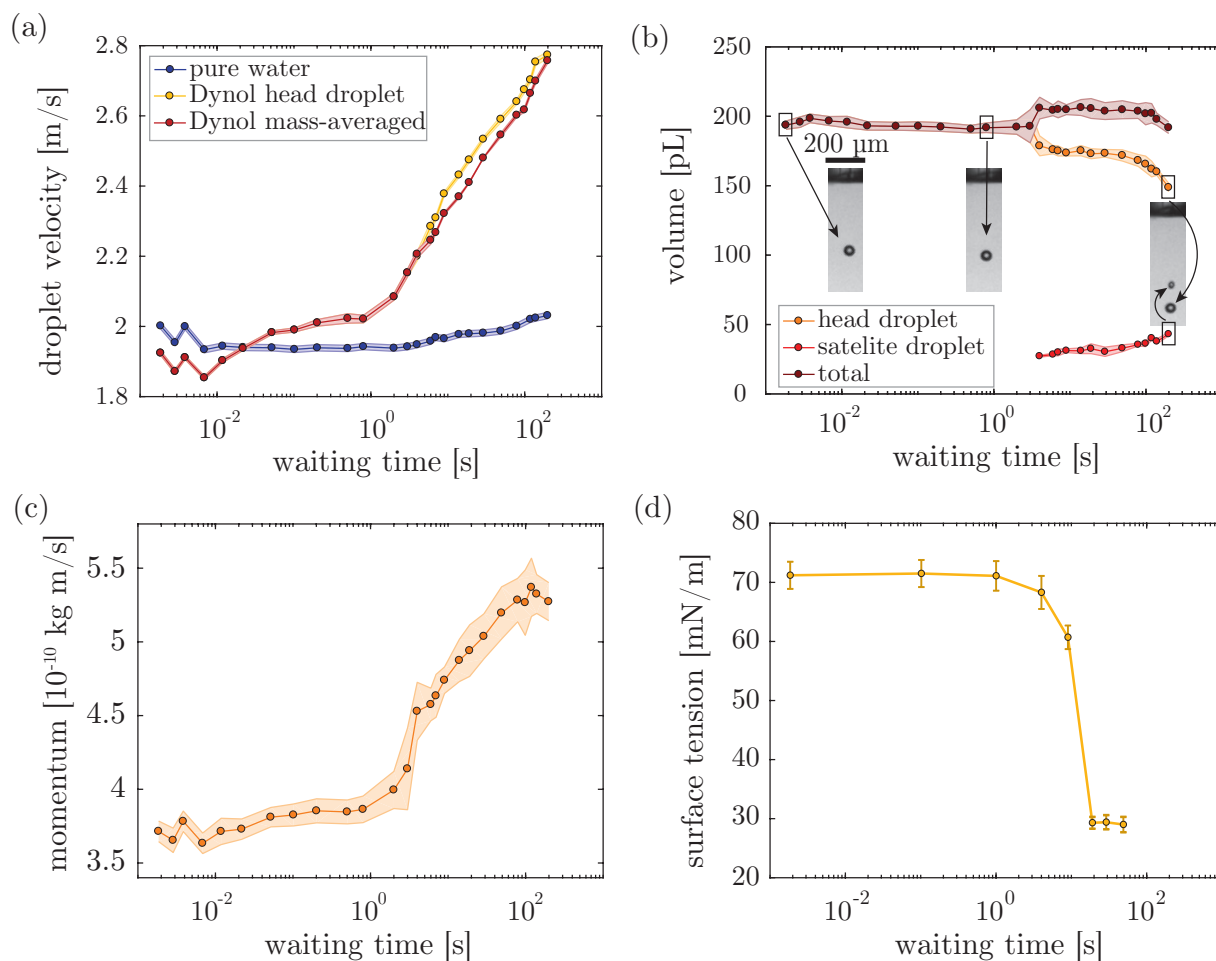


Figure 5.6: (a) Volume of the 1 CMC Dynol droplets and total volume ejected from a 50  $\mu$ m diameter nozzle as functions of waiting time. (b) Momentum of all the ejected liquid as function of waiting time. (c) Velocity of the pure water droplets and the Dynol head droplets compared to the Dynol mass-averaged velocity calculated from the momentum as function of waiting time. (d) Surface tension of the Dynol head droplets as function of the waiting time.

tension of the jetted liquid decrease for waiting times beyond 1 s?

### 5.4.2 Droplet formation

To investigate the time dependence of the ejection velocity in more detail, we first compare the droplet formations as measured for the 1 CMC Dynol solution at two waiting times in Figs. 5.7a and b, where (a) corresponds to a waiting time of 2 ms and (b) to a waiting time of 50 s. The most striking difference is the length of the tail. This is highlighted in Fig. 5.7c, which

shows that the increase in tail length is due to both the front of the liquid jet having traveled further (higher velocity) and the end of the tail that pinched off later in time. We plot the front position of the liquid jet vs. time in Fig. 5.7d for waiting times ranging from 2 ms up to 50 s. The velocity calculated from these position data is shown in Fig. 5.7e. Note that the velocity curves start to deviate with waiting time only after 50  $\mu$ s after the start of the piezo actuation pulse, i.e., when the meniscus starts to retract into the nozzle as shown by Figs. 5.7a and b. For waiting times longer than  $\sim 10$  s, the velocity of the liquid jet decreases less during the retraction of the meniscus. This observation indicates that the surface tension at the rear of the jet is decreased at longer waiting times thereby exerting a lower pulling-force on the liquid jet during meniscus retraction. The pinch-off time that is plotted in Fig. 5.7f once again shows that at waiting times longer than  $\sim 10$  s changes are observed in the droplet formation process. The increase in pinch-off time can be caused by a decreased surface tension but also by an increased surface viscosity due to the presence of the Dynol surfactant [171, 172]. Altogether, Fig. 5.7 demonstrates that the Dynol surfactant does not change the initial velocity of liquid ejection, while with increasing waiting times, a change in its effect on the rear of the droplet is observed, i.e., the ejected liquid is slowed down less by the retracting meniscus and its length and pinch-off time increase.

### 5.4.3 Evaporation

We now turn our focus to the question as to whether evaporation is involved in the observed increase in droplet velocity and pinch-off time. To be able to perform experiments with bulk surfactant concentrations above the CMC, in what follows, we use Triton surfactant as Dynol phase separates (oils out) at concentrations larger than the CMC [185]. On the other hand, Triton forms nanometer-sized micelles at bulk concentrations above the CMC [186]. We first confirmed that the observed increase in jet velocity with waiting time is also present for jetting experiments with a 1 CMC Triton solution, see Fig. 5.8a. Indeed, a highly similar trend is observed: the droplet velocity increases with waiting time, while presenting significant differences. First, the velocity increase at a waiting time of 200 s and the relative humidity of the lab (70%) was only 6%, whereas for Dynol the velocity increase was 40%. Furthermore, the time-dependent velocity of the liquid jet during its ejection from the nozzle was different (see appendix Fig. 5.13). For Triton, the increase in jet velocity appears to be present from the start of the ejection process onward whereas for

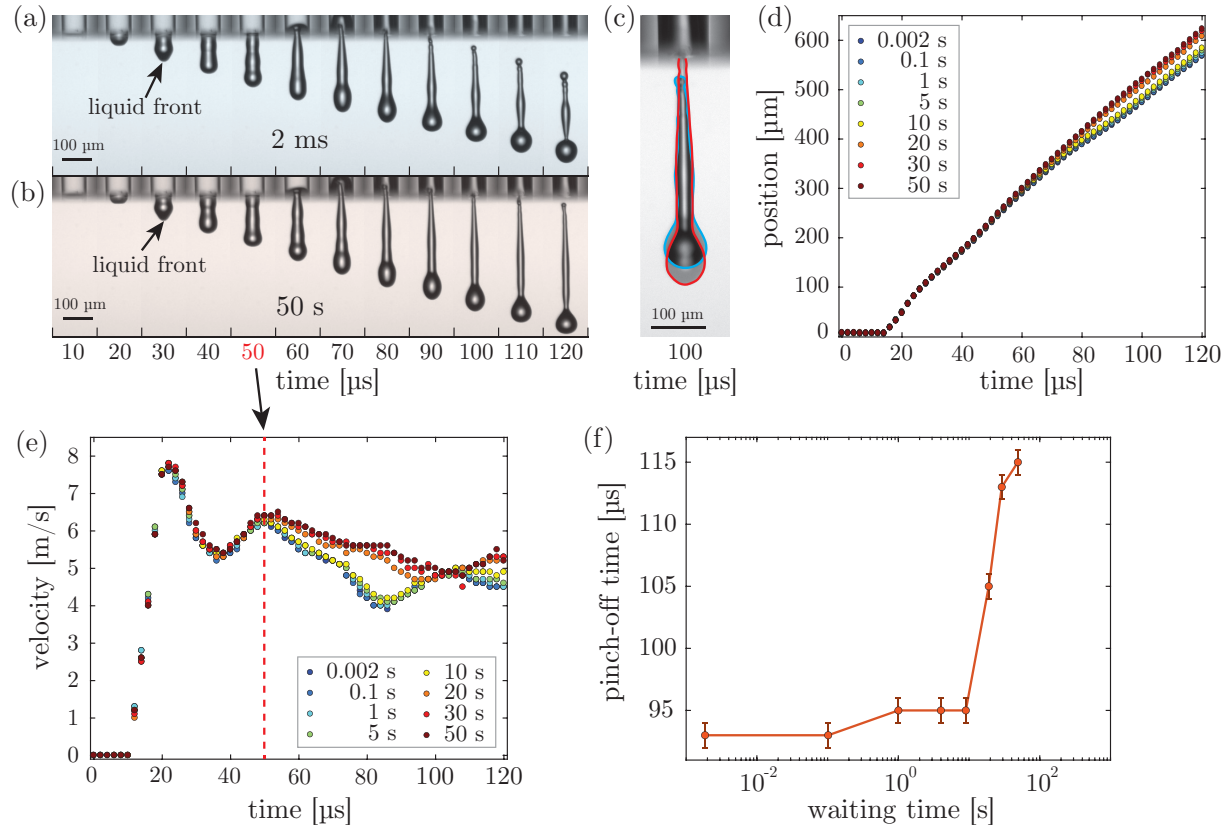


Figure 5.7: Snapshot of droplet formation of 1 CMC Dynol from a  $70\text{ }\mu\text{m}$  nozzle diameter for a waiting time of (a) 2 ms and (b) 50 s. (c) Overlap of the two experiments in (a) in red, and (b) in blue at  $100\text{ }\mu\text{s}$ . (d) The position of the liquid front for multiple waiting times. (e) The velocity of the liquid front for multiple waiting times. (f) The pinch-off time of the liquid column from the nozzle for multiple waiting times.

Dynol is was only apparent  $50\text{ }\mu\text{s}$  after the start of the piezo actuation pulse. This difference may be caused by the slower adsorption kinetics of Triton due to Triton being a bigger molecule than Dynol, resulting in a lower diffusivity. However, more importantly, the trend of the velocity increase with waiting time is still observed. On top of that, the curve in Fig. 5.8a measured at the decreased relative humidity of 30% confirms that evaporation is driving the droplet velocity increase with waiting time.

The expected effect of evaporation a local increase the surfactant concentration at the nozzle exit, which suggests that a surfactant concentration higher than 1 CMC is required to increase the droplet velocity. Therefore, the measurements were repeated with bulk Triton concentrations of 20, 50, and 100 CMC.

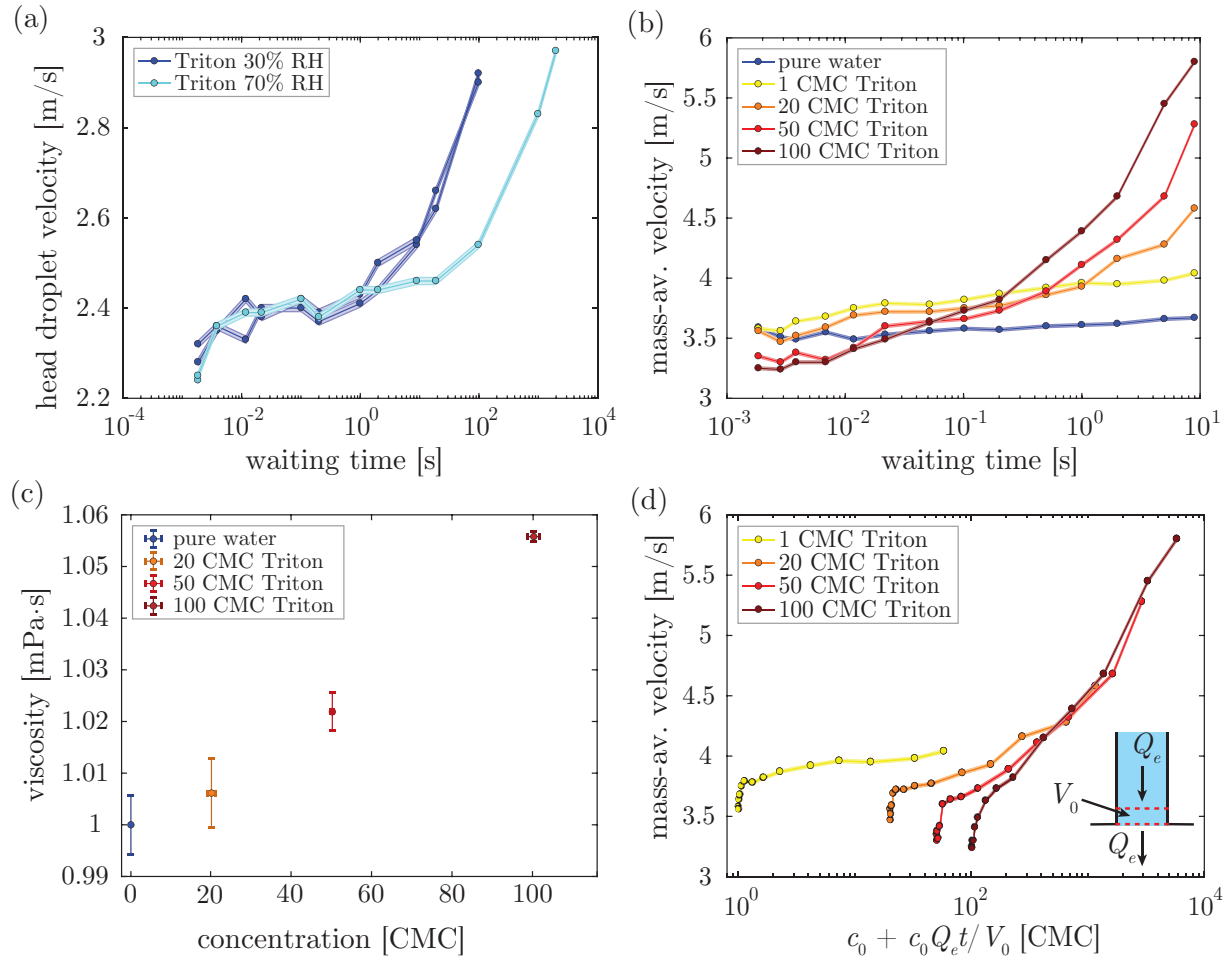


Figure 5.8: (a) Head droplet velocity for a 1 CMC Triton solution from a 50  $\mu\text{m}$  diameter nozzle at two different relative humidities as a function of waiting time. The shaded area represents the error in the analysis of the measurements. (b) Mass-averaged (mass-av.) velocities for pure water and 1 to 100 CMC Triton solutions from a 50  $\mu\text{m}$  diameter nozzle as a function of waiting time. (c) Viscosities for pure water and 20 to 100 CMC Triton solutions measured using a capillary viscometer. (d) Mass-averaged velocities for the different Triton concentrations as a function of the estimated Triton concentration in the control volume  $V_0$  at the nozzle exit, that is sketched in the figure as the red dotted lines.

Increasing the Triton concentration above 100 CMC made the solution too viscous to jet at the applied amplitude of the piezo driving pulse. The mass-averaged droplet velocity obtained for the different Triton concentrations is plotted in Fig. 5.8b as a function of the waiting time. At short time scales



( $< 0.1$  s), the increased Triton concentration resulted in a decreased droplet velocity instead of the expected increase. The decrease in velocity most likely results from the increased bulk viscosity of the high-concentration Triton mixtures, see Fig. 5.8c. At longer waiting times ( $> 0.1$  s), however, the waiting time at which the droplet velocity started to increase, decreased with an increase in Triton concentration. This observation suggests that the increased concentration in the nozzle for an increased droplet velocity is reached earlier. We estimate the surfactant concentration in the nozzle by placing a control volume at the nozzle exit, out of which the water evaporates and is replaced by surfactant solution from the bulk (see inset in Fig. 5.8c). The concentration  $c$  of the surfactant in this volume  $V_0$  is then increasing with waiting time  $t$  beyond the initial concentration  $c_0$  due to the evaporative flux  $Q_e$ , as follows:  $c(t) = c_0 + c_0 Q_e t / V_0$ . The evaporative flux was estimated using the numerical simulations to be  $0.02 \text{ kg}/(\text{m}^2\text{s})$ . The diffusivity of the surfactant is assumed to be negligible, for simplicity. The control volume covers the nozzle exit surface area and we set a depth of  $1 \mu\text{m}$ . Figure 5.8c shows that the droplet velocity curves now collapse at local surfactant concentrations beyond  $\sim 100$  CMC. Increasing the size of the control volume still collapses the data, but now at a longer waiting time. Even though this concentration estimation is based on a number of assumptions and the absolute values should not be trusted, the collapse of the data shows that the local surfactant concentration in the nozzle should be orders of magnitude higher than the CMC to increase the droplet velocity. For example, the 20 CMC solution contains  $\sim 35$  times the initial surfactant concentration when the droplet velocity starts to increase (after a waiting time of 5 s). These results suggest that a thin layer of highly concentrated surfactants at the nozzle exit is required to cause an increase in observable droplet velocity.

To understand how this thin layer of highly concentrated surfactant-layer leads to a droplet velocity increase, we turn to numerical simulations. We simulate only the concentration field of Triton in water and not its adsorption and desorption kinematics. The resulting droplets for two waiting times, 0.05 s and 5 s, are displayed in Fig. 5.9a. The colorbar is kept constant for both images to indicate the differences in Triton concentration. What these two droplet simulations show is that after a waiting time of 5 s, the jetted droplet is coated by a thin layer of highly concentrated surfactants fluid while at a waiting time of 0.05 s the droplet does not even show an increased Triton concentration at the front of the droplet. The entire droplet formation for 5 s can be found



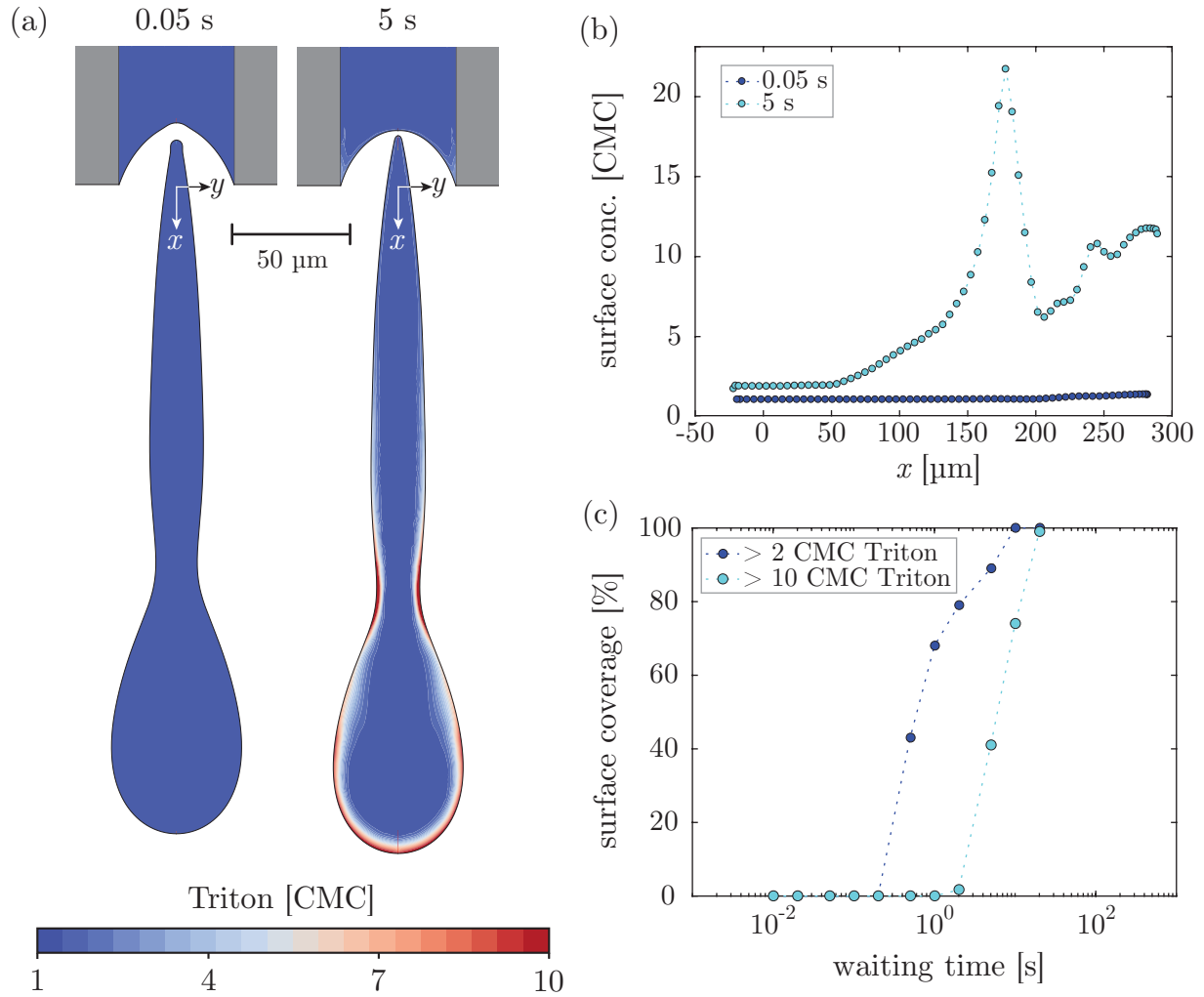


Figure 5.9: Numerical simulations of the droplet formation process using a 1 CMC Triton solution. The left image shows a snapshot for a waiting time of 0.05 s and the right image that for a waiting time of 5 s. The colorbar indicates the Triton concentration in a range from 1 CMC to 10 CMC. (b) Surface concentration of the droplets in (a) along the droplet's axis of symmetry as indicated by  $x$ . The origin of the  $x$ -axis is indicated in (a). (c) Percentage of Triton covering the surface at a concentration above 2 CMC and above 10 CMC measured from the simulation data at the time instance when the droplet has just pinched off from the nozzle, plotted as a function of waiting time.

in appendix Fig. 5.14. The coating of the droplet by a high concentration layer of Triton is more convincingly shown in Fig. 5.9b, where we plot the surface concentration of surfactant. The surface coverage over time, defined

as the percentage of surface area containing the desired concentration compared to the total surface area, for a surface concentration  $> 2$  CMC and for a concentration  $> 10$  CMC are plotted in Fig. 5.9c. These results show that the surfactant surface concentration on the jetted droplet increases beyond the bulk concentration for waiting times of the order of seconds, exactly the timescale at which the experimental droplet velocities were shown to increase. Therefore, we hypothesize that the surfactants studied here, which typically adsorb onto a newly formed surface in the millisecond to second timescale, can adsorb at the microsecond timescale of the droplet formation process once the local surfactant concentration at the liquid-air interface of the jet is reaching the order of 100 to 1000 CMC. Surfactant adsorption at the microsecond timescale then lowers the surface tension at the timescale of droplet formation, thereby increasing the jet velocity. We further argue that the increase in drop velocity with waiting time for Dynol results from the rear of the filament being coated to a larger extent with an increase in waiting time due to a thicker layer of high-surfactant concentration fluid being present at the nozzle exit.

The implications of the unraveling of the thin layer at the nozzle exit covering the entire droplet's surface extends beyond the interest of surfactants. This is a property that likely holds true for any material having a local higher concentration at the nozzle exit, including pigment particles and dyes. Furthermore, the results of surfactants having minor influence on the droplet formation at high droplet production frequencies during droplet production in air will be of interest to the development of new ink formulations, as the surfactants are already extensively used for stabilizing colloidal suspensions as well as the droplet behavior on the substrate.

## 5.5 Conclusion

In this work, the role of surfactants in inkjet printing was studied at timescales spanning over 8 orders of magnitude, i.e., from the microsecond timescale of the droplet formation process to the minute timescale of the evaporation process taking place between the ejection of two successive droplets. When the time between successive droplets was less than one second, surfactants were shown to only influence the details of the break-up dynamics of the jetted filament while the drop velocity and volume remain unchanged from the pure water case. However, droplet velocity and volume increase monotonically with an increase in the time between successive droplets when this time exceeds one

second, i.e. when the droplet generation frequency is lower than 1 Hz. The increase in droplet velocity was shown to correlate with a decrease in surface tension. We demonstrate that the observed velocity increase, and surface tension decrease, are evaporation driven. Evaporation of water at the nozzle exit for a duration of 10 s was estimated to increase the local surfactant concentration by as much as two orders of magnitude. Using numerical simulations, we demonstrate that a thin layer with an increased surfactant concentration located at the nozzle exit can coat the entire jetted liquid filament. We argue that when the surfactant concentration at the nozzle exit reaches a concentration on the order of 100 to 1000 CMC, the adsorption timescale of surfactants can decrease from milliseconds to microseconds thereby lowering the surface tension, and increasing the jet velocity, at the microsecond timescale of jet formation in inkjet printing.

## 5.6 Appendix

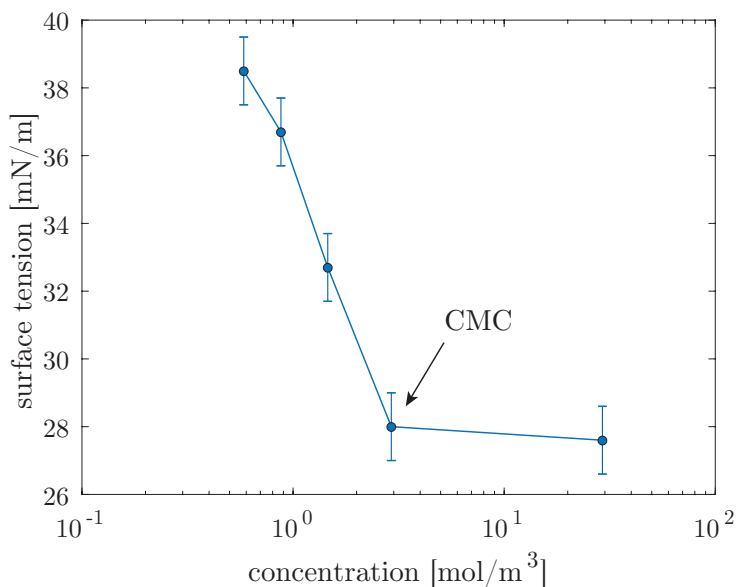


Figure 5.10: Equilibrium surface tension measurement for Dynol, measured with the pendant drop method [187].

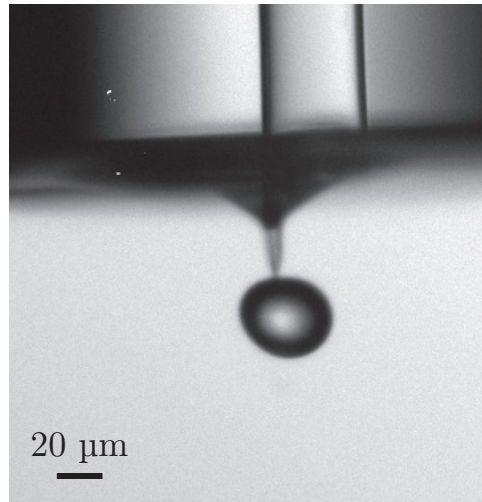


Figure 5.11: Wetting during droplet formation with 1 CMC Dynol after a waiting time of 10 ms and a driving amplitude of 75 V.

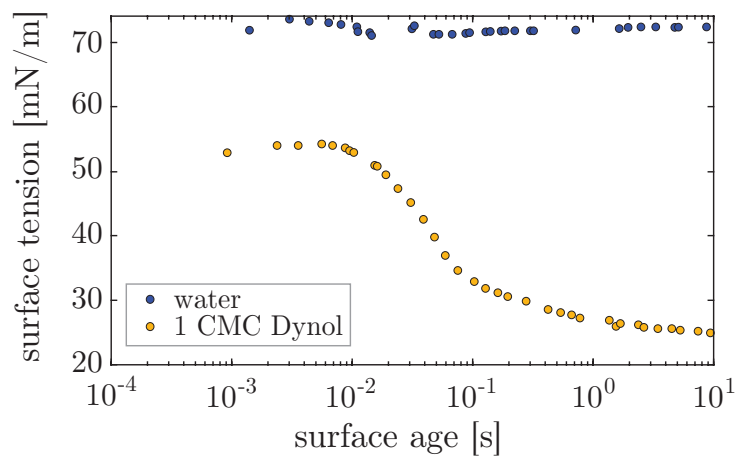


Figure 5.12: Dynamic surface tension of water and 1 CMC Dynol, measured with a maximum bubble pressure tensiometer (Sinterface, BPA-1S).

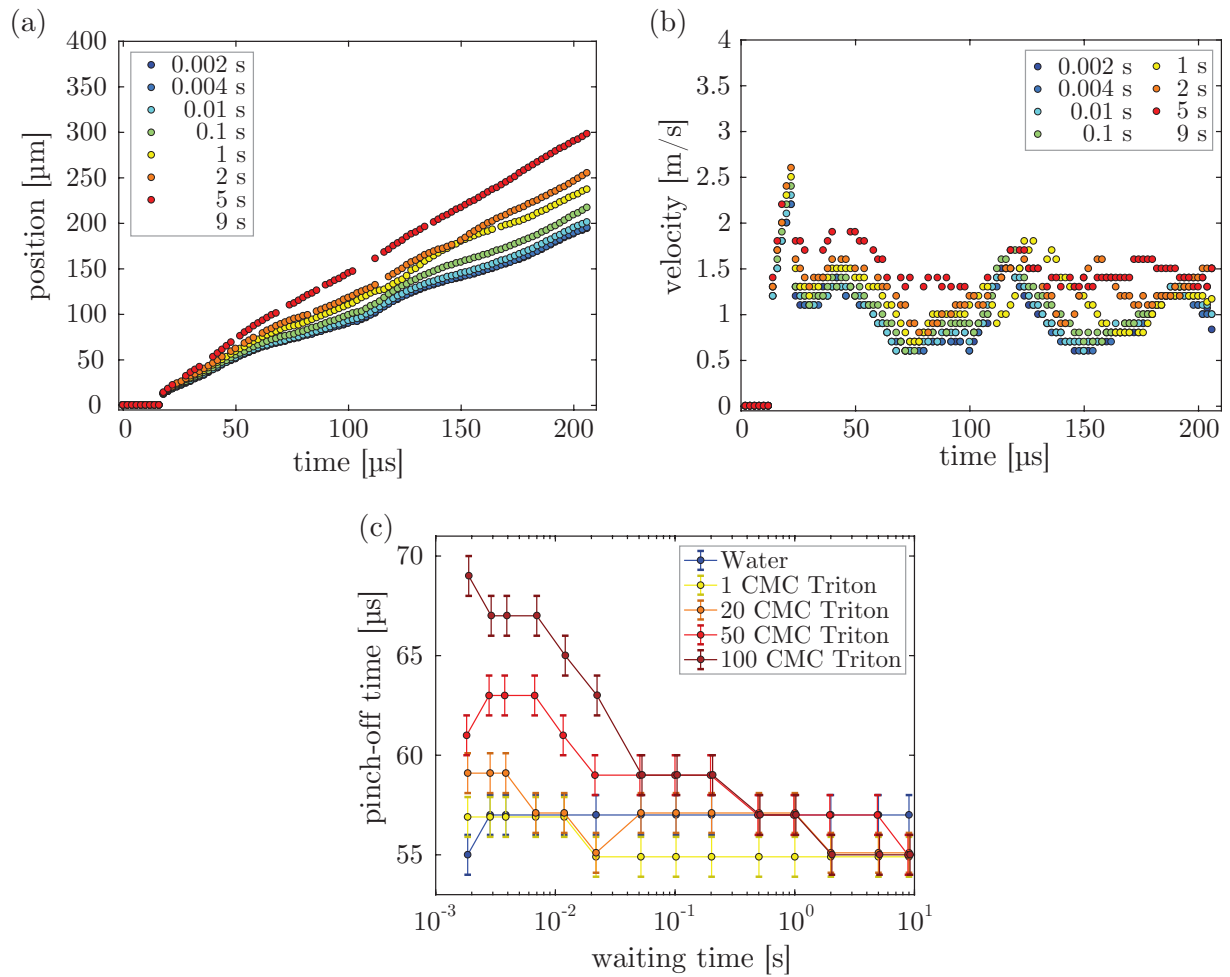


Figure 5.13: (a) Position of the liquid front during jetting of 100 CMC. (b) Corresponding velocity of the liquid front. (c) Pinch-off time of the liquid column for pure water different concentrations of Triton. The datapoints have an artificial (vertical or horizontal) offset in (c) to provide visibility of datapoints on the same location.

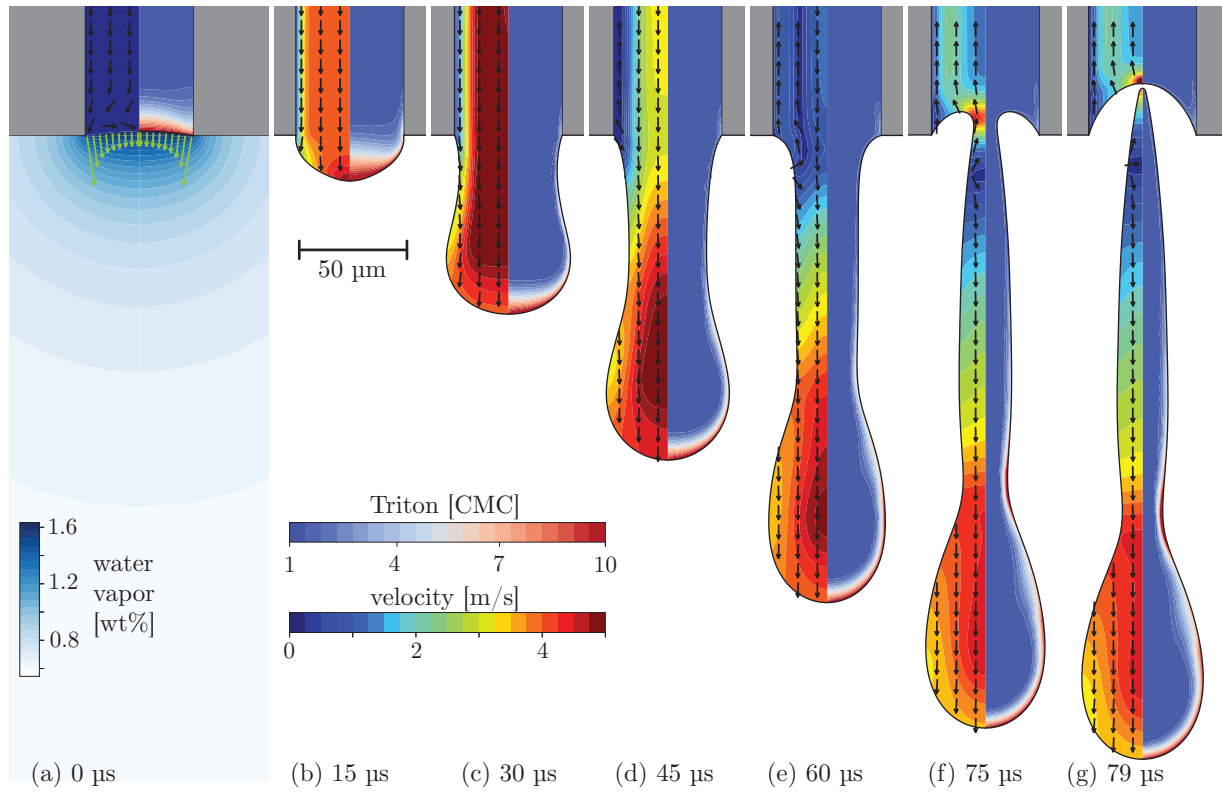


Figure 5.14: Snapshots from numerics for the droplet formation process with a drying time of 5 s. The numerical simulations provide two color schemes inside the liquid: the left hand side of the nozzle shows the velocity profile while the right hand side shows the Triton concentration. The water evaporation rate is around  $20 \text{ g}/(\text{m}^2\text{s})$ . Snapshots (a) shows the nozzle before droplet formation, and (b)-(g) show the droplet formation process. (g) The same snapshot as in Fig. [5.9a](#) for the 5 s drying time.

## Conclusions & Outlook

In this thesis, we have studied the deformations of the meniscus (chapters 1-3) and the dynamics of multi-component fluids (chapter 4-5) at the nozzle of a piezoacoustic drop-on-demand inkjet printer. The aims of the research presented in this thesis are all related to keeping the droplet formation reliable and undisturbed, and aid towards faster inkjet printers with smaller droplets. In the following sections, we elaborate on the conclusions of all the chapters with suggestions for future research based on the remaining open questions and interesting experimental observations.

### Driving pulses leading to bubbles and smaller droplets

The results of chapters 1 and 2 show that the oscillating flows in an inkjet printhead can lead to bubble pinch-off and entrainment via geometric flow-focusing. We demonstrate that this geometrical flow-focusing is a result of vortical rings in the fluid just above the meniscus. We have shown that the presence of this vorticity is a leading factor in bubble entrainment in a piezoacoustic inkjet printhead. The open question that remain in this work is the mechanism of the bubble pinch-off itself. The simulations show that a vortex is also present around the air jet, which could be assisting the bubble pinch-off. In the experiments, we tracked the length of the jet, as shown in Fig. 1a. What we see is that the air jet upward into the nozzle pinches at its the maximum length. However, after the pinch-off, the center of the meniscus moves downwards, producing a liquid jet. The liquid jet becomes more than three times as long, but does not pinch-off. This suggests that the the vortex in the liquid around the air jet aids in the pinch-off. Furthermore, when measuring the aspect ratio of the air jet at its maximum length, both the experiments (Fig. 1b) and numerics (Fig. 1c) reveal that there is not a critical aspect ratio



involved for the pinch-off to occur. This has to be investigated further to be able to predict when the air jet pinches off.

The study in chapter 3 on the driving of the different meniscus modes at the nozzle exit demonstrates that these modes are not well predicted by the typical capillary dispersion relation that describes an undriven system. However, the results from numerical simulations of a driven system still deviate from the experimental results. This indicates that there is still something lacking in our

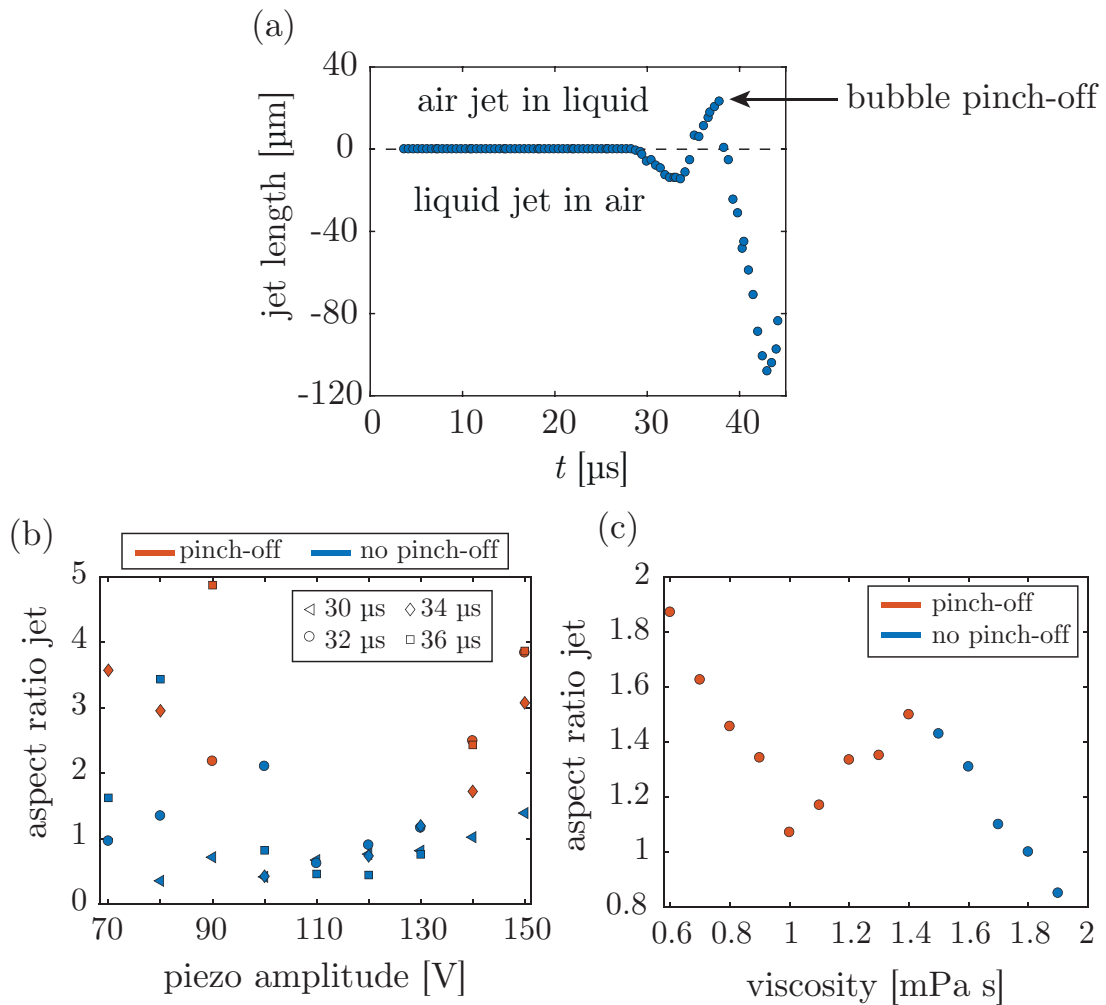


Figure 1: (a) Tracking the length of the jet as a function of time. When the jet has a positive length, it is an air jet in liquid, and when the length is negative, it is a liquid jet in air. (b) Ratio of jet length and jet radius for experiments with different pulse width and amplitude. (c) The numerical results for the aspect ratio of the jet as function of viscosity.

understanding of the driving of the meniscus modes. One possible reason for the deviation could be the coupling between the acoustics of the ink channel and the meniscus modes. To be able to investigate this, the acoustics of the system should be well understood, which is not the case in the currently used printhead. The acoustics of the printhead used in chapter 4 are much better understood. Therefore, performing the experiments from chapter 3 with this printhead should provide insights into the coupling between the acoustics in the channel and the shapes of the meniscus.

## Liquid properties of a drying ink

Chapter 4 demonstrates the ability to determine the composition of the liquid mixture inside the nozzle over time by measuring the channel acoustics ring-down signal with the piezo element and using the proposed analytical model. Furthermore, the experiments reveal that the system comes to a steady state after an extended period of evaporation. Another observation was made during the experimental investigation when closing the nozzle exit to obtain the

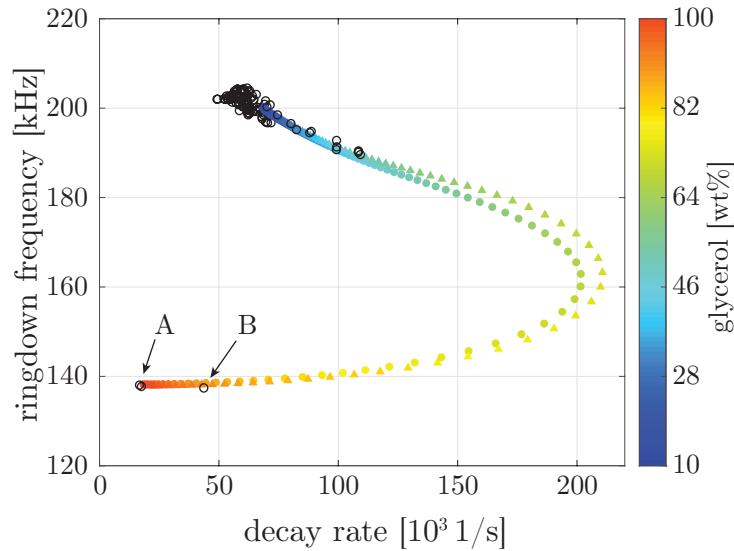


Figure 2: Ringdown frequency and decay rate obtained from experiments (open o), analytical model (filled o), and numerical simulations ( $\triangle$ ) as shown in Ch. 4. The arrow at A points toward the results obtained by manually closing the nozzle, while the arrow at A points toward the result from placing scotch tape at the nozzle exit.

datapoints at A in Fig. 2a: When the nozzle was not manually closed, but instead a piece of scotch tape was used, the resulting frequency and decay rate lie on the curve, but not at the location that indicates no movement in the nozzle, as indicated by B in Fig. 2b. That there is still movement in the nozzle, could be due to the elasticity of the scotch tape. This suggests a very interesting method for measuring material elasticity, although it should first be confirmed that it is indeed the elasticity that is measured.

Another proposal for future research based on chapter 4 is related to the measurement of the ringdown signal. As indicated in the analytical model, there are two oscillatory modes present in the employed printhead, the Helmholtz mode and the slosh mode. It is also demonstrated that the resonance frequency of these modes depends on the liquid properties, with the slosh mode frequency being very sensitive on the surface tension of the ink. However, the slosh mode was not observed in the experimental results, likely due to the signal-to-noise ratio of the ringdown signal. Therefore, improving the signal-to-noise ratio could provide this measurement parameter as well. A possible method is by increasing the amplitude of the piezo during the probe pulse, which was fixed in this chapter to 5 V to prevent droplet formation. However, this was not done marginally, meaning the voltage can still be increased before droplet formation occurs. Furthermore, reducing the viscosity of the liquid allows for a longer recording of the signal, thereby increasing the accuracy during the analysis. Another method to change the actuation pulse width. In the presented study, the system was actuated with a pulse width closely resembling the wavelength corresponding to the Helmholtz resonance frequency. Therefore, the ringdown frequency was also close to the Helmholtz resonance frequency. If the excitation frequency is closer to the slosh mode frequency, it is expected that the ringdown frequency is also close to the slosh mode frequency. To conclude, measuring the slosh mode frequency of the system allows for the measurement of the dynamic surface tension at the meniscus on shorter timescales than the current limitation at 1 ms when using a bubble pressure tensiometer.

The results of chapter 5 show that the droplet velocity of a water-surfactant mixture increases as soon as evaporation takes place, and the investigation leads to the hypothesis that a local high concentration of surfactant increases the adsorption rate onto the surface. The validation of this hypothesis is the main open question at the end of this chapter. One way to answer this question

is to measure the dynamic surface tension of high surfactant concentrations on the microsecond time-scale. However, this is currently not possible. The proposed method in the previous paragraph on measuring the slosh mode frequency is a potential solution for this problem. Another solution is based on observations from the droplet oscillation experiments in this chapter. As illustrated by Fig. 3a and b, the measured surface tension of a droplet decreases as the surface area reduction increases. This measurement of change in surface tension as function of reduced surface area is also used in Langmuir-Blodgett trough measurements, illustrated in Fig. 3c, which uses these measurements to determine the amount of surfactant present on the surface. The method we propose here could therefore lead to the same result, but now at the short time-scales involved in inkjet printing, instead of the time-scale of seconds from the Langmuir-Blodgett trough.

Furthermore, the method of determining surface tension and viscosity from an oscillating droplet, does not take into account surface viscosity. It is another interesting parameter to have dynamic measurements of on short timescales as it is expected to change with the amount of surfactant present on the surface. Extending the current theory at the base of the oscillating droplet method with surface viscosity could be achieved by measuring droplet oscillations in a more controlled system, like an acoustic levitator, and using liquids with well known properties. The viability has to be investigated.

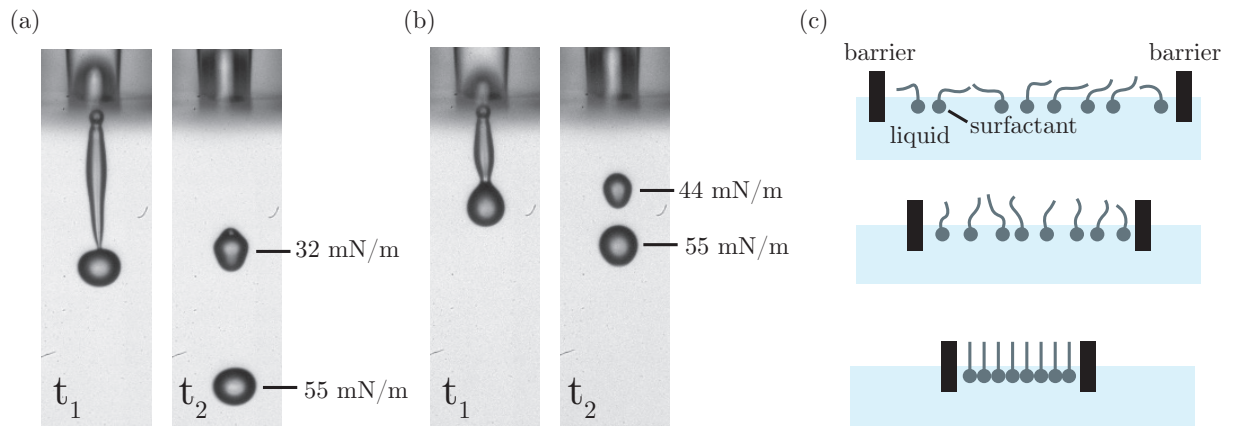


Figure 3: The surface tension of the head and satellite droplet after a waiting time of 10s and a driving voltage of (a) 60 V and (b) 50 V. (c) Langmuir-Blodgett trough method, where the surface tension is usually measured with a Wilhemly plate in between the barriers.

## References

- [1] H. Wijshoff, “The dynamics of the piezo inkjet printhead operation”, *Phys. Rep.* **491**, 77 (2010).
- [2] S. D. Hoath, *Fundamentals of Inkjet Printing* (Wiley-VCH) (2016).
- [3] D. Lohse, “Fundamental fluid dynamics challenges in inkjet printing”, *Annu. Rev. Fluid Mech.* **54**, 349–382 (2022).
- [4] D. Derby, “Inkjet printing of functional and structural materials: fluid property requirements, feature stability, and resolution”, *Annu. Rev. Mater. Res.* **40** (2010).
- [5] D. Cressey, “365 days: Images of the year”, *Nature* **516**, 304–309 (2014).
- [6] T. Shimoda, K. Morii, S. Seki, and H. Kiguchi, “Inkjet printing of light-emitting polymer displays”, *MRS Bull.* **28**, 821–827 (2003).
- [7] C. Wei, W. Su, J. Li, B. Xu, Q. Shan, Y. Wu, F. Zhang, M. Luo, H. Xiang, Z. Cui, and H. Zeng, “A universal ternary-solvent-ink strategy toward efficient inkjet-printed perovskite quantum dot light-emitting diodes”, *Adv. Mater.* **34**, 2107798 (2022).
- [8] H. Sirringhaus, T. Kawase, R. H. Friend, T. Shimoda, M. Inbasekaran, W. Wu, and E. P. Woo, “High-resolution inkjet printing of all-polymer transistor circuits”, *Science* **290**, 2123–2126 (2000).
- [9] S. Majee, M. Song, S.-L. Zhang, and Z.-B. Zhang, “Scalable inkjet printing of shear-exfoliated graphene transparent conductive films”, *Carbon* **102**, 51–57 (2016).

- [10] S. Majee, C. Liu, B. Wu, S.-L. Zhang, and Z.-B. Zhang, “Ink-jet printed highly conductive pristine graphene patterns achieved with water-based ink and aqueous doping processing”, *Carbon* **114**, 77–83 (2017).
- [11] G. Villar, A. D. Graham, and H. Bayley, “A tissue-like printed material”, *Science* **340**, 48–52 (2013).
- [12] A. Simaite, F. Mesnilgrente, B. Tondou, P. Souères, and C. Bergaud, “Towards inkjet printable conducting polymer artificial muscles”, *Sens. Actuators B* **229**, 425–433 (2016).
- [13] R. Daly, T. S. Harrington, G. D. Martin, and I. M. Hutchings, “Inkjet printing for pharmaceuticals - a review of research and manufacturing”, *Int. J. Pharm.* **494**, 554–567 (2015).
- [14] W. van der Kruk, S. Smit, T. Segers, X. Li, and C. Venner, “Drop-on-demand printing as novel method of oil supply in elastohydrodynamic lubrication”, *Tribol. Lett.* **67**, 1–12 (2019).
- [15] T.-T. Huang and W. Wu, “Scalable nanomanufacturing of inkjet-printed wearable energy storage devices”, *J. Mater. Chem. A* **7**, 23280 (2019).
- [16] G. McKinley and M. Renardy, “Wolfgang von Ohnesorge”, *Phys. Fluids* **23**, 127101 (2011).
- [17] A. Fraters, M. van den Berg, Y. de Loore, H. Reinten, H. Wijshoff, D. Lohse, M. Versluis, and T. Segers, “Inkjet nozzle failure by heterogeneous nucleation: Bubble entrainment, cavitation, and diffusive growth”, *Phys. Rev. Appl.* **12**, 064019 (2019).
- [18] R. Jeurissen, J. de Jong, H. Reinten, M. van den Berg, H. Wijshoff, M. Versluis, and D. Lohse, “Effect of an entrained air bubble on the acoustics of an ink channel”, *J. Acoust. Soc. Am.* **123**, 2496–2505 (2008).
- [19] R. Jeurissen, A. van der Bos, H. Reinten, M. van den Berg, H. Wijshoff, J. de Jong, M. Versluis, and D. Lohse, “Acoustic measurement of bubble size in an inkjet printhead”, *J. Acoust. Soc. Am.* **126**, 2184–2190 (2009).
- [20] R. Jeurissen, H. Wijshoff, M. van den Berg, H. Reinten, and D. Lohse, “Regimes of bubble volume oscillations in a pipe”, *J. Acoust. Soc. Am.* **130**, 3220–3232 (2011).

- [21] B.-H. Kim, T.-G. Kim, T.-K. Lee, S. Kim, S.-J. Shin, S.-J. Kim, and S.-J. Lee, “Effects of trapped air bubbles on frequency responses of the piezo-driven inkjet printheads and visualization of the bubbles using synchrotron X-ray”, *Sens. Actuator A Phys.* **154**, 132–139 (2009).
- [22] S. Lee, D. Kwon, and Y. Choi, “Dynamics of entrained air bubbles inside a piezodriven inkjet printhead”, *Appl. Phys. Lett.* **95**, 221902 (2009).
- [23] A. van der Bos, T. Segers, R. Jeurissen, M. van den Berg, H. Reinten, H. Wijshoff, M. Versluis, and D. Lohse, “Infrared imaging and acoustic sizing of a bubble inside a micro-electro-mechanical system piezo ink channel”, *J. Appl. Phys.* **110**, 034503 (2011).
- [24] A. Fraters, T. Segers, M. van den Berg, H. Reinten, H. Wijshoff, D. Lohse, and M. Versluis, “Shortwave infrared imaging setup to study entrained air bubble dynamics in a mems-based piezo-acoustic inkjet printhead”, *Exp. Fluids* **60**, 123 (2019).
- [25] J. de Jong, G. de Bruin, H. Reinten, M. van den Berg, H. Wijshoff, M. Versluis, and D. Lohse, “Air entrapment in piezo-driven inkjet print-heads”, *J. Acoust. Soc. Am.* **120**, 1257–1265 (2006).
- [26] J. de Jong, R. Jeurissen, H. Borel, M. van den Berg, H. Wijshoff, H. Reinten, M. Versluis, A. Prosperetti, and D. Lohse, “Entrapped air bubbles in piezo-driven inkjet printing: their effect on the droplet velocity”, *Phys. Fluids* **18**, 121511 (2006).
- [27] H. Wijshoff, “Drop dynamics in the inkjet printing process”, *Curr. Opin. Colloid Interface Sci.* **36**, 20–27 (2018).
- [28] R. F. Burr, D. A. Tence, and S. S. Berger, “Multiple dot size fluidics for phase change piezoelectric ink jets”, *Recent Progress in Ink Jet Technologies II* **2**, 192 – 198 (1999).
- [29] M. Sengun, “Impact of ink evaporation on drop volume and velocity”, 18–21 (1999).
- [30] S. Hoath, W.-K. Hsiao, S. Jung, G. Martin, I. Hutchings, N. Morrison, and O. G. Harlen, “Drop speeds from drop-on-demand ink-jet print heads”, *J. Imaging Sci. Technol.* **57**, 10503 (2013).

- [31] O. A. Basaran, “Small-scale free surface flows with breakup: Drop formation and emerging applications”, *AIChE Journal* **48**, 1842–1848 (2002).
- [32] A. Fraters, R. Jeurissen, M. van den Berg, H. Reinten, H. Wijshoff, D. Lohse, M. Versluis, and T. Segers, “Secondary tail formation and breakup in piezoacoustic inkjet printing: Femtoliter droplets captured in flight”, *Phys. Rev. Applied* **13**, 024075 (2009).
- [33] S. Eshkalak, A. Cinnappan, W. Jayathilaka, M. Khatibzadeh, E. Kowsari, and S. Ramakrishna, “A review on inkjet printing of CNT composites for smart applications”, *Appl. Mater. Today* **9**, 372–386 (2017).
- [34] M. Vilardell, X. Granados, S. Ricart, I. V. Driessche, A. Palau, T. Puig, and X. Obradors, “Flexible manufacturing of functional ceramic coatings by inkjet printing”, *Thin Solid Films* **548**, 489–497 (2013).
- [35] A. Moya, G. Gabriel, R. Villa, and F. J. del Campo, “Inkjet-printed electrochemical sensors”, *Curr. Opin. Electrochem.* **3**, 29–39 (2017).
- [36] T. Eggenhuisen, Y. Galagan, E. Coenen, W. Voorthuijzen, M. Slaats, S. Kommeren, S. Shanmugan, M. Coenen, R. Andriessen, and W. Groen, “Digital fabrication of organic solar cells by inkjet printing using non-halogenated solvents”, *Sol. Energy Mater Sol. Cells* **134**, 364–372 (2015).
- [37] S. Hashmi, M. Ozkan, J. Halme, K. Misic, S. Zakeeruddin, J. Paltakari, M. Grätzel, and P. Lund, “High performance dye-sensitized solar cells with inkjet printed ionic liquid electrolyte”, *Nano Energy* **17**, 206–215 (2015).
- [38] C. Jiang, L. Mu, J. Zou, Z. He, Z. Zhong, L. Wang, M. Xu, J. Wang, J. Peng, and Y. Cao, “Full-color quantum dots active matrix display fabricated by ink-jet printing”, *Sci. China Chem.* **60**, 1349–1355 (2017).
- [39] S. Hewes, A. D. Wong, and P. C. Searson, “Bioprinting microvessels using an inkjet printer”, *Bioprinting* **7**, 14 – 18 (2017).
- [40] M. Nakamura, A. Kobayashi, F. Takagi, A. Watanabe, Y. Hiruma, K. Ohuchi, Y. Iwasaki, M. Horie, I. Morita, and S. Takatani, “Bio-compatible inkjet printing technique for designed seeding of individual living cells”, *Tissue Eng.* **11**, 1658–1666 (2005).



- [41] M. Versluis, “High-speed imaging in fluids”, *Experiments in Fluids* **54**, 1–35 (2013).
- [42] C. Ravasio, S. Hoath, G. Martin, P. Boltryk, and M. Dorrestijn, “Meniscus motion inside a dot inkjet print-head nozzle”, in *NIP & Digital Fabrication Conference*, volume 2016, 348–352 (Society for Imaging Science and Technology) (2016).
- [43] J. van der Bos, A. Zijlstra, E. Gelderblom, and M. Versluis, “iLIF: illumination by laser-induced fluorescence for single flash imaging on a nanoseconds timescale”, *Exp. Fluids* **51**, 1283–1289 (2011).
- [44] H. Nallan, J. Sadie, R. Kitsomboonloha, S. Volkman, and V. Subramanian, “Systematic design of jettable nanoparticle-based inkjet inks: Rheology, acoustics, and jettability”, *Langmuir* **30**, 13470–13477 (2014).
- [45] Rayleigh, “Investigation of the character of the equilibrium of an incompressible heavy fluid of variable density”, *Proc. Lond. Math. Soc.* **14**, 170–177 (1883).
- [46] G. Taylor, “The instability of liquid surfaces when accelerated in a direction perpendicular to their planes. I”, *Proc. R. Soc. Lond. A* **201**, 192–196 (1950).
- [47] M. Faraday, “On a peculiar class of acoustical figures; and on certain forms assumed by groups of particles upon vibrating elastic surfaces”, *Philos. Trans. R. Soc. Lond.* **121**, 299–340 (1831).
- [48] M.-J. van der Meulen, H. Reinten, H. Wijshoff, M. Versluis, D. Lohse, and P. Steen, “Nonaxisymmetric effects in drop-on-demand piezoelectric inkjet printing”, *Phys. Rev. Applied* **13**, 054071 (2020).
- [49] D. Tence, S. Berger, and R. Burr, “Method and apparatus for producing dot size modulation ink jet printing”, Patent. US 5689291. November 2007.
- [50] A. Chen and O. Basaran, “A new method for significantly reducing drop radius without reducing nozzle radius in drop-on-demand drop production”, *Phys. Fluids* **14**, L1–L4 (2002).
- [51] A. Antkowiak, N. Bremond, S. L. Dizès, and E. Villiermaux, “Short-term dynamics of a density interface following an impact”, *J. Fluid Mech.* **577**, 241–250 (2007).

- [52] I. Peters, Y. Tagawa, N. Oudalov, C. Sun, A. Prosperetti, D. Lohse, and D. van der Meer, “Highly focused supersonic microjets: numerical simulations”, *J. Fluid Mech.* **719**, 587 – 605 (2013).
- [53] J. Gordillo, H. Onuki, and Y. Tagawa, “Impulsive generation of jets by flow focusing”, *J. Fluid Mech.* **894**, A3 (2020).
- [54] H. N. Oguz and A. Prosperetti, “Bubble entrainment by the impact of drops on liquid surfaces”, *J. Fluid Mech.* **219**, 143–179 (1990).
- [55] H. C. Pumphrey and P. A. Elmore, “The entrainment of bubbles by drop impacts”, *J. Fluid Mech.* **220**, 539–567 (1990).
- [56] S. T. Thoroddsen, K. Takehara, H. D. Nguyen, and T. G. Etoh, “Singular jets during the collapse of drop-impact craters”, *J. Fluid Mech.* **848**, R3 (2018).
- [57] P. Sleutel, P.-H. Tsai, S. Wildeman, W. Bouwhuis, M.-J. Thoraval, C.-W. Visser, A.-B. Wang, M. Versluis, and D. Lohse, “Bubble entrainment at high-speed microdroplet impact on a liquid pool”, *J. Fluid Mech.* **submitted** (2020).
- [58] L. Duchemin, S. Popinet, C. Josserand, and S. Zaleski, “Jet formation in bubbles bursting at a free surface”, *Phys. Fluids* **14**, 3000–3008 (2002).
- [59] J. M. Gordillo and J. Rodríguez-Rodríguez, “Capillary waves control the ejection of bubble bursting jets”, *J. Fluid Mech.* **867**, 556–571 (2019).
- [60] J. Dijksman, “Hydrodynamics of small tubular pumps”, *J. Fluid Mech.* **139**, 173–191 (1984).
- [61] J. Dijksman, “Hydro-acoustics of piezoelectrically driven ink-jet print heads”, *Flow Turbul. Combust.* **61**, 211–237 (1998).
- [62] J. Segur and H. Oberstar, “Viscosity of glycerol and its aqueous solutions”, *Ind. Eng. Chem. Res.* **43**, 2117–2120 (1951).
- [63] G. P. Association, *Physical properties of glycerine and its solutions* (Glycerine Producers’ Association) (1963).
- [64] ImageJ, <http://imagej.nih.gov/ij>.
- [65] Python Software Foundation, <https://www.python.org/>.

- [66] H. N. Oğuz and A. Prosperetti, “Dynamics of bubble growth and detachment from a needle”, *J. Fluid Mech.* **257**, 111–145 (1993).
- [67] H. Power and L. Wrobel, *Boundary Integral Methods in Fluid Mechanics* (Computational Mechanics Publications) (1995).
- [68] R. Bergmann, D. van der Meer, S. Gekle, A. van der Bos, and D. Lohse, “Controlled impact of a disk on a water surface: Cavity dynamics”, *J. Fluid Mech.* **633**, 381–409 (2009).
- [69] S. Gekle, J. M. Gordillo, D. van der Meer, and D. Lohse, “High-speed jet formation after solid object impact”, *Physical Review Letters* **102**, 034502 (2009).
- [70] M. Minnaert, “XVI. On musical air-bubbles and the sounds of running water”, *Lond. Edinb. Dublin philos. mag. j. sci.* **16**, 235–248 (1933).
- [71] T. Leighton, *The Acoustic Bubble* (Academic Press) (1994).
- [72] J. Castrejón-Pita, G. Martin, and I. Hutchings, “Experimental study of the influence of nozzle defects on drop-on-demand ink jets”, *J. Imaging Sci. Technol.* **55**, 40305–1 (2011).
- [73] APC International, Ltd, *Piezoelectric Ceramics: Principles and Applications* (APC International) (2011).
- [74] APC International, Ltd., “APC Piezo Calculator”, <https://www.americanpiezo.com/knowledge-center/apc-piezo-calc.html>.
- [75] Y. Li, O. Dahhan, C. D. M. Filipe, J. D. Brennan, and R. H. Pelton, “Deposited nanoparticles can promote air clogging of piezoelectric inkjet printhead nozzles”, *Langmuir* **35**, 5517–5524 (2019).
- [76] A. Fraters, M. Rump, R. Jeurissen, M. van den Berg, Y. de Loore, H. Reinten, H. Wijshoff, D. van der Meer, D. Lohse, M. Versluis, and T. Segers, “Meniscus oscillations driven by flow focusing lead to bubble pinch-off and entrainment in a piezoacoustic inkjet nozzle”, *Phys. Rev. Appl.* **16**, 044052 (2021).
- [77] A. Kiyama, Y. Tagawa, K. Ando, and M. Kameda, “Effects of a water hammer and cavitation on jet formation in a test tube”, *J. Fluid Mech.* **787**, 224–236 (2016).

- [78] Y. Tagawa, N. Oudalov, C. Visser, I. Peters, D. van der Meer, C. Sun, A. Prosperetti, and D. Lohse, “Highly focused supersonic microjets”, *Phys. Rev. X* **2**, 031002 (2012).
- [79] P. Delrot, M. Modestino, F. Gallaire, D. Psaltis, and C. Moser, “Inkjet printing of viscous monodisperse microdroplets by laser-induced flow focusing”, *Phys. Rev. Appl.* **6**, 024003 (2016).
- [80] K. Fezzaa and Y. Wang, “Ultrafast x-ray phase-contrast imaging of the initial coalescence phase of two water droplets”, *Phys. Rev. Lett.* **100**, 104501 (2008).
- [81] L. V. Zhang, J. Toole, K. Fezzaa, and R. D. Deegan, “Splashing from drop impact into a deep pool: multiplicity of jets and the failure of conventional scaling”, *J. Fluid Mech.* **703**, 402–413 (2012).
- [82] J. S. Lee, S. J. Park, J. H. Lee, B. M. Weon, K. Fezzaa, and J. H. Je, “Origin and dynamics of vortex rings in drop splashing”, *Nat. Commun.* **6**, 8187 (2015).
- [83] A. Lee, K. Sudau, K. H. Ahn, S. J. Lee, and N. Willenbacher, “Optimization of experimental parameters to suppress nozzle clogging in inkjet printing”, *Ind. Eng. Chem. Res.* **51**, 13195–13204 (2012).
- [84] S.-H. Lee, M. Rump, K. Harth, M. Kim, D. Lohse, K. Fezzaa, and J. H. Je, “Downward jetting of a dynamic leidenfrost drop”, *Phys. Rev. Fluids* **5**, 074802 (2020).
- [85] N. D. Parab, J. E. Barnes, C. Zhao, R. W. Cunningham, K. Fezzaa, A. D. Rollett, and T. Sun, “Real time observation of binder jetting printing process using high-speed x-ray imaging”, *Sci. Rep.* **9**, 2499 (2019).
- [86] <https://ops.aps.anl.gov/SRparameters/node5.html>.
- [87] D. Fuster, G. Agbaglah, C. Josserand, S. Popinet, and S. Zaleski, “Numerical simulation of droplets, bubbles and waves: state of the art”, *Fluid Dyn. Res.* **41**, 065001 (2009).
- [88] F. Zhang, M.-J. , S. T. Thoroddsen, and P. Taborek, “Partial coalescence from bubbles to drops”, *J. Fluid Mech.* **782**, 209–239 (2015).

- [89] M.-J. Thoraval, Y. Li, and S. T. Thoroddsen, “Vortex-ring-induced large bubble entrainment during drop impact”, *Phys. Rev. E* **93**, 033128 (2016).
- [90] F. P. Contò, J. F. Marín, A. Antkowiak, J. R. Castrejón-Pita, and L. Gordillo, “Shape of a recoiling liquid filament”, *Sci. Rep.* **9**, 1–8 (2019).
- [91] A. M. Gañán-Calvo, H. N. Chapman, M. Heymann, M. O. Wiedorn, J. Knoska, B. Gañán-Riesco, J. M. López-Herrera, F. Cruz-Mazo, M. A. Herrada, J. M. Montanero, and S. Bajt, “The natural breakup length of a steady capillary jet: Application to serial femtosecond crystallography”, *Crystals* **11**, 990 (2021).
- [92] S. W. Wilkins, T. E. Gureyev, D. Gao, A. Pogany, and A. W. Stevenson, “Phase-contrast imaging using polychromatic hard x-rays”, *Nature* **384**, 335–338 (1996).
- [93] S. C. Mayo, A. W. Stevenson, and S. W. Wilkins, “In-line phase-contrast x-ray imaging and tomography for materials science”, *Materials* **5**, 937–965 (2012).
- [94] A. van der Bos, M.-J. van der Meulen, T. Driessen, M. van den Berg, H. Reinten, H. Wijshoff, M. Versluis, and D. Lohse, “Velocity profile inside piezoacoustic inkjet droplets in flight: Comparison between experiment and numerical simulation”, *Phys. Rev. Appl.* **1**, 014004 (2014).
- [95] S. Popinet, “A quadtree-adaptive multigrid solver for the serre–green–naghdi equations”, *J. Comput. Phys.* **302**, 336–358 (2015).
- [96] J. U. Brackbill, D. B. Kothe, and C. Zemach, “A continuum method for modeling surface tension”, *J. Comput. Phys.* **100**, 335 – 354 (1992).
- [97] S. Popinet, “Gerris: a tree-based adaptive solver for the incompressible Euler equations in complex geometries”, *J. Comput. Phys.* **190**, 572 – 600 (2003).
- [98] S. Popinet, “An accurate adaptive solver for surface-tension-driven interfacial flows”, *J. Comput. Phys.* **228**, 5838–5866 (2009).
- [99] P.-Y. Lagrée, L. Staron, and S. Popinet, “The granular column collapse as a continuum: validity of a two-dimensional Navier–Stokes model with a  $\mu$  (i)-rheology”, *J. Fluid Mech.* **686**, 378–408 (2011).

- [100] R. Scardovelli and S. Zaleski, “Direct numerical simulation of free-surface and interfacial flow”, *Annu. Rev. Fluid Mech.* **31**, 567–603 (1999).
- [101] S. Afkhami, J. Buongiorno, A. Guion, S. Popinet, Y. Saade, R. Scardovelli, and S. Zaleski, “Transition in a numerical model of contact line dynamics and forced dewetting”, *J. Comput. Phys.* **374**, 1061–1093 (2018).
- [102] L. Deike, E. Ghabache, G. Liger-Belair, A. K. Das, S. Zaleski, S. Popinet, and T. Séon, “Dynamics of jets produced by bursting bubbles”, *Phys. Rev. Fluids* **3**, 013603 (2018).
- [103] V. Sanjay, D. Lohse, and M. Jalaal, “Bursting bubble in a viscoplastic medium”, *J. Fluid Mech.* **922**, A2 (2021).
- [104] J. Magnaudet and M. J. Mercier, “Particles, drops, and bubbles moving across sharp interfaces and stratified layers”, *Annu. Rev. Fluid Mech.* **52**, 61–91 (2020).
- [105] D. Fuster and M. Rossi, “Vortex-interface interactions in two-dimensional flows”, *Int. J. Multiph. Flow* **143**, 103757 (2021).
- [106] M. Rossi and D. Fuster, “Vorticity production at fluid interfaces in two-dimensional flows”, *arXiv preprint arXiv:2102.05878* (2021).
- [107] J.-Z. Wu, “A theory of three-dimensional interfacial vorticity dynamics”, *Phys. Fluids* **7**, 2375–2395 (1995).
- [108] S. T. W. Nam-Trung Nguyen, *Fundamentals and Applications of Microfluidics* (ARTECH HOUSE, INC.) (2006).
- [109] K. Fukuda, T. Sekine, D. Kumaki, and S. Tokito, “Profile control of inkjet printed silver electrodes and their application to organic transistors”, *ACS Applied Materials & Interfaces* **5**, 3916–3920 (2013).
- [110] M. Versluis, D. E. Goertz, P. Palanchon, I. L. Heitman, S. M. van der Meer, B. Dollet, N. de Jong, and D. Lohse, “Microbubble shape oscillations excited through ultrasonic parametric driving”, *Phys. Rev. E* **82**, 026321 (2010).
- [111] J. Xu and D. Attinger, “Acoustic excitation of superharmonic capillary waves on a meniscus in a planar microgeometry”, *Phys. Fluids* **19**, 108107 (2007).

- [112] A. Royon-Lebeaud, E. J. Hopfinger, and A. Cartellier, “Liquid sloshing and wave breaking in circular and square-base cylindrical containers”, *J. Fluid Mech.* **577**, 467–494 (2007).
- [113] D. Gritsenko, Y. Lin, V. Hovorka, Z. Zhang, A. Ahmadianyazdi, and J. Xu, “Vibrational modes prediction for water-air bubbles trapped in circular microcavities”, *Phys. Fluids* **30**, 082001 (2018).
- [114] H. Gelderblom, A. G. Zijlstra, L. van Wijngaarden, and A. Prosperetti, “Oscillations of a gas pocket on a liquid-covered solid surface”, *Phys. Fluids* **24**, 122101 (2012).
- [115] A. Prosperetti, “Linear oscillations of constrained drops, bubbles, and plane liquid surfaces”, *Phys. Fluids* **24**, 032109 (2012).
- [116] E. N. Leith and J. Upatnieks, “Reconstructed wavefronts and communication theory\*”, *J. Opt. Soc. Am.* **52**, 1123–1130 (1962).
- [117] H. Xia, S. Montresor, R. Guo, J. Li, F. Yan, H. Cheng, and P. Piccart, “Phase calibration unwrapping algorithm for phase data corrupted by strong decorrelation speckle noise”, *Opt. Express* **24**, 28713–28730 (2016).
- [118] B. Kim, S. Lee, S. Kim, P. Kang, and Y.-S. Park, “Hydrodynamics responses of a piezoelectric driven MEMS inkjet print-head”, *Sens. Actuators A* **210**, 131–140 (2014).
- [119] J. F. Dijksman, *Design of Piezo Inkjet Print Heads* (John Wiley & Sons) (2018).
- [120] D. Lohse and X. Zhang, “Physicochemical hydrodynamics of droplets out of equilibrium”, *Nat. Rev. Phys.* **2**, 426–443 (2020).
- [121] K. Sefiane, “Patterns from drying drops”, *Adv. Colloid Interface Sci.* **206**, 372–381 (2014).
- [122] H. Kim, F. Boulogne, E. Um, I. Jacobi, E. Button, and H. A. Stone, “Controlled uniform coating from the interplay of Marangoni flows and surface-adsorbed macromolecules”, *Phys. Rev. Lett.* **116**, 124501 (2016).
- [123] R. D. Deegan, O. Bakajin, T. F. Dupont, G. Huber, S. R. Nagel, and T. A. Witten, “Capillary flows as the cause of ring stains from dried liquid drops”, *Nature* **389**, 827–829 (1997).

- [124] E. L. Talbot, H. N. Yow, L. Yang, A. Berson, S. R. Biggs, and C. D. Bain, “Printing small dots from large droplets”, *ACS Appl. Mater. Interfaces* **7**, 3782–3790 (2015).
- [125] S. Karpitschka, F. Liebig, and H. Riegler, “Marangoni contraction of evaporating sessile droplets of binary mixtures”, *Langmuir* **33**, 4682–4687 (2017).
- [126] A. Marin, S. Karpitschka, D. Noguera-Marín, M. A. Cabrerizo-Vílchez, M. Rossi, C. J. Kähler, and M. A. Rodríguez-Valverde, “Solutal Marangoni flow as the cause of ring stains from drying salty colloidal drops”, *Phys. Rev. Fluids* **4**, 041601(R) (2019).
- [127] A. P. Mouat, C. E. Wood, J. E. Pye, and J. C. Burton, “Tuning contact line dynamics and deposition patterns in volatile liquid mixtures”, *Phys. Rev. Lett.* **124**, 064502 (2020).
- [128] W. D. Ristenpart, P. G. Kim, C. Domingues, J. Wan, and H. A. Stone, “Influence of substrate conductivity on circulation reversal in evaporating drops”, *Phys. Rev. Lett.* **99**, 234502 (2007).
- [129] S. Y. Lee, H. Kim, S.-H. Kim, and H. A. Stone, “Uniform coating of self-assembled noniridescent colloidal nanostructures using the Marangoni effect and polymers”, *Phys. Rev. Appl.* **10**, 054003 (2018).
- [130] H. Tan, C. Diddens, P. Lv, J. G. M. Kuerten, X. Zhang, and D. Lohse, “Evaporation-triggered microdroplet nucleation and the four life phases of an evaporating Ouzo drop”, *Proc. Natl. Acad. Sci.* **113**, 8642–8647 (2016).
- [131] H. Tan, C. Diddens, M. Versluis, H.-J. Butt, D. Lohse, and X. Zhang, “Self-wrapping of an ouzo drop induced by evaporation on a superamphiphobic surface”, *Soft Matter* **13**, 2749–2759 (2017).
- [132] Y. Li, P. Lv, C. Diddens, H. Tan, H. Wijshoff, M. Versluis, and D. Lohse, “Evaporation-triggered segregation of sessile binary droplets”, *Phys. Rev. Lett.* **120**, 224501 (2018).
- [133] A. A. Pahlavan, L. Yang, C. D. Bain, and H. A. Stone, “Evaporation of binary-mixture liquid droplets: The formation of picoliter pancakelike shapes”, *Phys. Rev. Lett.* **127**, 024501 (2021).



- [134] S. Mao, M. S. Chakraverti-Wuerthwein, H. Gaudio, and A. Košmrlj, “Designing the morphology of separated phases in multicomponent liquid mixtures”, *Phys. Rev. Lett.* **125**, 218003 (2020).
- [135] A. Mailleur, C. Pirat, O. Pierre-Louis, and J. Colombani, “Hollow rims from water drop evaporation on salt substrates”, *Phys. Rev. Lett.* **121**, 214501 (2018).
- [136] Y. Li, V. Salvator, H. Wijshoff, M. Versluis, and D. Lohse, “Evaporation-induced crystallization of surfactants in sessile multicomponent droplets”, *Langmuir* **36**, 7545–7552 (2020).
- [137] A. M. J. Edwards, P. S. Atkinson, C. S. Cheung, H. Liang, D. J. Fairhurst, and F. F. Ouali, “Density-driven flows in evaporating binary liquid droplets”, *Phys. Rev. Lett.* **121**, 184501 (2018).
- [138] Y. Li, C. Diddens, P. Lv, H. Wijshoff, M. Versluis, and D. Lohse, “Gravitational effect in evaporating binary microdroplets”, *Phys. Rev. Lett.* **122**, 114501 (2019).
- [139] C. Diddens, Y. Li, and D. Lohse, “Competing Marangoni and Rayleigh convection in evaporating binary droplets”, *J. Fluid Mech.* **914**, A23 (2021).
- [140] J. de Jong, H. Reinten, H. Wijshoff, M. van den Berg, K. Delescen, R. van Dongen, F. Mugele, M. Versluis, and D. Lohse, “Marangoni flow on an inkjet nozzle plate”, *Appl. Phys. Lett.* **91**, 204102 (2007).
- [141] B. Beulen, J. de Jong, H. Reinten, M. van den Berg, H. Wijshoff, and R. van Dongen, “Flows on the nozzle plate of an inkjet printhead”, *Exp. Fluids* **42**, 217–224 (2007).
- [142] H. Reinten, Y. Jethani, R. Jeurissen, A. Fraters, M. Versluis, D. Lohse, and T. Segers, “Resonance behavior of a compliant piezo-driven inkjet channel with an entrained microbubble”, *J. Acoust. Soc. Am.* **151**, 2545 (2022).
- [143] A. Volk and C. Kähler, “Density model for aqueous glycerol solutions”, *Exp. Fluids* **59** (2018).
- [144] N. Cheng, “Formula for the viscosity of a glycerol-water mixture”, *Ind. Eng. Chem. Res.* **47**, 3285–3288 (2008).

- [145] K. Takamura, H. Fischer, and N. Morrow, “Physical properties of aqueous glycerol solutions”, *J. Pet. Sci. Eng.* **98-99**, 50–60 (2012).
- [146] J. R. Womersley, “Method for the calculation of velocity, rate of flow and viscous drag in arteries when the pressure gradient is known”, *J. Physiol.* **127**, 553–563 (1955).
- [147] L. Landau and E. Lifshitz, *Electrodynamics of Continuous Media* (Pergamon Press) (1984).
- [148] M. Gröninger, P. Kruijt, H. Reinten, R. Schippers, and J. Simons, “Method of controlling an inkjet printhead, an inkjet printhead suitable for use of said method, and an inkjet printer comprising said printhead”, (2008), U.S. Patent 7, 357, 474.
- [149] “<http://oomph-lib.maths.man.ac.uk>”, .
- [150] M. Heil and A. L. Hazel, “oomph-lib - An Object-oriented multi-physics finite-element library”, *Lect. Notes Comput. Sci. Eng.* **53**, 19–49 (2006).
- [151] Y. Li, C. Diddens, T. Segers, H. Wijshoff, M. Versluis, and D. Lohse, “Evaporating droplets on oil-wetted surfaces: Suppression of the coffee-stain effect”, *Proc. Natl. Acad. Sci.* **117**, 16756–16763 (2020).
- [152] A. Zuend, C. Marcolli, A. M. Booth, D. M. Lienhard, V. Soonsin, U. K. Krieger, D. O. Topping, G. McFiggans, T. Peter, and J. H. Seinfeld, “New and extended parameterization of the thermodynamic model AIOMFAC: calculation of activity coefficients for organic-inorganic mixtures containing carboxyl, hydroxyl, carbonyl, ether, ester, alkenyl, alkyl, and aromatic functional groups”, *Atmospheric Chem. Phys.* **11**, 9155–9206 (2011).
- [153] C. Diddens, “Detailed finite element method modeling of evaporating multi-component droplets”, *J. Comput. Phys.* **340**, 670–687 (2017).
- [154] G. D’Errico, O. Ortona, F. Capuano, and V. Vitagliano, “Diffusion coefficients for the binary system glycerol + water at 25 °C. A velocity correlation study”, *J. Chem. Eng. Data* **49**, 1665–1670 (2004).
- [155] T. Driessen and R. Jeurissen, “A regularised one-dimensional drop formation and coalescence model using a total variation diminishing (TVD) scheme on a single Eulerian grid”, *Int. J. Comput. Fluid Dyn.* **25**, 333–343 (2011).

- [156] M. A. Hack, P. Vondeling, M. Cornelissen, D. Lohse, J. H. Snoeijer, C. Diddens, and T. Segers, “Asymmetric coalescence of two droplets with different surface tensions is caused by capillary waves”, *Phys. Rev. Fluids* **6**, 104002 (2021).
- [157] Z. Dagan, S. Weinbaum, and R. Pfeffer, “An infinite-series solution for the creeping motion through an orifice of finite length”, *J. Fluid Mech.* **115**, 505–523 (1982).
- [158] H. Manikantan and T. Squires, “Surfactant dynamics: Hidden variables controlling fluid flows”, *J. Fluid Mech.* **892**, P1 (2020).
- [159] B. Bera, O. Carrier, E. H. G. Backus, M. Bonn, N. Shahidzadeh, and D. Bonn, “Counteracting interfacial energetics for wetting of hydrophobic surfaces in the presence of surfactants”, *Langmuir* **34**, 12344–12349 (2018).
- [160] M. Hack, W. Kwieciński, O. Ramírez-Soto, T. Segers, S. Karpitschka, E. Kooij, and J. Snoeijer, “Wetting of two-component drops: marangoni contraction versus autophobing”, *Langmuir* **36**, 3605–3611 (2021).
- [161] A. Marin, R. Liepelt, M. Rossi, and C. Kähler, “Surfactant-driven flow transitions in evaporating droplets”, *Soft Matter* **12**, 1593–1600 (2016).
- [162] R. van Gaalen, C. Diddens, H. Wijshoff, and J. Kuerten, “Marangoni circulation in evaporating droplets in the presence of soluble surfactants”, *J. Colloid Interface Sci.* **584**, 622–633 (2021).
- [163] Y. Jiang, T. Geng, Q. Li, G. Li, and H. Ju, “Equilibrium and dynamic surface tension properties of salt-free catanionic surfactants with different hydrocarbon chain lengths”, *J. Mol. Liq.* **204**, 126–131 (2015).
- [164] E. Antonopoulou, O. Harlen, M. Rump, T. Segers, and M. A. Walkley, “Effect of surfactants on jet break-up in drop-on-demand inkjet printing”, *Phys. Fluid* **33**, 072112 (2021).
- [165] R. Craster, O. Matar, and D. Papageorgiou, “Pinchoff and satellite formation in surfactant covered viscous threads”, *Phys. Fluids* **14**, 1364 (2002).

- [166] N. Kovalchuk, E. Nowak, and M. Simmons, “Kinetics of liquid bridges and formation of satellite droplets: Difference between micellar and bi-layer forming solutions”, *Colloids Surf. A Physicochem. Eng. Asp.* **521**, 193–203 (2017).
- [167] N. Kovalchuk, H. Jenkinson, R. Miller., and M. Simmons, “Effect of soluble surfactants on pinch-off of moderately viscous drops and satellite size”, *J. Colloid Interface Sci.* **516**, 182–191 (2018).
- [168] P. Kamat, B. Wagoner, A. Castrejón-Pita, J. Castrejón-Pita, C. Anthony, and O. Basaran, “Surfactant-driven escape from endpinching during contraction of nearly inviscid filaments”, *J. Fluid Mech.* **899**, A28 (2020).
- [169] A. Martínez-Calvo, J. Rivero-Rodríguez, B. Scheid, and A. Sevilla, “Natural break-up and satellite formation regimes of surfactant-laden liquid threads”, *J. Fluid Mech.* **833**, A35 (2020).
- [170] R. Sijs, S. Kooij, and D. Bonn, “How surfactants influence the drop size in sprays from flat fan and hollow cone nozzles”, *Phys. Fluid* **33**, 113608 (2021).
- [171] P. Kamat, B. Wagoner, S. Thete, and O. Basaran, “Role of marangoni stress during breakup of surfactant-covered liquid threads: Reduced rates of thinning and microthread cascades”, *Phys. Rev. Fluids* **3**, 043602 (2018).
- [172] H. Wee, B. Wagoner, V. Garg, P. Kama, and O. Basaran, “Pinch-off of a surfactant-covered jet”, *J. Fluid Mech.* **908**, A38 (2021).
- [173] A. Ponce-Torres, J. Montanero, M. Herrada, E. J. Vega, and J. M. Vega, “Influence of the surface viscosity on the breakup of a surfactant-laden drop”, *Phys. Rev. Lett.* **118**, 024501 (2017).
- [174] A. F. Belhaj, K. A. Elraies, S. M. Mahmood, N. N. Zulkifli, S. Akbari, and O. S. Hussien, “The effect of surfactant concentration, salinity, temperature, and ph on surfactant adsorption for chemical enhanced oil recovery: a review”, *J. Pet. Explor. Prod. Technol.* **10**, 125–137 (2020).
- [175] H. J. Staat, A. van der Bos, M. van den Berg, H. Reinten, H. Wijshoff, M. Versluis, and D. Lohse, “Ultrafast imaging method to measure surface tension and viscosity of inkjet-printed droplets in flight”, *Exp. Fluids* **58** (2017).

- [176] L. Yang, B. Kazmierski, S. Hoath, S. Jung, W. Hsiao, Y. Wang, A. Berson, O. Harlen, N. Kapur, and C. Bain, “Determination of dynamic surface tension and viscosity of non-newtonian fluids from drop oscillations”, *Phys. Fluids* **26**, 113103 (2014).
- [177] B. R. Bzdeka, J. Reida, J. Malilab, and N. Prisleb, “The surface tension of surfactant-containing, finite volume droplets”, *Proc. Natl. Acad. Sci.* **117**, 8335–8343 (2020).
- [178] S. Hoath, W. Hsiao, G. Martin, S. Jung, S. Butler, N. Morrison, O. Harlen, L. Yang, C. Bain, and I. Hutchings, “Oscillations of aqueous PEDOT:PSS fluid droplets and the properties of complex fluids in drop-on-demand inkjet printing”, *J. Non-Newton. Fluid Mech.* **223**, 28–36 (2015).
- [179] G. E. Tiller, T. J. Mueller, M. E. Dockter, and W. G. Struve, “Hydrogenation of Triton X-100 eliminates its fluorescence and ultraviolet light absorption while preserving its detergent properties”, *Anal. Biochem.* **141**, 262–266 (1984).
- [180] M. Kamal, “A review of gemini surfactants: Potential application in enhanced oil recovery”, *J. Surfactant Deterg.* **19**, 223–236 (2016).
- [181] V. M. Wasekar and R. M. Manglik, “The influence of additive molecular weight and ionic nature on the pool boiling performance of aqueous surfactant solutions”, *Int. J. Heat Mass Transf.* **45**, 483–493 (2002).
- [182] L. Rayleigh, “On the capillary phenomena of jets”, *Proc. Royal Soc. Lond.* **20**, 196–199 (1879).
- [183] L. H. Phu Pham, L. Bautista, D. C. Vargas, and X. Luo, “A simple capillary viscometer based on the ideal gas law”, *RSC Adv.* **8**, 30441–30447 (2018).
- [184] G. Venditti, V. Mulari, and A. A. Darhuber, “Inkjet printing of surfactant solutions onto thin moving porous media”, *Colloids Surf. A Physicochem. Eng. Asp.* **643**, 127832 (2022).
- [185] C.-M. Tåg, M. Juuti, K. Koivunen, and P. A. C. Gane, “Dynamic water transport in a pigmented porous coating medium: Novel study of droplet absorption and evaporation by near-infrared spectroscopy”, *Ind. Eng. Chem. Res.* **49**, 4181–4189 (2010).

- [186] H. H. Paradies, “Shape and size of a nonionic surfactant micelle. Triton X-100 in aqueous solution”, *J. Phys. Chem.* **84**, 599–607 (1980).
- [187] A. Daerr and A. Mogue, “Pendent\_drop: an Imagej plugin to measure the surface tension from an image of a pendant drop”, *J. Open Res. Softw.* **4**, e3 (2016).

## Summary

In this thesis we investigated challenges in the inkjet printing process that are encountered when droplets are desired to be jetted with a higher velocity or smaller volume, or have a multicomponent composition. The phenomena studied are the bubble entrainment from an oscillating meniscus, the meniscus shape as function of the driving frequency, the measurement method of the liquid composition in the nozzle during drying via the acoustics in the channel, and the role of surfactants on the droplet formation. In the following summary, we briefly describe the main results of each study.

In **Chapter 1**, the bubble pinch-off from an oscillating meniscus is studied in an optically transparent DOD printhead as a function of the driving waveform. We show that bubble pinch-off follows from low-amplitude high-frequency meniscus oscillations on top of the global high-amplitude low-frequency meniscus motion that drives droplet formation. In a certain window of control parameters, phase inversion between the low and high frequency components leads to the enclosure of an air cavity and bubble pinch-off. Although phenomenologically similar, bubble pinch-off is not a result of capillary wave interaction such as observed in drop impact on a liquid pool. Instead, we reveal geometrical flow focusing as the mechanism through which at first, an outward jet is formed on the retracted concave meniscus. The subsequent high-frequency velocity oscillation acts on the now toroidal-shaped meniscus, and it accelerates the toroidal ring outward resulting in the formation of an air cavity that can pinch-off. Through incompressible boundary integral simulations we reveal that bubble pinch-off requires an unbalance between the capillary and inertial time scales and that it does not require acoustics. The critical control parameters for pinch-off are the pulse timing and amplitude. To cure the bubble entrainment problem, the threshold for bubble pinch-off can be increased by suppressing the high frequency driving through appropriate

waveform design.

In **Chapter 2**, we continue our study of Chapter 1 using ultrafast X-ray phase-contrast imaging and direct numerical simulations to study the factors underlying bubble entrainment in a piezo-acoustic printhead. We first demonstrate good agreement between experiments and numerics. The numerical results are then used to show that the baroclinic torque that is generated at the gas-liquid interface due to the misalignment of density and pressure gradients, results in a flow-focusing effect that drives the formation of the air jet from which a bubble can pinch-off.

In **Chapter 3**, the liquid-air meniscus shape oscillations in drop-on-demand inkjet printing are studied. We obtain experimental time-resolved 3D topography profiles of an oscillating meniscus driven at frequencies from 1 kHz to 400 kHz with an accuracy of length scales down to tens of nanometers and microsecond timescales. Furthermore, we obtain the resonance curve for multiple axisymmetric and non-axisymmetric modes of the system. The resonance frequency does not correspond to the eigenfrequency obtained from the capillary dispersion equation for an undriven system. The resonance frequencies for a driven system determined using boundary integral simulations show an improved understanding of the system.

In **Chapter 4**, we study selective evaporation from an inkjet nozzle for water-glycerol mixtures. Through experiments, analytical modeling, and numerical simulations, we investigate changes in mixture composition with drying time. By monitoring the acoustics within the printhead, and subsequently modeling the system as a mass-spring-damper system, the composition of the mixture can be obtained as a function of drying time. The results from the analytical model are validated using numerical simulations of the full fluid mechanical equations governing the printhead flows and pressure fields. Furthermore, the numerical simulations reveal that the time independent concentration gradient we observe in the experiments, is due to the steady state of water flux through the printhead. Finally, we measure the number of drop formation events required in this system before the mixture concentration within the nozzle attains the initial (pre-drying) value, and find a stronger than exponential trend in the number of drop formations required.

In **Chapter 5**, we study the influence of surfactants on droplet formation in piezo-acoustic inkjet printing while we vary the time between the formation of two successive droplets over 5 orders of magnitude, i.e., from microseconds to minutes. During jetting, a large amount of new surface area is created



when the liquid is ejected from the nozzle. Jetting occurs on a microsecond timescale, which is shorter than the typical timescale of surfactant adsorption. Here, we vary the time between the ejection of two droplets to allow surfactants to accumulate on the meniscus. At a waiting time of milliseconds to one second, we observe a change in break-up dynamics, but no effect on the droplet velocity and volume. When the waiting time is longer than one second, when evaporation starts to play a role, the droplet velocity and volume increases. We measured the surface tension of the ejected droplets from their dynamics in flight, which showed that the increased local concentration of surfactant due to evaporation allows for faster surfactant adsorption on the freshly formed surface. Interestingly, increasing the bulk concentration of surfactant does not lead to an increase in droplet velocity, as viscosity starts to play a role as well. Thus, the increased local concentration of surfactant due to evaporation is required to increase the droplet velocity. Numerical simulations demonstrate that the increased concentration at the nozzle exit covers the droplet during the droplet formation process, thereby allowing for surfactant adsorption along the freshly formed surface.

## Samenvatting

In dit proefschrift hebben we uitdagingen onderzocht die je tijdens inkjet printing tegenkomt zodra je wil dat de druppels een hogere snelheid of een kleiner volume hebben, of als de druppel uit meerdere vloeistoffen bestaat. De fenomenen die bestudeert zijn zijn het belinhappen van een oscillerende meniscus, de vorm van meniscus met verschillende aandrijffrequenties, de methode om de vloeistofsamenstelling in the nozzle tijdens drogen te meten via de akoestiek van het kanaal, en de rol van oppervlakteactieve stoffen tijdens de druppelformatie. In de onderstaande samenvatting, beschrijven we de hoofdresultaten van elk onderzoek.

In **Hoofdstuk 1** bestuderen we het belinhappen van een oscillerende meniscus met een doorzichtige DOD printkop als functie van de aandrijvingsgolf. We laten zien dat het belinhappen het gevolg is van een meniscusoscillatie met een hoge frequentie en lage amplitude bovenop de meniscusbeweging met een lage frequentie en hoge amplitude die zorgt voor het produceren van een druppel. In een bepaald gebied van de vorm van de aandrijvingsgolf, zien we dat er een faseverschil is tussen bewegingen met hoge en lage frequentie, waar uiteindelijk een luchtcaviteit door ontstaat die leidt tot belinhappen. Ook al lijkt dit process op het belinhappen als gevolg van interactie tussen capillaire golven waardoor een druppel ingehapt wordt nadat een druppel op een bad inslaat, dat is hier niet het geval. We laten zien dat hier het belinhappen het gevolg is van het focussen van de vloeistofstroming, waardoor er eerst een jet naar buiten ontstaat zodra de meniscus bolvormig is doordat die naar binnen getrokken wordt. Daarna zorgt de oscillatie met een hoge frequentie ervoor dat de ring-vormige meniscus naar buiten versneld, die de jet inhaald en daarmee een luchtcaviteit vormt die kan afknijpen. Doormiddel van *boundary integral* simulaties van een onsamendrukbare vloeistof laten we zien dat het inhappen van een bel een onbalans nodig heeft tussen capillaire en inertiaële tijdschalen,

en dat akoestiek niet belangrijk is. Het belinhappen wordt bepaald door de lengte en amplitude van de aandrijfgolf. Om het belinhappen minder snel te laten gebeuren moet de meniscusoscillatie met een hoge frequentie onderdrukt worden door de juiste golfvorm te gebruiken.

In **Hoofdstuk 2** gaan we verder op het onderzoek van Hoofdstuk 1 door het systeem in beeld te brengen met de ultrasnelle *X-ray phase-contrast* techniek en het gebruik van directe numerieke simulaties om te onderzoeken wat het achterliggende fenomeen is dat zorgt voor belinhappen in een printkop. We laten eerst de goede overeenkomst zien tussen de experimenten en de numerieke simulaties. Daarna laten de numerieke simulaties zien dat het baroklinische moment dat wordt aangedreven op het gas-vloeistof oppervlak door de wanverhouding van dichtheid en drukgradienten, zorgt voor het focussen van de stroming waardoor een luchtcaviteit wordt gevormd die resulteert in belinhappen.

In **Hoofdstuk 3** bekijken we de oscillerende vorm van het gas-vloeistof oppervlakte in een printkop. We verkrijgen experimentele 3D-topografieën op korte tijdschalen van de oscillerende meniscus met een aandrijving van 1 kHz tot 400 kHz met een lengtenauwkeurigheid zo klein als tientallen nanometers en tijdschalen van microseconden. Uit deze resultaten verkrijgen we resonantiegrafieken voor meerde axiaal symmetrische en niet-axiaal symmetrische vormen van het systeem. De resonantiefrequentie die we hier uit halen komt niet overeen met de frequentie uit de berekeningen van de capillaire dispersievergelijking van een systeem dat niet aangedreven is. We bepalen de resonantiefrequenties voor een aangedreven systeem doormiddel van *boundary integral* simulaties, die laten zien dat dit de resonantiefrequenties beter voorspeld.

In **Hoofdstuk 4** wordt de verdamping vanuit de inkjet printkop bestudeerd met een water-glycerol mengsel. Door middel van experimenten, een analytisch model, en numerieke simulaties bestuderen we de veranderingen in de samenstelling van het mengsel als functie van droogtijd. Door de akoestiek in de printkop te meten gedurende de droogtijd, en daarna het systeem de beschrijven als een massa-veer-damper systeem, kunnen we de samenstelling van het mengsel bepalen gedurende de droogtijd. De resultaten van het analytische model valideren we met het numerieke model van alle stromingen en drukvelden in de printkop. Verder laten de numerieke simulaties zien dat de tijdsonafhankelijke concentratieprofiel, dat we ook verkrijgen in de experimenten, het resultaat is van de stabiele toestand van waterstroom de de print-

kop is. Als laatste meten we het aantal druppels dat geproduceerd moet worden in dit systeem om de samenstelling van de vloeistof weer terug te krijgen naar zijn waarde voor verdamping, wat laat zien dat de trend sterker dan exponentieel is tussen hoeveel druppels er nodig zijn en hoeveel tijd er is verstreken.

In **Hoofdstuk 5** bestuderen we de invloed of oppervlakteactieve stoffen op de druppelvorming in een printkop, terwijl we de tijd tussen twee opeenvolgende druppels verlengen met meer dan 5 ordegroottes, d.w.z. van microseconden tot minuten. Tijdens de druppelformatie wordt er een grote hoeveelheid nieuw oppervlak gevormd. De druppelvorming vindt plaats op de tijdschaal van microseconden, wat korter is dan de tijdschaal die typisch nodig is voor adsorptie van de oppervlakteactieve stoffen. In deze studie variëren we de tijd tussen twee druppels om de oppervlakteactieve stoffen tijd te geven om op het oppervlak te adsorberen. Tijdens de wachttijd van milliseconden tot één seconde zien we een verandering in het opbreken van de vloeistof, maar geen verandering in de druppelsnelheid of het volume. Als we nog langer wachten, vindt er verdamping plaats, en neemt de druppelsnelheid en volume toe. We meten de oppervlaktespanning van de gevormde druppels doormiddel van de druppeldynamiek gedurende de vlucht, waaruit we zien dat een toenemende lokale concentratie van oppervlakteactieve stoffen door verdamping ervoor zorgt dat het adsorberen van de oppervlakteactieve stof sneller gaat op een nieuw oppervlak. Interessant genoeg zien we niet hetzelfde effect als we de hoeveelheid oppervlakteactieve stof verhogen, omdat de viscositeit dan ook mee gaat spelen. Dat zou betekenen dat de lokale verhoging van concentratie dankzij verdamping nodig is om de druppel snelheid te verhogen. Numerieke simulaties laten zien dat een lokaal verhoogde concentratie bij de meniscus zich verdeelt over het hele druppeloppervlak gedurende de druppelvorming, waardoor de oppervlakteactieve stoffen over het hele nieuwe oppervlak kunnen adsorberen.

## Scientific output

### Thesis publications

- A. Fraters, **M. Rump**, R.J.M. Jeurissen, M. van den Berg, Y. de Loore, H. Reinten, H. Wijshoff, D. van der Meer, D. Lohse, M. Versluis, and T.J. Segers, “Meniscus Oscillations Driven by Flow Focusing Lead to Bubble Pinch-Off and Entrainment in a Piezoacoustic Inkjet Nozzle”, *Phys. Rev. Applied* **16**, 044052 (2021) - *Chapter 1*
- **M. Rump**, Y. Saade, U. Sen, K. Fezzaa, M. Versluis, D. Lohse, and T.J. Segers, “Vorticity-induced flow-focusing leads to bubble entrainment in an inkjet printhead: synchrotron X-ray and volume-of-fluid visualizations”, to be submitted - *Chapter 2*
- M. van den Broek, **M. Rump**, E. O. Roano, R. Jeurissen, H. Reinten, D. van der Meer, D. Lohse, M. Versluis, G. Lajoinie, and T.J. Segers, “Meniscus mode shapes in inkjet printing”, in preparation - *Chapter 3*
- **M. Rump**, U. Sen, R. Jeurissen, H. Reinten, M. Versluis, D. Lohse, C. Diddens, and T.J. Segers, “Selective evaporation at the nozzle exit in piezoacoustic inkjet printing”, submitted - *Chapter 4*
- **M. Rump**, C. Didden, U. Sen, M. Versluis, D. Lohse, and T.J. Segers, “Role of surfactants on droplet formation in DoD piezoacoustic inkjet printing”, in preparation - *Chapter 5*

### Other publications

- E. Antonopoulou, O. Harlen, **M. Rump**, T.J. Segers, and M. Walkley, “Effect of surfactants on jet break-up in drop-on-demand inkjet printing”, *Phys. Fluids* **33**, 072112 (2021)
- S.H. Lee, K. Harth, **M. Rump**, M. Kim, D. Lohse, K. Fezzaa, and J.H.

Je, “Drop impact on hot plates: contact times lift-off and the lamella rupture”, *Soft Matter* **16**, 7935 (2020)

- S.H. Lee, **M. Rump**, K. Harth, M. Kim, D. Lohse, K. Fezzaa, and J.H. Je, “Downward jetting of a dynamic Leidenfrost drop”, *Phys. Rev. Fluids* **5**, 074802 (2020)
- B. Dyett, A. Kiyama, **M. Rump**, Y. Tagawa, D. Lohse, and X. Zhang, “Growth dynamics of surface nanodroplets during solvent exchange at varying flow rates”, *Soft Matter* **14**, 5197–5204 (2018)
- E. Dietrich, **M. Rump**, P. Lv, E.S. Kooij, H.J.W. Zandvliet, and D. Lohse, “Segregation in dissolving binary-component sessile droplets”, *J. Fluid Mech.* **812**, 349–369 (2017)

## Acknowledgments

In the end, the time as PhD is shaped by the people surrounding you. Without these people, I would not have learned so many new things and become the person I am today. I will try to express my gratitude in words as best as I can, and I apologize in advance if I have forgotten anyone.

*Detlef*, thank you for providing the opportunity to work within your group, it is an amazing environment. I am always impressed with how you keep it running, it seems like an impossible task. Therefore, I always appreciated any time you had for my questions, which often received an efficient and speedy reply. Also, your stories during the trips to Venlo about the scientific community were always very interesting to hear, but the (scientific) discussion on what defines a boy band is the one I will not soon forget.

*Michel*, our first meeting was when I was already a couple of weeks into my PhD, and I was immediately surprised by your attention to detail, but also your ability to quickly switch between a personal conversation to focusing on work. This meant that many personal meetings started with a fun and interesting conversation about holidays and countries before switching to work discussions. Thank you for your critical feedback and polishing of presentations, they have taught me a lot about presenting scientific stories.

*Tim*, you are a great experimentalist and taught me many things, especially in the lab. Also you always had great suggestions for the research that lead to great findings. I very much appreciated that you were often with me in the lab to figure things out, one could not expect better from a daily supervisor. I hope you can still enjoy the lab sometimes these days, even though more desk work is required.

In the collaboration with Canon, I want to thank *Marc, Hans and Youri*, for all your teachings in printhead workings. Often, from the droplet formation

you could already see what the problems were and how to solve those. I feel like we've only touched upon the vast amount of knowledge you have on these systems. *Helder*, thank you for all your collaborations, I hope you have found what you wished for in research. *Ineke*, you have great ideas on what to investigate. It is a shame there was not more time to actually perform the experiments we had in mind, but I'm sure it will be done in the following years. *Herman*, thank you for your ideas and great discussions.

My path to the Physics of Fluids group started at the Physics of Interfaces and Nanomaterials group, where I was introduced to scientific research. *Erik*, thank you for introducing me to this fluidics topic that I enjoy so much, you've given me a strong base on how to perform experiments. *Stefan*, I always appreciate your views on scientific and non-scientific matters, and you have been involved in all my projects since my bachelor. Therefore, I very much enjoy that you are again involved at the end of this big project, we will make it a great day! *José*, we met at PIN, and later on you became my supervisor at PoF. We had a lot of fun, and your punting skills in Cambridge were amazing. Thank you for the good times.

Of course PoF would not exist without the work of at the heart of the group: *Joanita*, thank you for your wonderful chats throughout the years and amazing efficiency to help out everyone at incredible speeds. *Bas*, *Gert-Wim*, *Martin*, *Dennis* and *Thomas*, there really was not a technical problem you could not help me with, even the ones related to the bikes at home. Thank you for keeping the labs running and safe.

It was great being involved in the FIP project, providing many opportunities to discuss topics and meet new people. *Udo*, after my first two years you became my go-to person, with whom I could share my ideas, doubts and questions, both scientific and non-scientific. Thank you for always being there and sharing work related trips as well as bike trips. Your view on science has taught me many things and I enjoyed working together with you. I wish you all the best going forward! *Christian*, your skills with your numerical code are simply impressive. You amazed us with showing new results during every meeting we had at Canon. It took quite a while before I was able to perform the experiments which could be used as a validation for your code, with very nice results. You even managed for me to run some simulations myself. Thank you very much for all the great collaborations. *Michiel*, thank you for all the fun, and sometimes extensive, chats in the lab, during lunch walks, conferences and holidays. *Arjan*, *Yaxing*, *Wojtek*, *Lijun*, *Yogesh*, *Pim*,



and the others involved in the FIP project, we often had good times during all the meetings and thank you for the many interesting discussions.

The Run group did organize some runs, but we actually mostly used the group for a lot of other stuff. *Myrthe*, it already feels so long ago when we met during the complex motion summer school. Since then, I would say, we have conquered our experimental setups! We enjoyed so many fun activities such as running, music and beachvolleyball (especially with Bram and Pieter), I cannot thank you enough for having been there on this journey. *Jessica*, you taught me so many things. Thank you for helping me facing fears and of course the obstacle courses. Your ability to make others feel at home is incredible, never forget that. *Anja*, the trips to you were always highlights for me during Covid/lockdown times. Thank you so much for all the laughs and talks we have had, especially during the final stretch of the thesis writing. And soon we will finally have the trip on which we will be roomies! *Carola*, I've thoroughly enjoyed our music sessions, with of course the accompanying zure matjes. Thank you for listening, your supporting discussions, and pushing me a little bit further than my comfort zone during climbing. *Diana*, thank you for the fun evenings of (almost prophetic) Pandemic games, but even more for all walks and talks while enjoying the sun. We still have to go dancing sometime! *Ambre*, thank you for all the great chats, especially in the lab.

My office mates in ME250 and ME152. *Kirsten*, thank you for the amazing experience at the synchrotron, where we even received someone's genuine question if we were working on time traveling. It was great having you as an office mate. *CS*, besides the time in the office, we also enjoyed times on the bike. Thank you for your friendship and making ME250 a great office, including the great smells from Cindy's delicious cooking. *Martin A.*, you made the great introduction of cakes in the office, and often surprised us with your delicious cakes. Thanks! *Yibo*, you introduced me to funny new things, and I will not soon forget your giant jar of protein powder. *Mathieu* and *Pallav*, thank you for welcoming me into ME152 and the great office chats. *Guilia* and *Simon*, I'm happy to share my last moments at PoF with you, and I wish you all the best with your PhD's!

My numerics guys *Youssef* and *Edgar*, even though you were not part of FIP, I've had the pleasure to work with you and be able to rely on your numerical skills. *Youssef*, because you were often traveling, it was always a great pleasure to see you back at PoF again and enjoy non-scientific talks and activities. Thank you for all the good times! *Edgar*, you were always ready to

go at any moment and I admire your work attitude, thank you for the time you've spent explaining things to me and helping me out.

To the team of the Vloeistoffysica practicum, *Michel*, *Devaraj*, *Jelle*, *Utkarsh*, *Pallav*, *Udo*, *Ambre*, and *Luuk*, thank you for this teaching experience, I learned many new things on lab equipment but also on educating students. Furthermore, *Alvaro* thank you for involving me in the Experimental Techniques course, which was another new experience.

I've also had the pleasure to (co-)supervise students during their bachelor and master projects in the group. *Martin*, I greatly enjoyed working with you and also learning from you. The images you produced are beautiful and will hopefully soon be published. We also had great times outside the group during beachvolleyball. Thank you for the good times and best of luck during your own PhD adventure. *Christel*, it was a bit hectic at the start due to the closure of the labs. You worked very independently, making me sometimes wonder if things were okay. However, your good results say all that is needed, thank you.

There are several people in PoF who I still want to thank. *Jelle*, we both started in PoF on April 1st, which fortunately turned out to be no joke. You introduced me to the beauty of turbulent experiments and the tricky analysis that goes with it. You've made some beautiful things, don't stop. I hope you find great joy on the other side of the world. *Vatsal*, never loose that passion for science, your enthusiasm is inspiring to watch. Thank you for all the fun discussions we have had over the years. *Ricardo*, thank you for the great times, especially during climbing and the wonderful trip to Sofia with the amazing band (I still cannot believe they were so late we almost left!). I also had the pleasure for organizing the Batavierenrace for multiple years with many people, of which I still want to mention: *Pieter*, you giant, the beachvolleyball matches were always amazing, we should keep doing those; and *Luuk*, my fellow korfbal enthusiast, the PoF bata is safe in your hands and we will definitely enjoy the edition of this year. Finally, I want to thank *all other PoF members* in the past and present for all the great times and many scientific and non-scientific discussions.

Besides the PoF group, I also want to thank everyone from the Nanoelectronics group that shared many fun times and activities together, especially during the unforgettable two full party weeks, tequila will never be the same.

My friends from Utrecht (and Wageningen), *Ina*, *Nikki*, *Esmée*, and *Allyson*, who would've thought that we would still be in contact and visiting each other after so many years. Thanks! We will keep this going of course.

Verder wil ik ook mijn familie bedanken. Ten eerste natuurlijk mijn ouders en zusje. *Mam*, *pap* en *Elise*, bedankt voor jullie onvoorwaardelijke steun, interesse, en al het andere waar gewoon geen woorden voor zijn. Ik kijk er naar uit deze periode samen met jullie af te sluiten, omdat ik nu al weet hoe ongeloofelijk trots jullie zijn. *opa* en *oma*, ik ben elke keer weer sprakeloos als jullie me weer verbazen met intuïtie over mijn onderzoek en natuurlijk jullie passie voor fietsen. Het betekent veel voor me dat jullie bij mijn verdedeging kunnen zijn. Graag wil ik ook mijn dank uitspreken naar de *familie van de Ven*, onze thuishaven in het zuiden, en *Piet* en *Fanny* in het noorden.

Tot slot, *Bram*, ik zou niet weten hoe ik ooit duidelijk kan maken hoeveel je voor mij betekent. We hebben zoveel geleerd gedurende onze PhD avonturen, over elkaar, van elkaar, door elkaar, in de dieptes en de mooie hoogtes. We blijven samen nieuwe dingen leren, en ik kijk er naar uit nog veel mooie avonturen te beleven samen met jou.

